MECHANICAL PROPERTIES OF THE NIOBRARA

by

Mason Bridges

A thesis submitted to the Faculty and the Board of Trustees of the Colorado School of Mines in partial fulfillment of the requirements for the degree of Master of Science (Geophysics).

Golden, Colorado

Date_____

Signed:_____
Mason Bridges

Signed:_____
Dr. Manika Prasad
Thesis Advisor

Golden, Colorado

Date_____

Signed:_____
Dr. Roel Snieder
Professor and Head
Department of Geophysics

ABSTRACT

The Niobrara Formation consists of alternating chalk and marl intervals. The chalk intervals comprise reservoir units while the marl intervals act as sources and seals. Mineralogy and kerogen content are vertically and laterally heterogeneous, and knowledge of mechanical properties improves calculation of minimum horizontal stress, a primary control of fracture growth. Permeability is enhanced by fracture networks, and the detection of these networks informs completion decisions. In this study laboratory ultrasonic and static measurements are used to derive relationships enabling the creation of an anisotropic stress model for a well in Wattenberg Field, CO, USA. The well log is also used to apply a fracture detection method that considers the fractured medium transversely isotropic with a horizontal axis of symmetry (HTI). Applying Hudson's crack model to the laboratory anisotropy data serves as a quality check for the method.

Dry rock velocity and strain measurements were taken for the D chalk and marl facies of the Niobrara. Mineralogy, TOC, and vitrinite reflectance data were obtained for the laboratory samples and the studied reservoir facies. The samples measured in the laboratory exhibit lower velocity pressure sensitivity than is observed in the studied well, which is related to peak maturity of the lab samples.

The dry rock velocity measurements are used to obtain the Thomsen parameters for both facies. The chalk samples tested are isotropic, and the marl samples are weakly anisotropic. Anisotropy decreases with increasing confining pressure, and the observed trend is commensurate with laboratory tests of peak-mature shales (Vanorio, 2008). Saturated velocities from Maldonado (2010) were used to observe the anisotropic response to pore fluid pressure. ε

and γ both decrease with increasing pore and confining pressure. γ exhibits a greater response to increasing pore fluid pressure than to confining pressure for the measured facies.

Empirical relationships between the laboratory-derived Thomsen parameters are applied to the dipole shear log, which is treated as a dry rock measurement. Static and dynamic elastic parameters are measured to further describe the dry rock mechanical properties. The parameters are compared with Voigt-Reuss-Hill effective medium theory and employed in uniaxial strain approximations of the minimum horizontal stress.

The anisotropy present in the study well is considerably lower than that measured in the laboratory samples. The estimation of δ allows the application of the ANNIE approximation. The approximated constants are corrected to the static case using the laboratory-derived ratios, and the errors resultant from utilizing dynamic constants and assuming isotropy are discussed.

Fracture density is estimated using a method developed by Conoco (Sil, 2013). The method considers the formation a homogenous, horizontal transverse isotropic (HTI) medium consisting of vertical, parallel sets of fractures. In Conoco's method δ_N, the normal fracture weakness, is used to derive the fracture density, e. δ_T, the tangential fracture weakness, replaces δ_N in this method since δ_T is less prone to second-order effects. Fracture density is compared to the laboratory-derived anisotropy parameters using Hudson's crack model.

TABLE OF CONTENTS

LIST OF FIGURES

LIST OF TABLES

Acknowledgements

I would like to acknowledge Manika Prasad, Denton O'Neal, Dana Gallegos, Brandon Bolach, Azar Hasanov, Mandy Schindler, Jesse Havens, Matt W., Jimmy Gayer, Craig Markey, Nick Fetta, Matthias Pohl, Conrad Newton, Tom Davis, Andre Swidinsky, Tom Bratton, Bob Benson and the Niobrara Consortium. The successes of this work I attribute to them, the failures are mine.

Dedication

To the memory of Mike Batzle.

CHAPTER 1

INTRODUCTION

The Niobrara Formation is a subunit of the Mancos shale, consists of the Fort Hays member and the Smoky Hill Member, and is a self-sourcing hydrocarbon system comprised of chalk-reservoir intervals sourced and sealed by organic-rich marls. Mechanical characteristics, porosity, permeability, and organic-matter content are laterally heterogeneous and vary with depth and pressure. The low porosity and permeability of the Niobrara complicates hydrocarbon extraction, and obtaining the mechanical properties enhances completion design. This chapter discusses our motivation for this study, research objectives, study area, and methods.

1.1. Motivation

The Niobrara Formation, consisting of the Smoky Hill and Fort Hays members, is a tight shale formation comprising marl sections of varying clay content. These sections are generally divided into “chalks” and “marls.” Horizontal wells and hydraulic fracturing improve completions and production in the Niobrara. Anisotropy, both mechanical and elastic, is common and complicates seismic processing and completions. Moreover, the anisotropy in the Niobrara is exacerbated by the existence of fault and fracture networks that disrupt characterization techniques across various scales. This thesis has three primary goals: 1) describe the P-wave and S-wave anisotropy of the Niobrara, 2) describe the elastic parameters and elastic anisotropy of the Niobrara, and 3) determine if the host rock of the Niobrara fits the criteria for full-waveform, fracture-detection methods.

1.2 Objectives and Purpose

The purpose of this study is to quantify the P-wave and S-wave anisotropy, elastic constants, elastic anisotropy, and fracture mechanics of the Niobrara Formation, Wattenberg Field, Denver Basin, CO. The mechanical anisotropy of the Niobrara is described with the Thomsen parameters δ, ϵ, and γ (Thomsen, 1986). δ is the most important parameter in seismic processing as it describes the near-vertical *P*- and *S*-wave anisotropy, which must be taken into account for Normal Move-Out (NMO) algorithms. The anisotropy of the host rock is important when determining if full-sonic-waveform fracture-detection inversions are appropriate (Bakulin et al., 1999; Sil, 2013). We are also interested in how anisotropy changes with respect to clay content.

The mechanical properties, especially the Young's modulus and Poisson's ratio, are key determinants of the elastic behavior of materials, and knowledge of the elastic anisotropy enhances completion design (Higgins, 2008). We compare the laboratory-derived anisotropy parameters to the well log and determine if the ANNIE approximation (Schoenberg and Sayers, 1996) is appropriate for modeling the elastic properties. We also compare the lab- and log-derived elastic properties to effective medium theory and determine how clay and kerogen content affect stiffness. The parameters also enable the implementation of fracture-detection inversions that determine the location of naturally-fractured reservoirs.

Finally, we are concerned with how fractures affect the mechanical behavior of the Niobrara. We combine the mechanical properties and wave anisotropy data to locate fractures in our study well. We compare the fracture density in our study well to Hudson's crack model (Hudson, 1981) predictions from the lab. We criticize shortcomings in previous work and use anisotropy theory to improve fracture-detection inversions and hydrocarbon indication.

1.3 Study Area

Samples tested in the laboratory come from the Cemex quarry in Lyons, CO. A well log suite was also acquired at the quarry site. The laboratory data is compared to log data acquired in Wattenberg field, which is located in the center of the Denver Basin and is one of the largest oil and gas fields in the United States. The well logs studied are the Noble Aristocrat PC H11-07, referred to as the "Noble Aristocrat" or "Aristocrat" well, and the Weld CO State 2-13 well, acquired from the Colorado Oil and Gas Conservation Commission (COGCC) archives.

1.4 Methodology

This project involved laboratory core testing and well log data analysis. As mentioned previously, samples of the D chalk and D marl were collected from the Lyons, CO Cemex quarry. Cores oriented 0^o, 45^o, and 90^o to bedding were extracted from the blocks. Uniaxial compressive tests and thick-walled cylinder tests were conducted to acquire data for calculating the static and dynamic elastic constants, respectively. The stress, strain, and velocity data were used to calculate the elastic constants, which were compared and used to estimate elastic anisotropy. The velocity data contained P, S_1, and S_2 arrival times; these were also used to calculate the wave anisotropy via the Thomsen parameters (Thomsen, 1986). Calculations for the laboratory measurements, to include plotting the wave arrivals, were performed in Excel.

Well log data for the Noble Aristocrat and CO Weld State 2-13, both .las files, were loaded into the Schlumberger TechLog software. The Noble Aristocrat well contains P-wave and dipole sonic data, density, gamma ray, density porosity, and thermal neutron porosity data. The CO Weld State 2-13 log suite contains P and monopole S-wave, Stoneley wave, density, gamma ray, density porosity, and thermal neutron porosity data. The Stoneley wave data was converted

to S_H-wave data. The elastic constants for the anisotropic case were calculated using the ANNIE (Schoenberg and Sayers, 1996) approximation, and the viability of this method is supported by the measured mechanical anisotropy. Thomsen parameters were calculated using relationships derived in the laboratory, and HTI fracture-detection inversion was implemented utilizing a method derived by Bakulin (1999). Expanded discussion of these methods can be found throughout this thesis.

1.5 Thesis Organization

This thesis is organized into seven chapters with the main chapters, 4-6, discussing the primary research findings. Chapter 2 is an introduction and discusses the geology of the Niobrara and expands on the motivation for this research. Chapter 3 discusses the experimental and quantitative methods, samples tested, and also briefly discusses shale maturity and how it affects rock mechanical properties.

Chapter 4 discusses the Thomsen parameters. The chapter begins with a comparison of various formations and how the Thomsen parameters vary according to various clay fractions and maturities. I also show how ϵ and γ vary with increasing overburden stresses and pore pressures. The laboratory derived Thomsen parameters are used to derive a correlation that may be used to estimate the well log-derived Thomsen parameters. Once the well log-derived Thomsen parameters are estimated I apply the ANNIE approximation to estimate the downhole stiffness tensors. With the stiffness tensors calculated I show the potential modeling errors that may arise by assuming isotropy during the ANNIE approximation.

Chapter 5 is a report of the laboratory-derived Young's modulus and Poisson ratios for the D chalk and D marl. The laboratory-derived parameters, both static and dynamic, are

compared to one another, to the well log-derived elastic parameter values, the Voigt-Reuss-Hill averages, and other calcareous shale formations of varying clay contents and maturities. The well log-derived elastic constants are used to estimate minimum horizontal stress over the study area reservoir intervals. The different quantitative methods for estimating minimum horizontal stress are compared and potential method error is discussed.

Chapter 6 uses the well log data to implement a fracture-detection inversion developed by Sil (2013). The chapter discusses the approach and criticizes the use of the normal fracture compliance parameter, δ_N. I applied a modified version of the method and report the results which are then compared against past results. The chapter ends by discussing the applicability of a Hudson's crack model-based inversion on layered media adjacent to boreholes and notes that clay layering may cause the false detection of fractures. Chapter 7 is a concluding discussion.

CHAPTER 2

NIOBRARA GEOLOGIC SUMMARY

This chapter discusses the geology of the Niobrara Formation. Topics covered are the regional setting, structural setting, depositional environment, stratigraphy, and general reservoir characteristics.

2.1 Depositional overview

The Niobrara was deposited in the Denver Basin, one of the largest basins in the Rocky Mountain region (Higley, 2007). The Denver Basin is asymmetric, Laramide-age (65-30 Ma), and bounded on the west by the Front and Laramie ranges (Higley, 2007). The Laramide Orogeny is credited with most of the clay deposition in the Niobrara (Pollastro and Scholle, 1987). The deepest part of the basin, located near Denver, contains more than 13,000 feet of sediments. The largest field in the Denver Basin is Wattenberg field, covering 2000 square miles and including more than 20,000 wells (Weimer et al., 1986; COGCC, 2015).

During the Cretaceous, rising temperatures resulted in a "warm-temperate to subtropical" (Surlyk et al., 2003) climate that caused global eustatic sea-level rise (Pollastro and Scholle, 1987). This sea-level rise facilitated worldwide chalk deposition, an episode that accounts for 70% of the carbonate deposition that has taken place in the past 100 million years (Hay et al., 1976). In contrast to modern chalk deposition, which is generally restricted to ocean basins, widespread deposition of chalk occurred in epicontinental seas (Pollastro and Scholle, 1987). The Western Interior Seaway (Figure 2.1) was one such sea, an elongate asymmetrical trough that extended north-south across much of the Mid-Continent (Pollastro & Scholle, 1987). This

trough was the site of the deposition of the Niobrara Carbonate Shale, a sub-unit of the Mancos Shale.

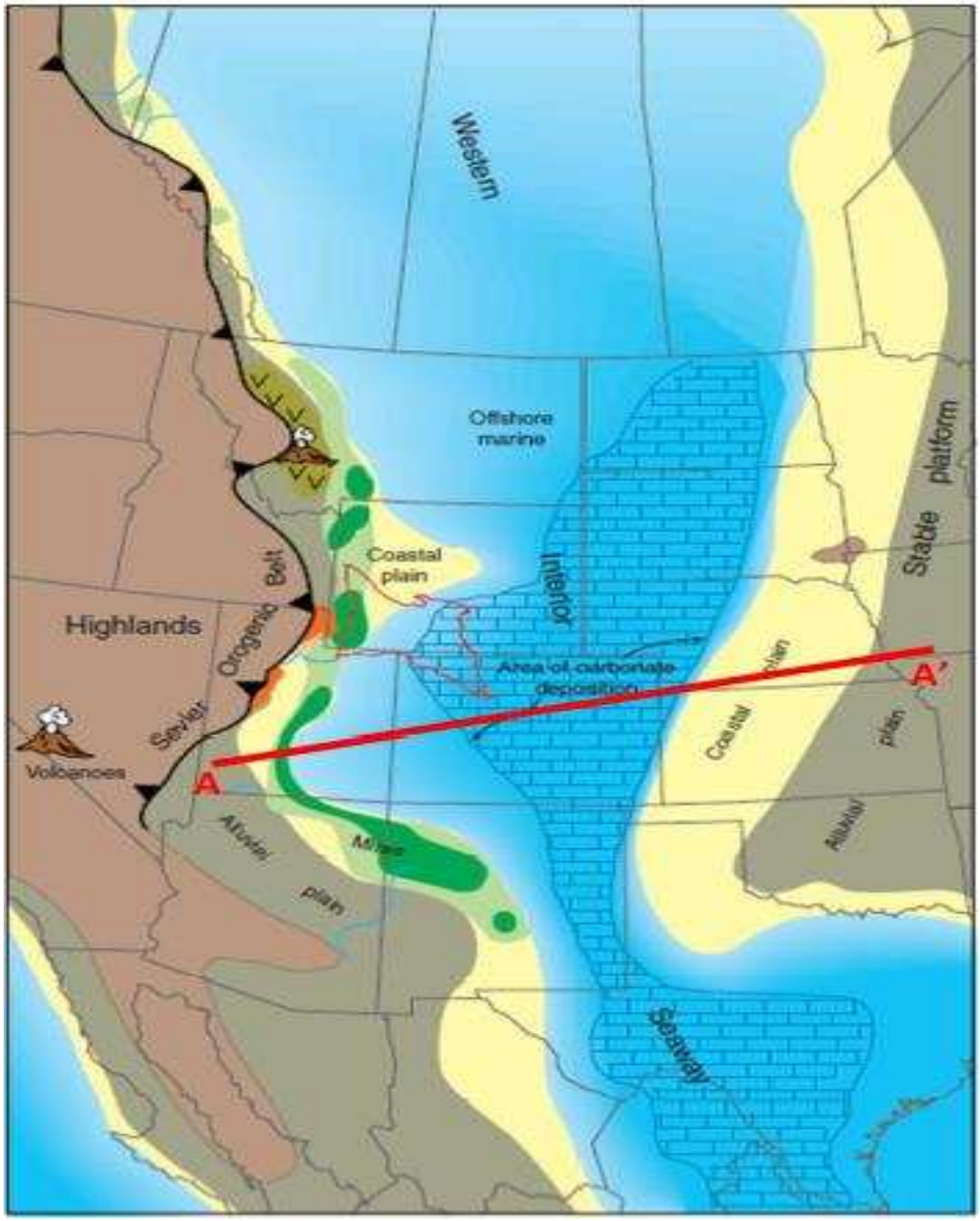

Figure 2.1. Image of the Western Interior Seaway, site of major chalk deposition in ancient North America. Red line indicates location of cross section shown in Figure 2.2. Image sourced from Maldonado (2011).

.

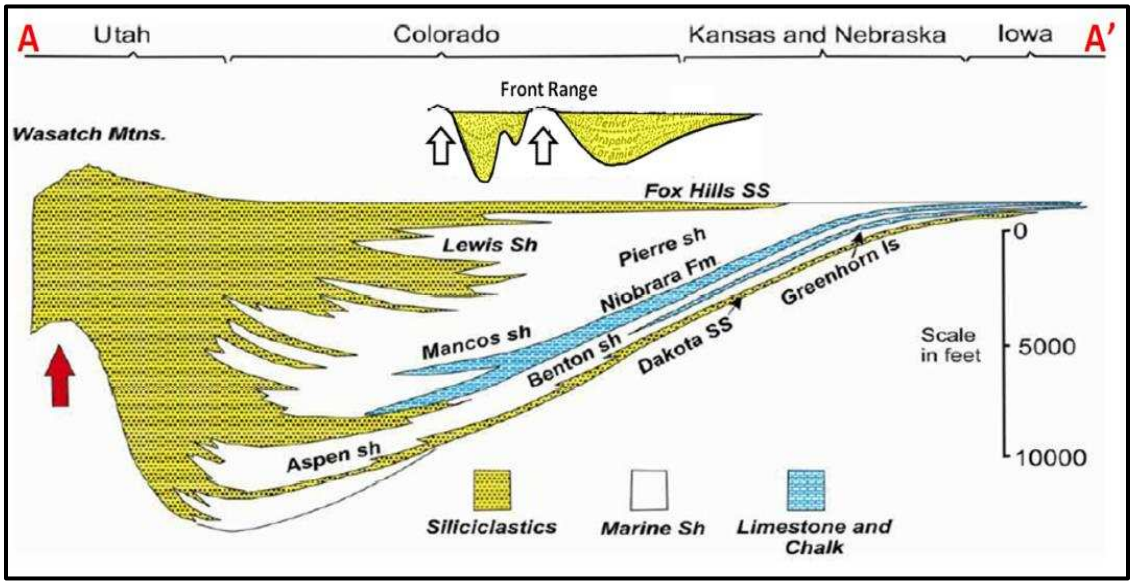

Figure 2.2. Cross section A-A' of Western Interior Seaway Basin shown in Figure 2.1. The Niobrara is a subunit of the Mancos Shale. Notice the West-East thinning trend. Image from Sonnenberg (2011).

Over broad areas, deepwater chalks are characteristically homogenous (Pollastro & Scholle, 1987), but in the Western Interior Seaway, a shallower depositional environment and structural factors led to East-West heterogeneities (Weimer, 1978; Rice & Shurr, 1983). These heterogeneities take the form of depositional thinning as a function of the Transcontinental Arch, as well as a gradual Westward decrease in chalk purity due to detrital sedimentation from the Laramide uplift (Pollastro & Scholle, 1987).

The micritic Niobrara formation is marl that was formed by the assemblage and diagenesis of calcareous, organic, and terrigenous components (Pollastro & Scholle, 1986). It consists of approximately 70-80 % carbonate (Pollastro & Scholle, 1986), and the calcium-carbonate ($CaCO_3$) is primarily derived from the nannofossils of golden-brown algae known as Coccolithophorids. These algae formed and shed platy shells called coccoliths, which range in

size from 0.4 to 1 μm and can occur in a spherical arrangement, forming coccospheres, with diameters of 10 to 25 μm (Surlyk et al., 2003). Rhabdoliths, planktonic foraminifera, and calcispheres also supplemented Niobrara chalk deposition, (Tucker and Wright, 1990) along with lesser contribution from macrofossils such as bivalves and inoceramids (Pollastro & Scholle, 1986).

The reservoir chalks of the Niobrara have somewhat low (approximately 5%) microporosities and relatively low (0.5 mD) permeabilities. Sea floor chalks, proximate to time-of-deposition, exhibit porosities of 60-80 % (Pollastro and Scholle, 1986). The Niobrara chalk was therefore subjected to a regimen of mechanical compaction and dewatering prior to chemical compaction. The primary driver of chemical compaction is pressure solution, where mineral dissolution at grain contacts is re-precipitated within the pore space (Pollastro, 1992). Observed stylolites at Niobrara outcrops reinforce the pressure solution hypothesis. The effects of compaction and diagenesis are profound. In some areas the Niobrara formation porosity decreased from 40 % to 5 %.

2.2 Stratigraphy

The Fort Hays and Smoky Hill members constitute the two main divisions of the Niobrara. The Fort Hays member is the purest and oldest chalk of the Niobrara. The Smoky Hill Member is subdivided into four chalks, from top to bottom, the A, B, C, and D Chalks. These are interbedded by marls, which are referred to as the Upper, Middle, and Lower Marl. Within each subunit of the Niobrara there are unique depositional sequence patterns that are the function of smaller cycles (See Figure 2.3).

In Colorado, the Niobrara's thickness varies from 60 to 120 m in the northeast part of the state, while to the northwest, the formation can be more than 460 m (1500 ft) thick (Eisinger, 2011). As shown in Figure 2.2, general thickness decreases from West to East. In Figure 2.4, one notices high resistivity zones that correspond to high gamma ray values. This is an indication of the role of the marls as source rocks. Hydrocarbon migration generally occurs as fractures permit oil and gas to flow into the reservoir chalks of the formation.

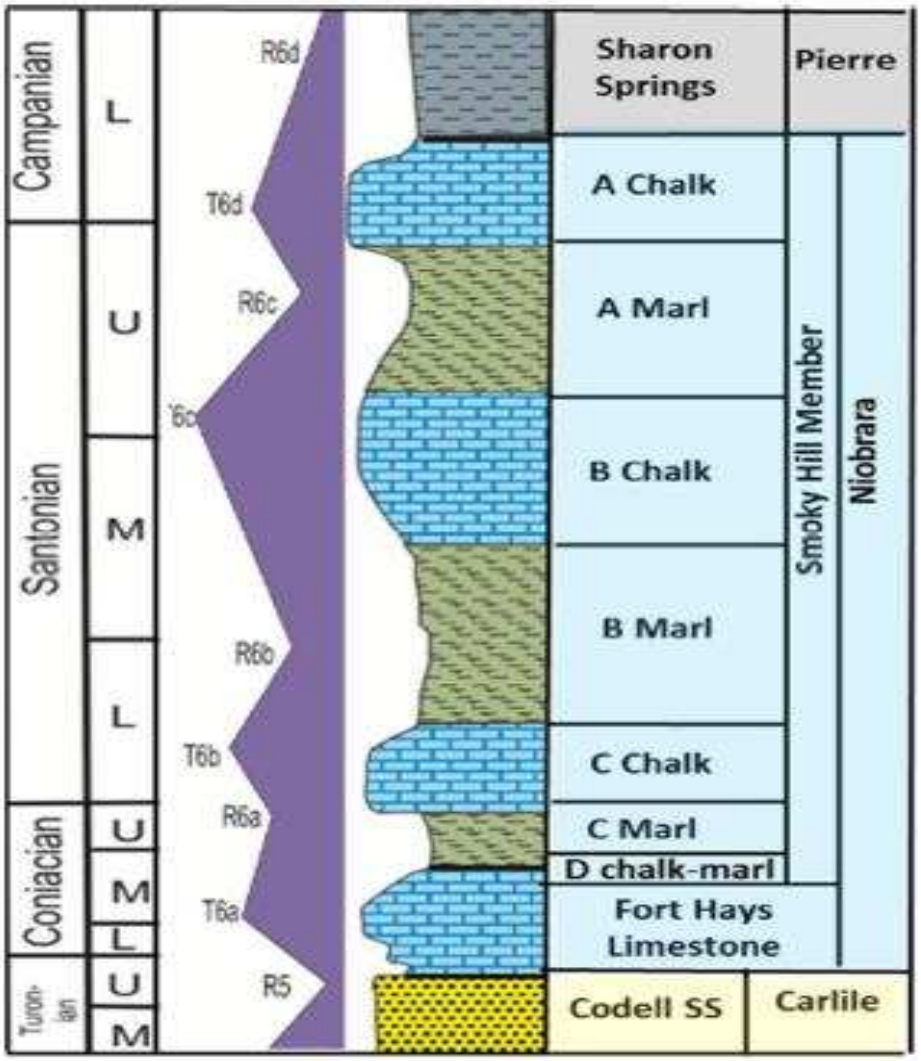

Figure 2.3 Transgressive-regressive cycles of the Niobrara Cyclotherm and Niobrara Stratigraphy.The image is sourced from ElGhonimy (2015) and represents a modification of Kauffman (1977).

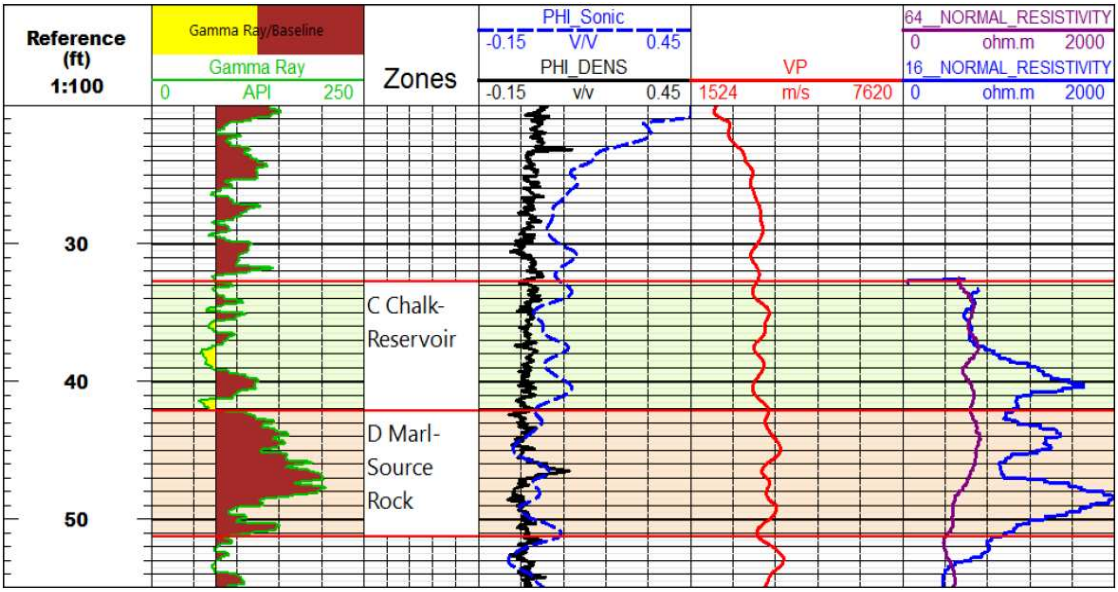

Figure 2.4. Well log image of the Niobrara from Layne Cemex #17. This log shows the relationship between the marl sections, which are source rocks, and the chalk sections, which are reservoir rocks. This well log was acquired at the Cemex Lyons, CO quarry.

2.3 Outcrop study, core samples, and well log locations

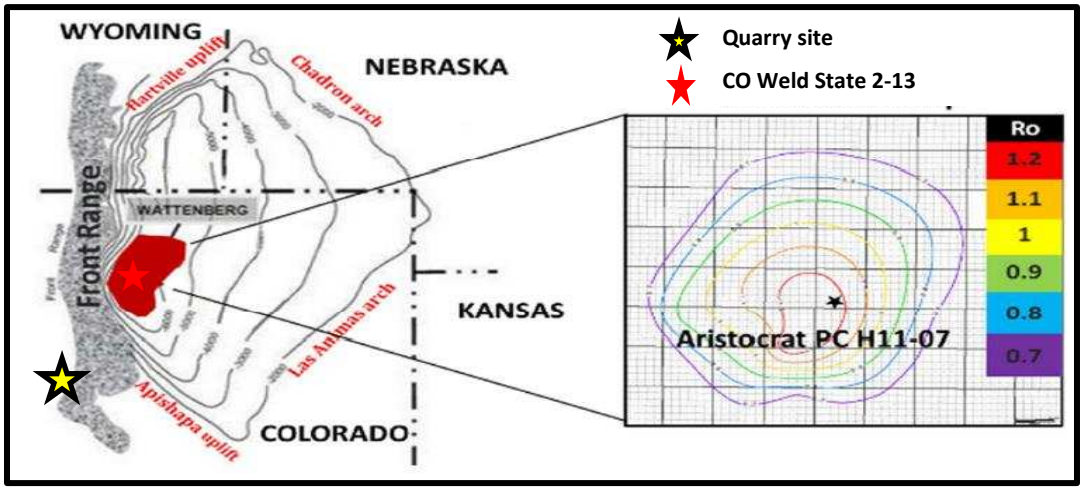

Figure 2.5 General overview of study area and resource characteristics. The red shaded area represents Wattenberg Field, and the yellow and red stars represent the Layne Cemex quarry site in Lyons, CO and CO Weld State 2-13 well, respectively. The vitrinite reflectance (R_o) contour map shows that the Noble Aristocrat well lies in a mature, gas-producing zone. Image sourced from ElGhonimy (2015).

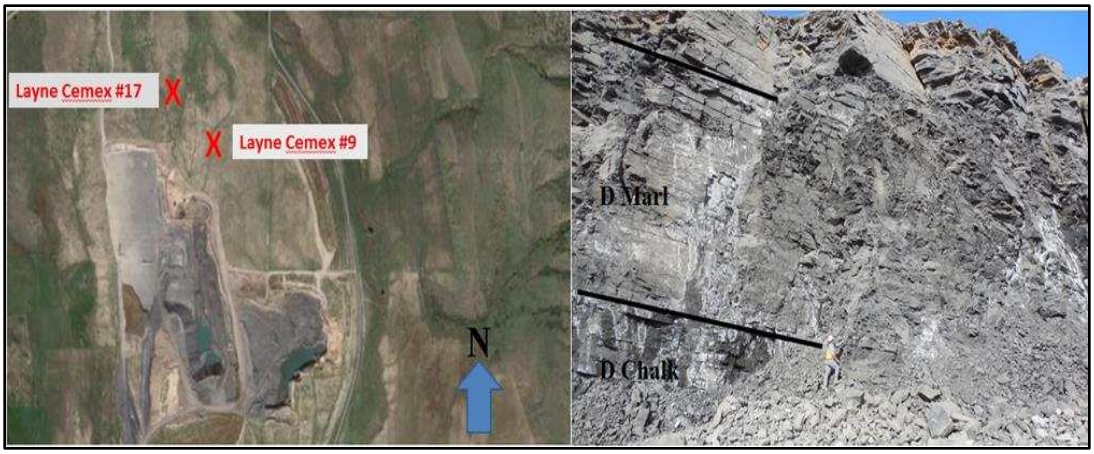

Figure 2.6. Image of survey site at Cemex quarry, Lyons, CO. The picture to the left shows an aerial view of the Cemex quarry while the picture on the right shows the D Chalk and D Marl from inside the quarry.

Field study, including well logging, geologic measurements, and sample collection, was conducted at the CEMEX cement quarry in Lyons, CO (Figure 2.6). The chalks and marls of the Niobrara can be differentiated by color at the CEMEX quarry site. The chalk intervals, when not hydrocarbon-bearing, are whitish-gray to gray, and the marls are dark-gray to black, depending on organic content. The D Chalk is whitish-gray to gray while the C Chalk, which is sourced by the D Marl, is dark-gray to black-colored.

I describe the acquired D Chalk samples as a light-gray pyritic, foram rich, bioturbated chalk. I measured strike and dip and found the chalks striking N 14 E and dipping 15 degrees East. I describe the D Marl samples as dark-gray to black, foram rich, bioturbated chalk with pyrite concretions, and striking N 45 W and dipping 16 degrees East. Inoceramid fossils, bioturbations, ripples, and pyrite, both crystals and concretions, were observed at the quarry site and are common in the Smoky Hill member. These are also typical of a shallow-sea benthic depositional environment (Pollastro and Scholle, 1986).

Fracture characterization is an important component of producing oil and gas from the Niobrara, and we took care to observe fracture orientations while in the quarry. The fractures I observed are primarily large, parallel vertical fractures that indicate vertical principal stress.

Figure 2.7. Images of D Chalk (left) and D Marl (right) samples. The D chalk is a clean chalk while the D marl contains clay, pyrite, and organic matter.

These large vertical fractures may be factor contributing to acoustic wave anisotropy in the Niobrara (Chapter 6). Due to the dynamite blasting and ongoing removal that takes place at the

quarry the fractures are easily observable and exhibit wider apertures than those existing in-situ (Romm, 1985). I also observed vertical stylolites and calcite-filled horizontal fractures. Both indicate that the principal stress was once horizontal, most likely due to thrust-faulting during the Laramide Orogeny (71-50 Ma).

Porosity in the Niobrara formation ranges from 40-50% and 25-35% in the Beecher Island zone (Pollastro, 1996), while porosity at greater depths can be as low as 2-5%. Despite the high porosities encountered at shallower depths, permeability values in the Niobrara range from 0.05-5 mD. At greater depths the low porosities and permeabilities make hydrocarbon extraction difficult. I plotted density porosity over depth for the Aristocrat well (Figure 2.8) to illustrate the effects of depth.

When clay particles fill the pores of a medium comprised of larger particles microporosity dominates the fabric (Revil, 2013). This phenomenon has profound effects on the ability of a porous medium to transmit fluids. To see if clay content has a profound effect on porosity values in the Smoky Hill member I plotted gamma ray and porosity (Figure 2.9) and found that high clay content is not a limiting factor when it comes to log-derived porosity values in the Niobrara. I assume that this is due to clay particles in the intra-pore spaces. This indicates that microporosity is the dominant porosity type in the Niobrara, and that one should expect a noteworthy decrease in permeability as clay content increases.

Due to the "tight" nature of the Niobrara, most log-derived measurements overestimate permeability. To observe the effects of clay content on permeability within the Niobrara, I queried the database at the Colorado Oil and Gas Conservation Commission and found well log and core test data for a well drilled by EOG Resources. The well is LaMotta 5-01M in Weld County, CO and the permeability data corresponds to the B Chalk. I plotted the permeabilities

against gamma ray from the well log and show that there is an inverse correlation between clay content and permeability (Figure 2.10).

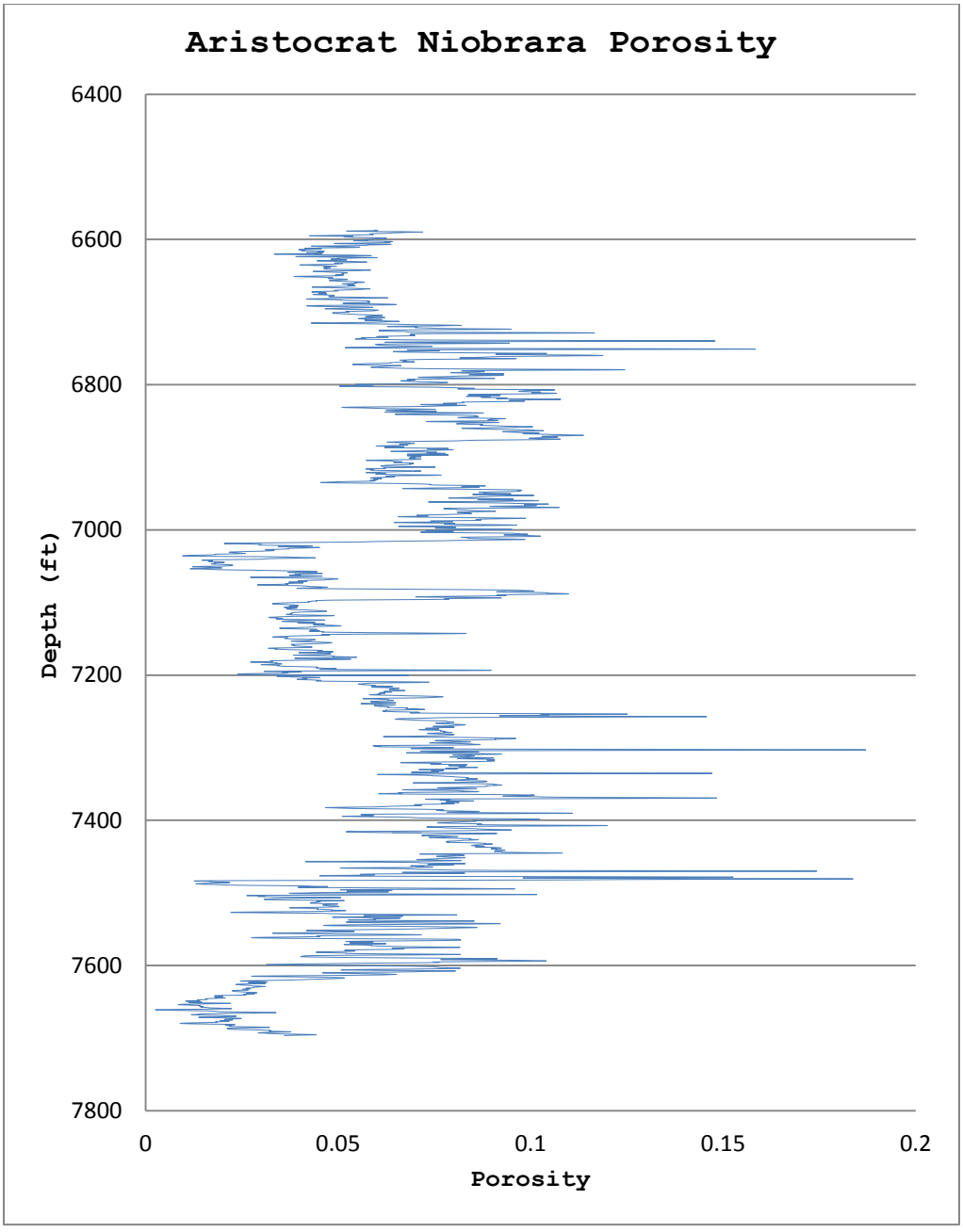

Figure 2.8. Plots of depth over density porosity for Noble Energy's Aristocrat well.

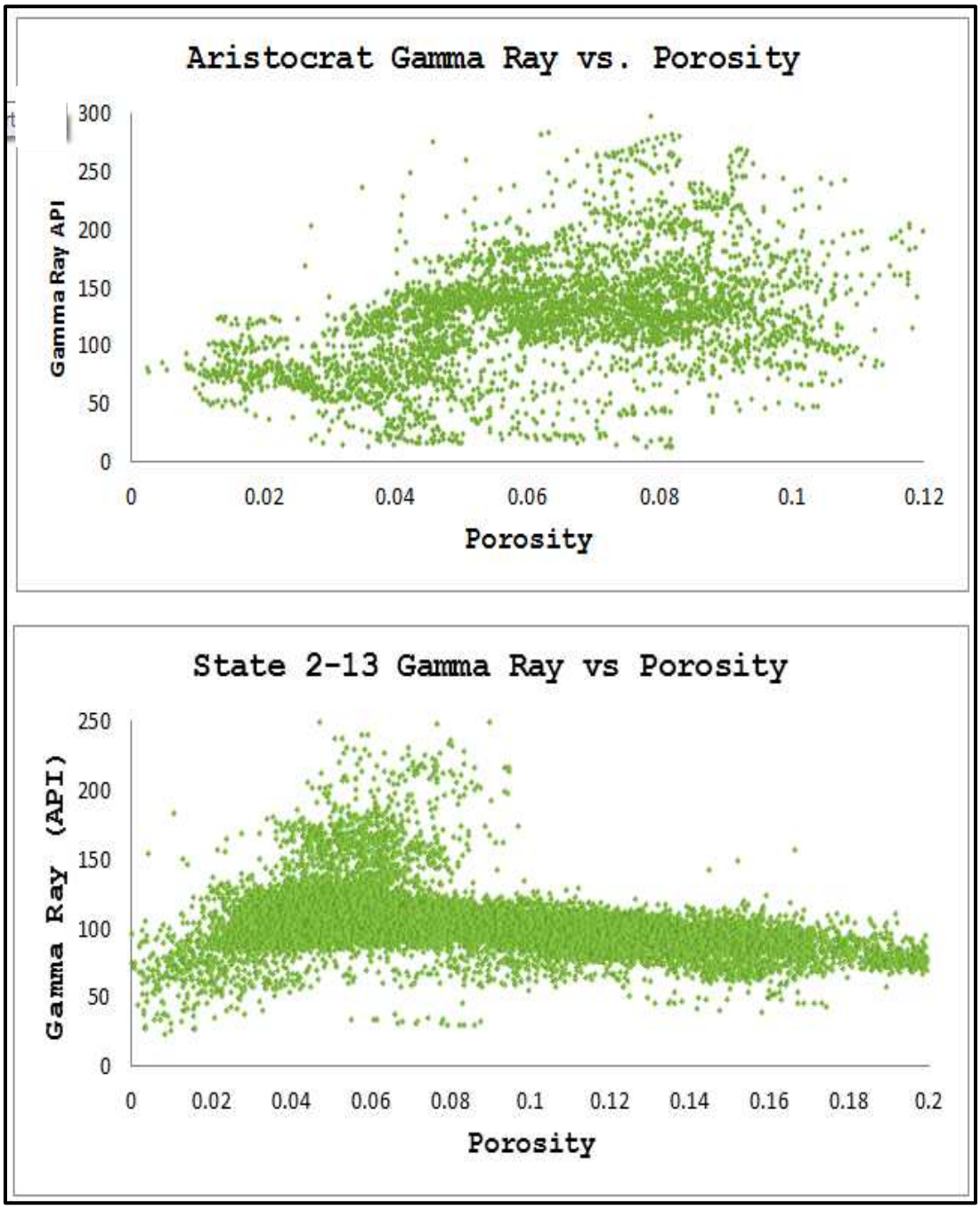

Figure 2.9. Gamma Ray vs Porosity for Noble Energy Aristocrat and CO State Well 2-13Clay content has no effect on log-derived porosity values.

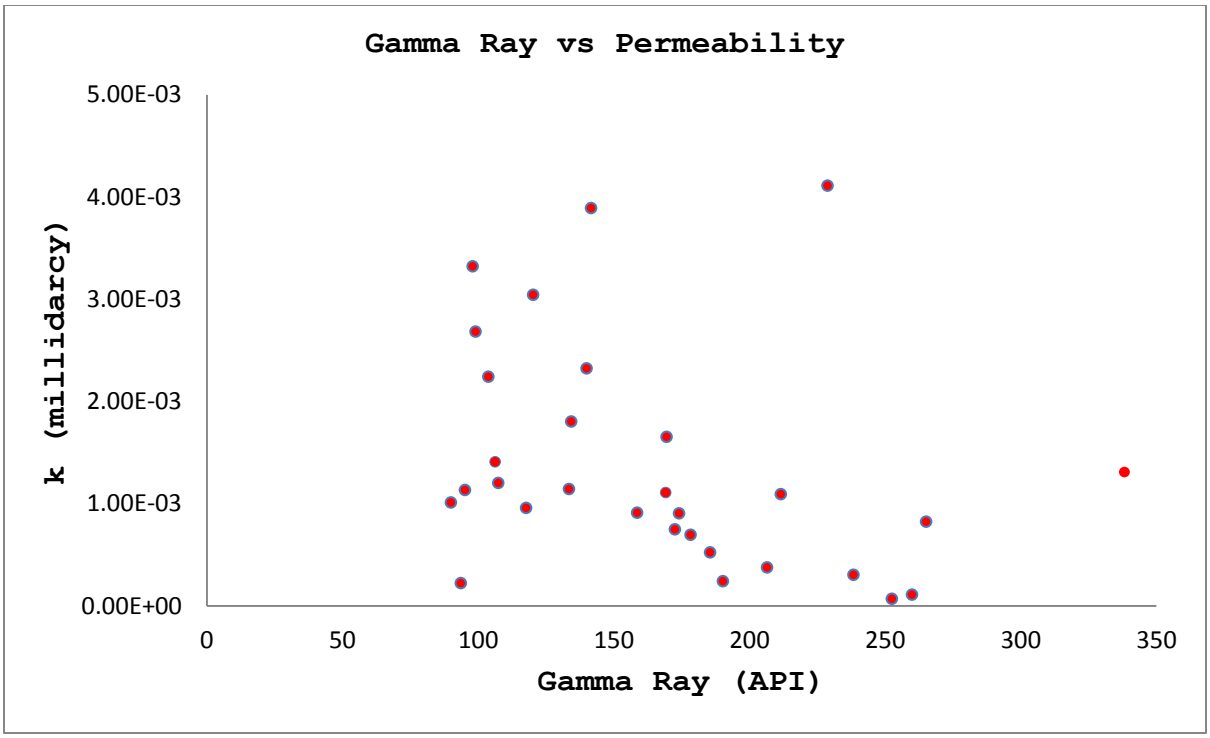

Figure 2.10. Gamma Ray vs Permeability for EOG Resources Lamotta 5-01M well. Permeability decreases with increasing clay content.

To conclude, our examinations of the Niobrara reinforce our motivation for this study. Due to the geologic characteristics of the formation, enhanced completion techniques are required for hydrocarbon production. The next chapter discusses laboratory methods, Elastic Medium Theory, and Effective Medium Theory.

CHAPTER 3

EXPERIMENTAL SPECIFICATIONS AND SAMPLE OVERVIEW

3.1 Introduction

This chapter discusses the experimental and quantitative methods. The topics discussed are chalk and marl composition, the Uniaxial Compressive Test and the Thick-Walled Cylinder Test, and equations required to measure the elastic parameters. A brief discussion of Effective Medium Theory is included.

3.2 Samples Tested

The samples tested were cored from the D chalk and D marl blocks extracted from the Cemex quarry (see Figures 2.7,8). The term "chalk" is used for conciseness, but the "chalk" facies are marls by definition. The Smoky Hill member facies have considerable clay and quartz content, and the predominant clay in the D chalk and D marl is illite-smectite. The D Marl has higher clay content than the D Chalk, as shown the XRD analysis results in Table 3.1.

Table 3.1 Mineralogy of D Chalk and D Marl, Cemex Quarry, Lyons, CO.

Sample	Calcite	Mg Calcite	Dolomite	Ankerite	Quartz	Plagioclase	Pyrite	Anhydrite	Kaolinite	Illite-Smectite	Sum non-clay	Sum clay
D Chalk	48	0.4	0.6	4	16	5	0.9	0.6	2	22	75	25
D Marl	37	1	1	1	14	6	4	0.8	3	32	65	35

The Archimedes method was used to determine grain density and porosity, and the results are shown in Table 3.3. Effective porosity in the Smoky Hill member decreases as clay increases. This is important to note since clay content doesn't affect log-derived porosity, as discussed in Chapter 2. Since kerogen content in the samples is low it might be maintained that clay content carries most of the pore volume in these facies. A summary of the samples tested is shown in Table 3.2. The XRD-analyzed mineral components have been grouped for ease of modeling.

Table 3.2 Summary of D chalk and D marl samples for geomechanical characterization

Facies	In-situ stress (MPa)	TOC (wt %)	Dry Bulk Density (g/cc)	R_o (unitless)	QFP * %	Carbonate %	Clay %	φ %	Clay Preferred Orientation	orientations tested (degrees to bedding)	E GPa	v unitless
Marl	1.84	5.2	2.68	0.7	24	40	35	3.8	yes	0^o,45^o,90^o	35	0.33
Chalk	1.84	1.3	2.68	0.7	21.9	53	25	4.3	no	0^o,45^o,90^o	32	0.26

*Quartz, Feldspar, Pyrite

Increasing proportions of platy mineral grains tend to increase the anisotropy of materials (Thomsen, 1986; Vernik and Nur, 1992; Sone and Zoback, 2013), and observed stiffness in these materials increases with increasing measurement angle. Thin section images of the D chalk and D marl are shown in Figure 3.1 below. The samples for the D chalk contain flattened calcispheres and foram fragments. Organic content is roughly 0.65 %, and there is no observed preferential clay orientation. The D marl samples contain similar fossil content as the chalks, but preferential clay orientation is observed. This is likely the primary contributor to D marl anisotropy. Organic matter content was greater for the marl samples, where TOC measures 2 %. The clay content present in the D facies is mostly illite or mixed layer illite-smectite (10%-25% expandability). Other minerals, such as Plagioclase-Feldspar, Pyrite, Anhydrite, and Kaolinite

are present, but they comprise less than a few percent of the total rock volume. For modeling effective media they are each grouped as “soft” or “stiff” components.

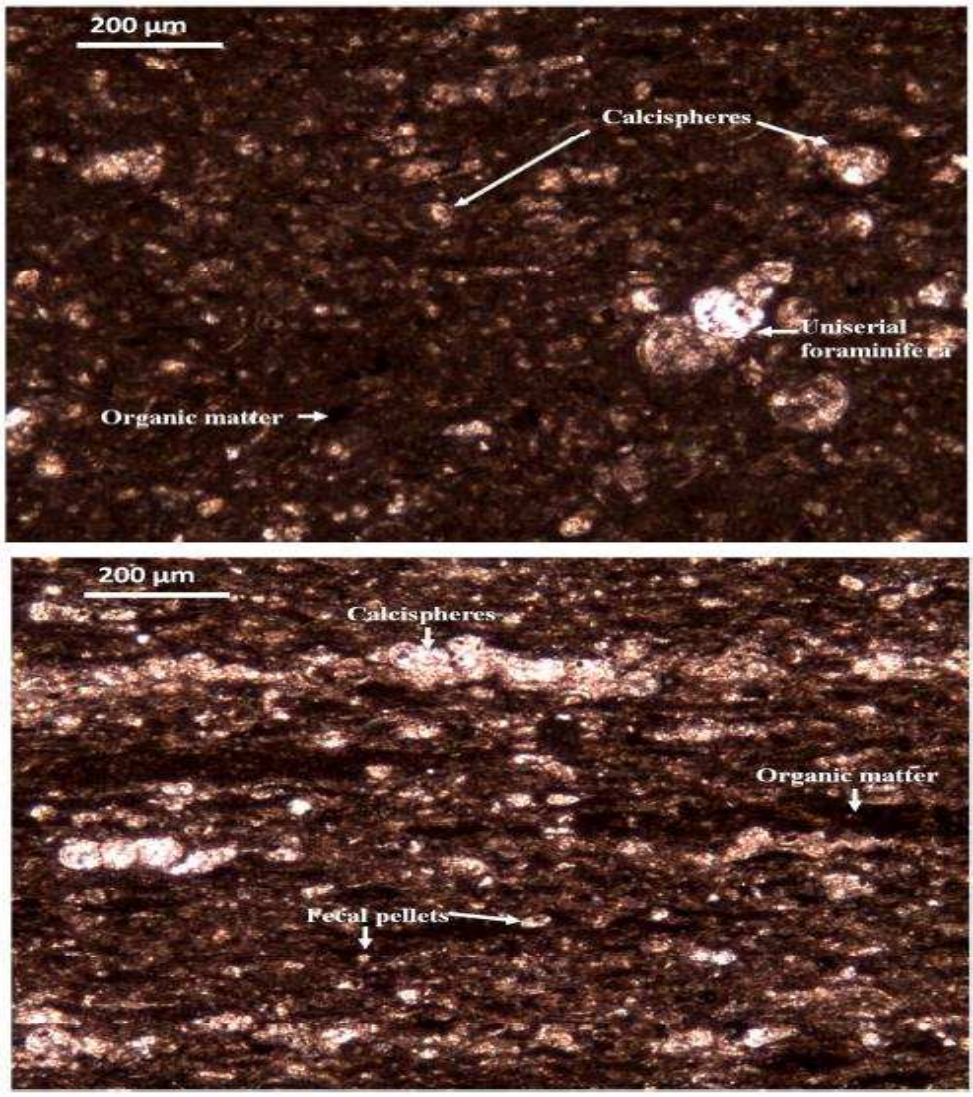

Figure 3.1. Annotated thin section images of the D Chalk (top) and D Marl (bottom). Samples taken from Cemex quarry, Lyons, CO. Image sourced from Maldonado (2010).

Figure 3.1 illustrates that the micro-fabric of the D chalk and D marl is primarily fine-grained calcareous matrix, fine-grained clays and detrital silt, biotic fragments, and organic materials. Anisotropy in shales generally originates from preferential clay orientation, low-aspect

ratio organics, or fractures (Vernik and Nur, 1992; Bakulin, 1999; Sil, 2013; Sone and Zoback, 2013). Based on the thin-section imagery (Figure 3.1), we expected the D marl to exhibit greater anisotropy than the chalk due to the observed clay orientation and low-aspect ratio organics. The higher clay content also means that the marl is more compliant. Since the Niobrara is laterally heterogeneous (Pollastro and Scholle, 1986), and clay fabric loses preferred orientation below some critical content (Sone and Zoback, 2013), and we expect that small-scale anisotropy in the Niobrara is widely varied. Figure 3.2 shows that the D chalk and D marl in the Aristocrat well differs from our samples collected at the Cemex quarry.

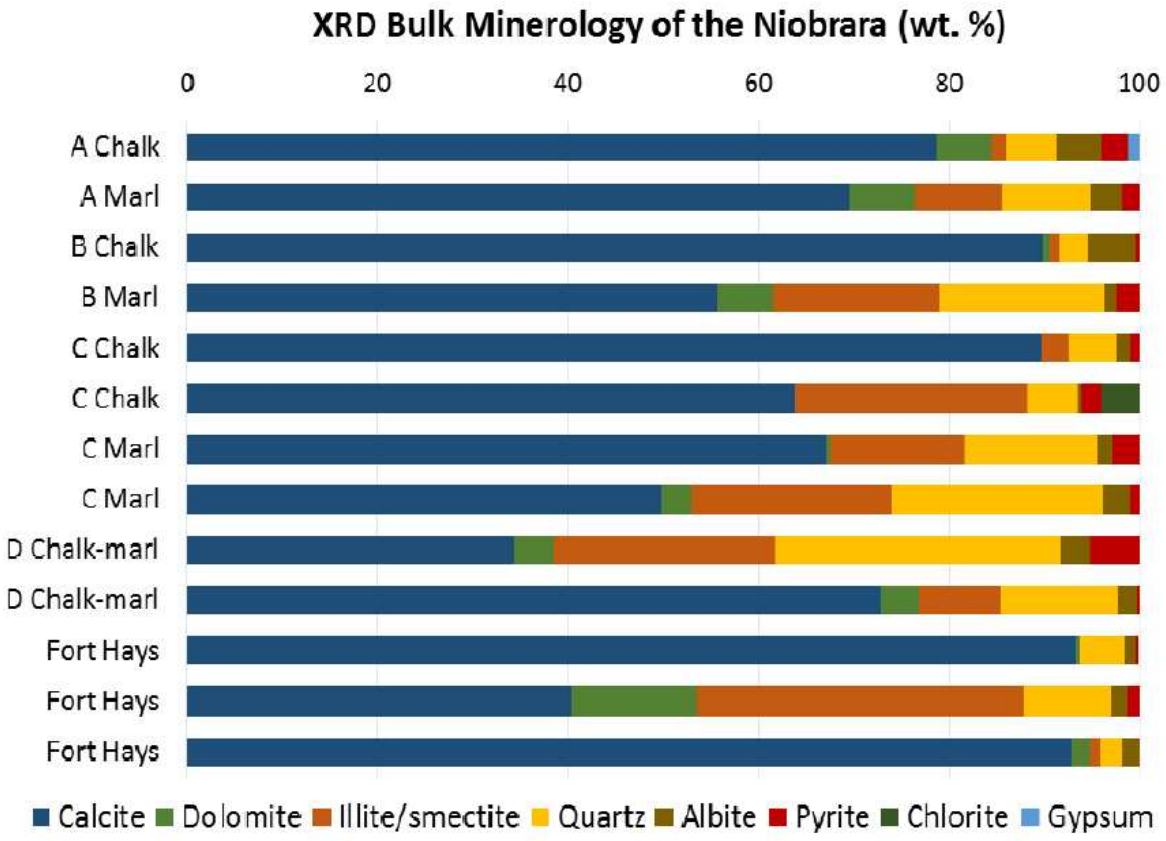

Figure 3.2 XRD mineralogy for the Aristocrat well, Niobrara Formation, Wattenberg Field, CO. The D facies down this well differs from that observed at the Lyons Cemex quarry. The Niobrara, as it is widely known, differs across various locations. Image sourced from ElGhonimy (2015).

This means that in some wells the Niobrara may contain anisotropy in some facies, especially those with higher clay content, but may not exhibit the same anisotropy at other locations. As shown by Vanorio et al. (2010), maturity of shales also plays a critical role in anisotropy and velocity response.

3.3 Experiments

Hydrofracture models require accurate estimation of the minimum horizontal stress. Young's modulus, *E,* Poisson's ratio, *v,* overburden stress, σ_v, pore pressure, $\sigma_{pp,}$ and the Biot's coefficient, α, are required inputs. Hydrofracture models in unconventional reservoirs benefit when the anisotropic properties of *E* and *v* are estimated (Higgins, 2008). The purpose of the laboratory experiments was to measure the static and dynamic properties of the D chalk and D marl to estimate stress/strain relationships and measure the anisotropic elastic constants. I prepared core plugs for each D chalk and D marl facies angle, 0^0, 45^0, and 90^0, and affixed semiconductor and/or foil strain gauges, two vertically and two horizontally, to each core plug. The core plugs each measured 2 inches in length and 1 inch in diameter, consistent with ISTM laboratory standards. Once the cores were prepared, I attached wires to the tails of the strain gauges and placed the individual cores in a hydraulic press (Figure 3.3). To measure the stress applied I used a load cell that was positioned atop the sample. TracerDAQ software was used for data collection.

Strain gauges are used to measure static moduli. The strain calibration factor, ε_{cal}, is written:

$$\varepsilon_{cal} = \frac{1}{GF}\left(\frac{R_g}{R_{cal}+R_g}\right), \tag{3.1}$$

where GF is the gauge factor, which is 155 for semiconductor gauges and 2.11 for the foil gauges. Higher GF means the gauge is more sensitive to strain. R_g is the gauge resistance, 1000 ohm, and R_{cal} is the resistance that was used to calibrate the Wheatstone bridge. R_{cal} is 49 kohm for all measurements. Strain, ε, is calculated with the following formula.

$$\varepsilon = \left(\frac{\varepsilon_{cal}}{\Delta Vol_{cal}}\right) \Delta Vol \tag{3.2}$$

, where ΔVol_{cal} is the difference of measured bridge voltage, with and without the shunt resistor and ΔVol is the difference of voltage measured at a specific increment and at the beginning of the measurement when no stress is applied.

An aluminum standard was used for calibration. Aluminum is useful to remove errors associated with the electronics since the Young's modulus of aluminum is a known 70 GPa. Young's modulus can be defined for an isotropic medium as:

$$E_a = \frac{\sigma_a}{\varepsilon_a} \tag{3.3}$$

, where σ_a is the applied stress is and ε_a the measured strain. The static Young's modulus is thereby the slope of stress vs. strain for linear elastic materials.

A series of biaxial tests (Figure 3.4) were conducted inside a thick-walled cylinder apparatus to measure the velocities required to compute the dynamic moduli and describe the anisotropy of the two facies. Three samples from both the D chalk and D marl were tested. The core plugs measured were cut at angles of 0^0, 45^0, and 90^0 with respect to bedding. For the dynamic measurements, I also maintained a 2:1 length to diameter ratio. Once the core plugs were prepared they were placed between two transducers with acoustic couplant. The transducers were premeasured to ascertain the travel time contribution of the instrument. The

sample and transducers were covered with heat shrink tubing and epoxy to keep oil from seeping into the system and causing errors and/or malfunctions.

Once the sample was ready for testing, it was placed atop an axial loading piston, and fixed into place by raising the pressure to 500 psi. After the sample was oriented correctly above the piston, I connected the transducer wires to an oscilloscope and performed a check of all three waveforms (P, S1, and S2).

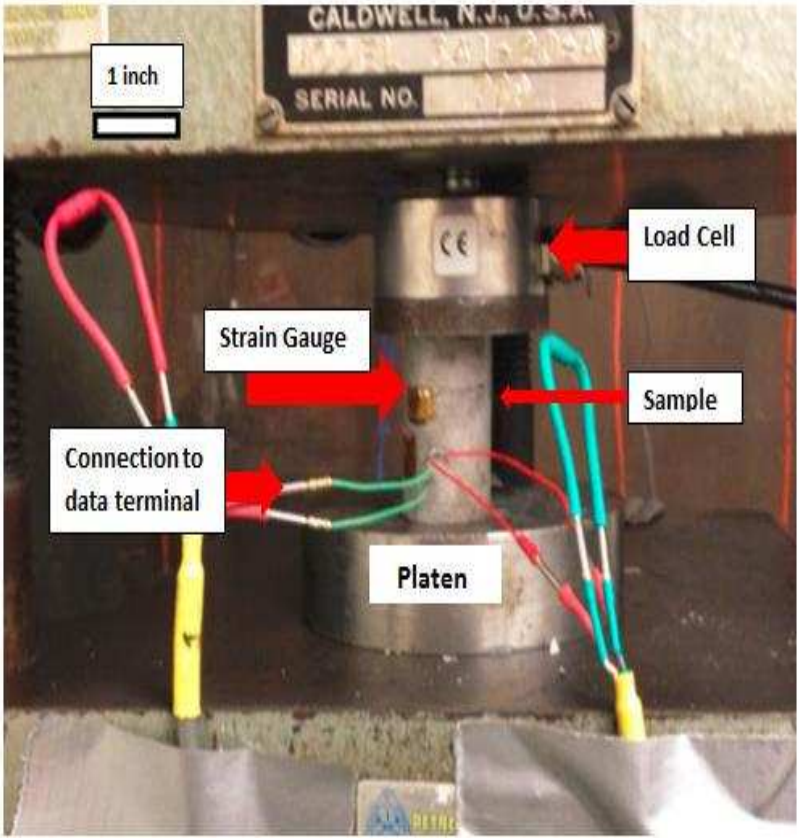

Figure 3.3. Experimental set-up for measuring static stress and strain. This method allows the static moduli and other materials properties to be measured.

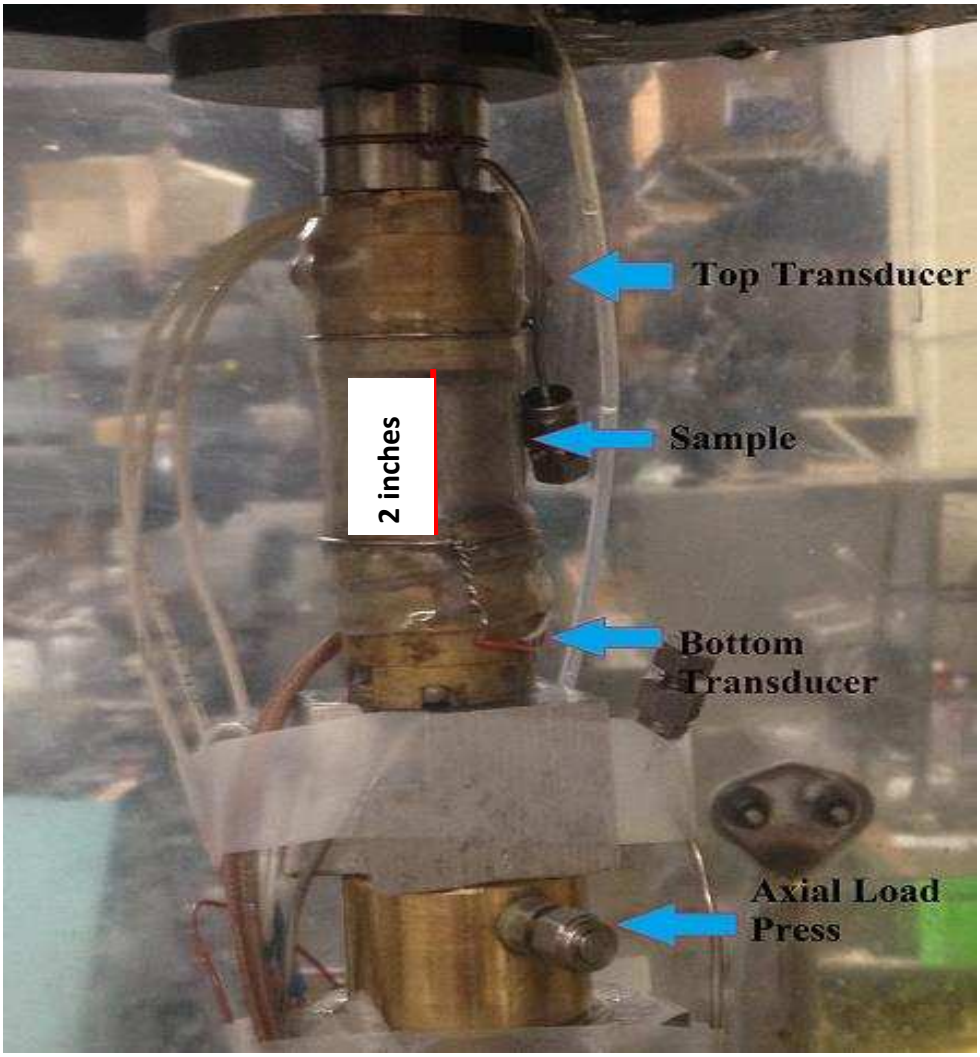

Figure 3.4. Biaxial Test set-up. A sample is placed in between two transducers and is placed in a load frame. Axial stress comes from the axial load press and confining stress comes from pumping oil into the thick-walled cylinder.

When the chamber filled with oil the confining pressure was raised until equal to the axial pressure, or about 500 psi at the beginning of the experiment. From there I slowly raised the hydrostatic pressure and captured waveforms at various increments. The range of axial and confining pressures measured was 500-7500 psi. The P, S1, and S2 waveforms captured were stored in spreadsheet format. By plotting the waveforms in Excel I was able to pick first arrivals and compute the velocity.

The performed method limited the measurements to hydrostatic loading ($\sigma_{max} = \sigma_{min}$). However, for the purposes of estimating the dry-rock anisotropy and elastic parameters this experiment was sufficient, and, moreover, prevented perturbation of the true anisotropy (Sone and Zoback, 2013). The D marl shows weak anisotropy, while the D chalk can be considered isotropic for both static and dynamic cases. The full transversely isotropic (TI) stiffness matrix was calculated using the velocity measurements and static measurements. I was able to reconcile errors and failures in my static measurements by using data from Maldonado (2010).

The velocity measurements reinforce the previous observations of preferred clay orientation in the marl samples (Figure 3.5). Velocities are highest when parallel to bedding, and the measured velocities for the 45° and 90° degree samples are nearly equal for the P-wave velocities, but vary with angle for the measured shear-waves. The measured velocity for the 0° marl sample is lowest and it is apparent that the marl is stiffest parallel to bedding. This implies that the anisotropy parameters ϵ and γ will be relatively high while the near-vertical anisotropy, illustrated by δ, will be lower. The velocity measurements for the chalk differentiate very little with angle, and the velocity measured parallel to bedding is the lowest. The lack of P-wave and S-wave velocity differentiation with respect to bedding indicate that the D chalk is isotropic. The limited velocity response is also characteristic of immature shales (Vanorio et al., 2010), and the Niobrara exhibits low R_o (~0.70) values in the area near the Cemex Lyons quarry (See Figure 2.5).

Figure 3.6 shows the measured strains for the D chalk and D marl facies. The chalk measurements again indicate isotropy or weak-anisotropy, with the facies showing little preferential behavior. The marl again indicates that stiffness is strongly related to bedding angle, and the 45° sample shows the greatest stiffness during the experiment. The 0° samples were the

most easily deformed, and based on the behavior of the 45° and 90° samples it might be inferred that the Niobrara hasn't undergone a vertical loading cycle at the Lyons quarry site. This warrants further study, for perhaps the collected samples result in greater anisotropy than what might be observed at average reservoir depth.

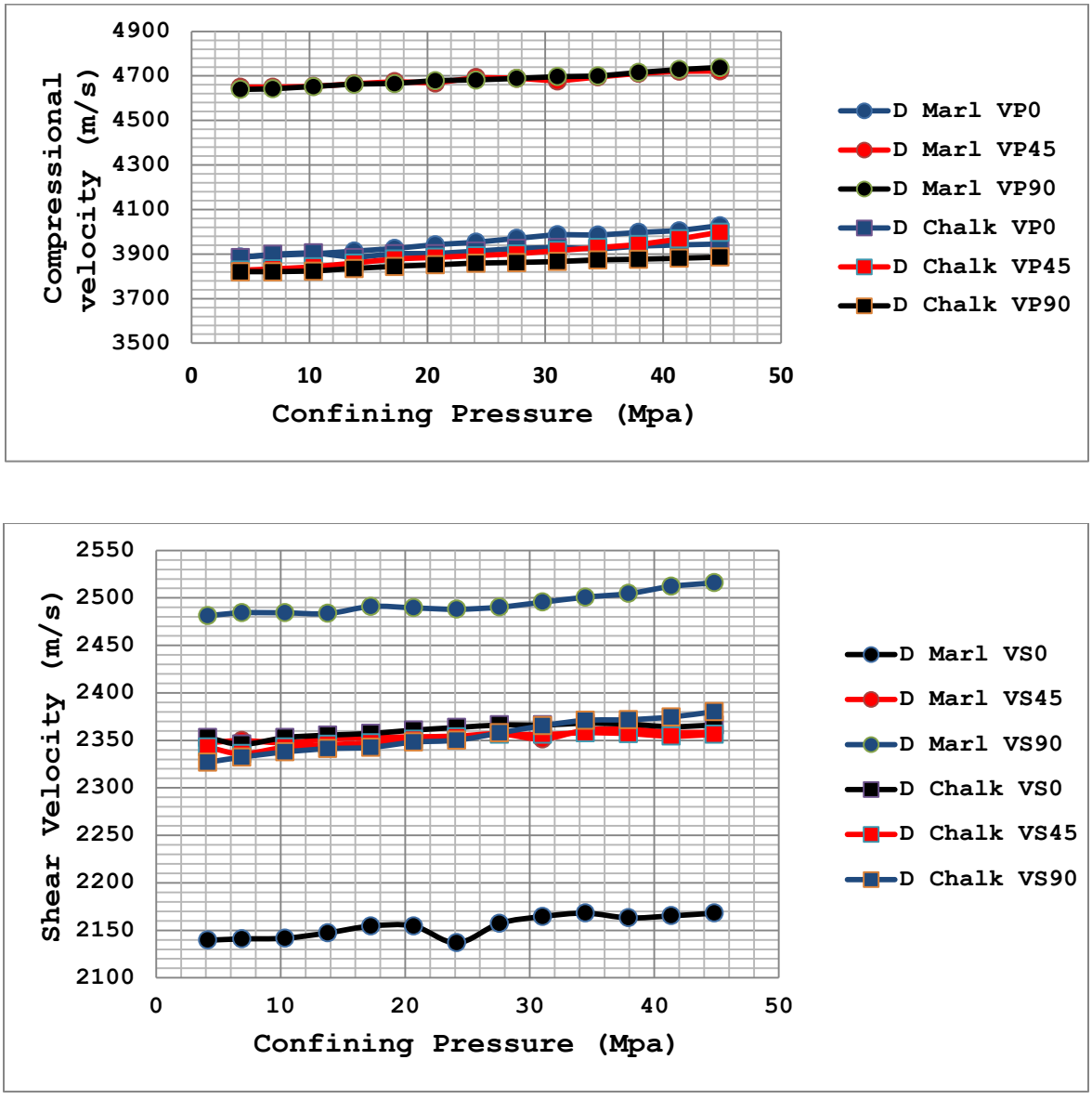

Figure 3.5 Compressional and Shear velocity for the D chalk and D marl facies. For the D marl the controlling variable for velocity is orientation to bedding plane. The velocity response is typical of peak-mature shales.

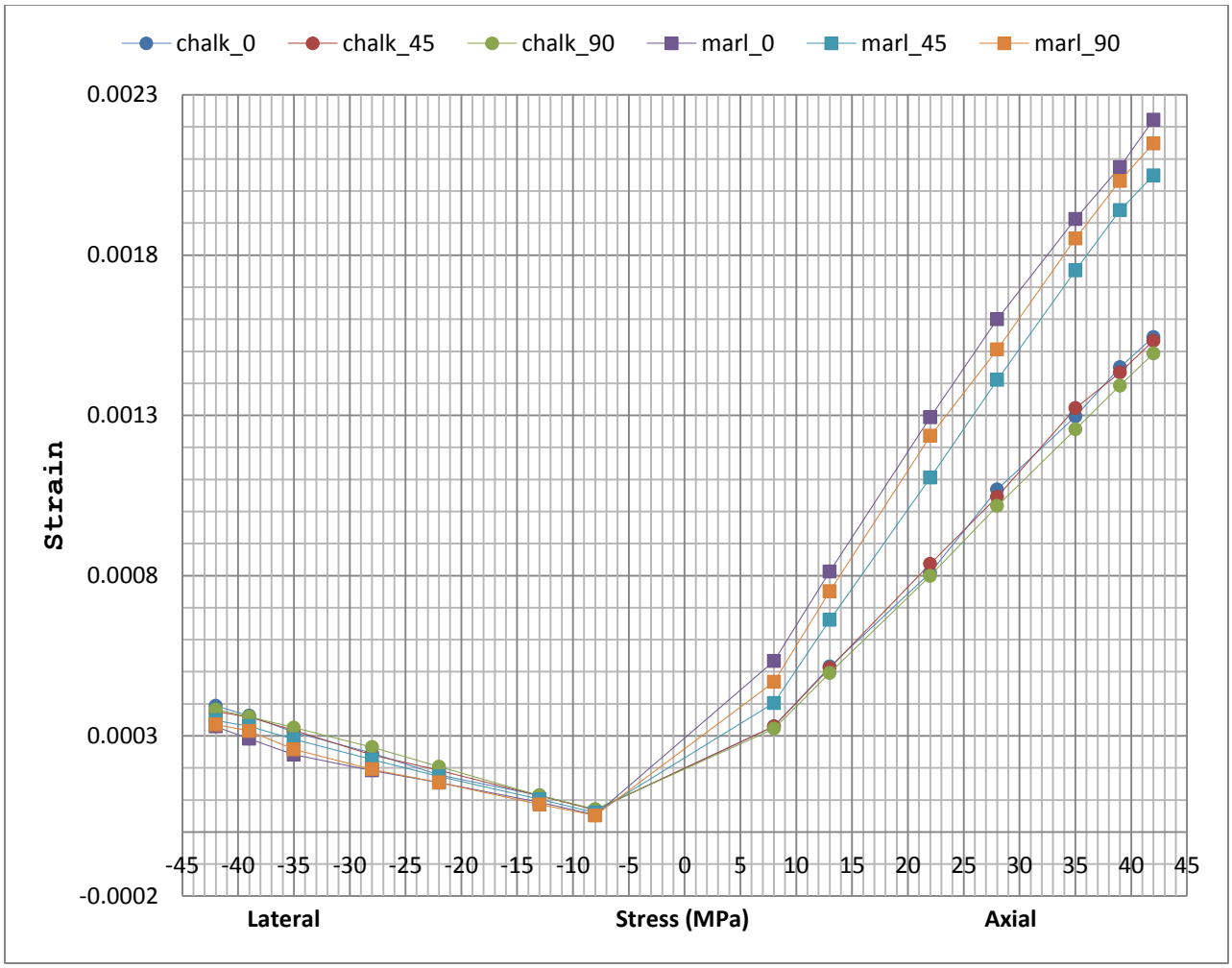

Figure 3.6. Measured strain values for the D chalk and D marl facies. The controlling variable for strain magnitudes for the facies, especially for the D marl, is soft material content and orientation with respect to bedding.

3.4 Elastic Theory

3.4.1 Isotropic form of Hooke's Law

This section discusses the isotropic and anisotropic forms of Hooke's law. In well logs where dipole sonic is not available, the isotropic elastic parameters must be used. The isotropic form of Hooke's Law can be written as (Mavko, 1998):

$$\sigma_{ij} = \lambda\delta_{ij}\varepsilon_{\alpha\alpha} + 2\mu\varepsilon_{ij} \tag{3.4}$$

Where σ_{ij} represents the elements of the stress tensor; ε_{ij} represents the elements of the strain tensor; $\varepsilon_{\alpha\alpha}$ represents volumetric strain; $\sigma_{\alpha\alpha}$ is the mean stress times 3; λ is the first Lamé parameter; μ is the shear modulus, C_{44}, or the second Lamé parameter; and δ_{ij} is the Kronecker delta.

I also show the generalized form of Hooke's law below in Equation 3.5 and show the conversion from four-index notation to two-index notation in Table 3.3. Numbers 1-3 represent compressive or tensile stress/strain along the principle axes (x, y, z), while 4-6 represent shear stress/strain (xy, yz, zx). Strain for a material is $\Delta L/L$ while stress is unit force per unit area F/A. The stiffness coefficients (C_{ij}) are related to both static and dynamic engineering terms used to describe materials and allow conversion from stress to strain, and vice versa. Two independent stiffness coefficients are required to describe and isotropic medium. The generalized form of Hooke's law is written (Mavko, 1998):

$$\sigma_i = C_{ij}\varepsilon_{ij} \tag{3.5}$$

Table 3.3. Conversion from four-index to two-index notation.

ij (kl)	*I (J)*
11	1
22	2
33	3
23, 32	4
13, 31	5
12, 21	6

$$\begin{pmatrix} C_{11} & C_{12} & C_{13} & C_{14} & C_{15} & C_{16} \\ C_{12} & C_{22} & C_{23} & C_{24} & C_{25} & C_{26} \\ C_{13} & C_{23} & C_{33} & C_{34} & C_{35} & C_{36} \\ C_{14} & C_{24} & C_{34} & C_{44} & C_{45} & C_{46} \\ C_{15} & C_{25} & C_{35} & C_{45} & C_{55} & C_{56} \\ C_{16} & C_{26} & C_{36} & C_{46} & C_{56} & C_{66} \end{pmatrix} \rightarrow \begin{pmatrix} C_{11} & C_{12} & C_{12} & 0 & 0 & 0 \\ C_{12} & C_{11} & C_{12} & 0 & 0 & 0 \\ C_{12} & C_{12} & C_{11} & 0 & 0 & 0 \\ 0 & 0 & 0 & C_{44} & 0 & 0 \\ 0 & 0 & 0 & 0 & C_{44} & 0 \\ 0 & 0 & 0 & 0 & 0 & C_{44} \end{pmatrix} \quad (3.6)$$

σ and ε are directional stress and strain of the material, and the isotropic non-zero stiffness coefficients are related to the velocities and density, ρ, by the following equations (Mavko, 1998):

$$C_{11} = \rho V_p^2 \quad (3.7)$$

$$C_{44} = \rho V_s^2 \quad (3.8)$$

$$C_{12} = C_{11} - 2C_{44} \quad (3.9)$$

There are only two independent stiffness coefficients for isotropic materials, as shown by Equation 3.6. Young's modulus (*E*), Poisson's ratio (*v*), bulk modulus (*K*), and shear modulus (*G*) have the following relationships, sourced from Mavko (1998), with velocity, density, stress, and strain given stress in an arbitrary plane *a*, and perpendicular planes *b* and *c*:

$$E = \rho V_s^2 \left(\frac{3V_p^2 - 4V_s^2}{V_p^2 - V_s^2}\right) = C_{44}\left(\frac{3C_{11} - 4C_{44}}{C_{11} - C_{44}}\right) = \frac{9KG}{3K+G} = \frac{\Delta\sigma_a}{\Delta\varepsilon_a} \quad (3.10)$$

$$v = \frac{1}{2}\left(\frac{V_p^2 - 2V_s^2}{V_p^2 - V_s^2}\right) = \frac{1}{2}\left(\frac{C_{11} - 2C_{44}}{C_{11} - C_{44}}\right) = \frac{3K-2G}{2(3K+G)} = \frac{\Delta\varepsilon_{b,c}}{\Delta\varepsilon_a} \quad (3.11)$$

$$K = \rho\left(V_p^2 - \frac{4}{3}V_s^2\right) = C_{11} - \frac{4}{3}C_{44} \quad (3.12)$$

$$G = \rho V_s^2 = C_{44} = \frac{E}{2(1+\nu)} = \frac{\Delta\tau_{ab}}{\Delta\varepsilon_{ab}} \tag{3.13}$$

Where V_p and V_s are the P- and S-wave velocities, and τ represents shear or tangential stress. Shear modulus is normally calculated from other elastic properties as direct shear stress is rarely applied to rock samples. The physical definition of each property is shown by the last term, and these terms are true for any degree of anisotropy, causing *a*, *b*, and *c* to become increasingly unique and Young's moduli and Poisson's ratios to increase in number.

To measure the static moduli the axial pressure was raised by small increments (1-2 MPa) for each axial pressure. Strain gauge failure and noisy data were thrown out, and the static data were supplemented by measurements taken at 6.9 MPa pore pressure by Maldonado (2010). Strain gauge error is 6 GPa for Young's modulus and 0.05 for Poisson's ratio.

3.4.2 Transversely Isotropic form of Hooke's law

Transversely isotropic (TI) materials are azimuthally symmetric about a single axis. In the laboratory I assumed a vertical axis of symmetry (VTI), and for the borehole computations performed I assumed a horizontal axis of symmetry (HTI). The stiffness matrix is shown below.

$$C_{ij} = \begin{pmatrix} C_{11} & C_{12} & C_{13} & 0 & 0 & 0 \\ C_{12} & C_{11} & C_{13} & 0 & 0 & 0 \\ C_{13} & C_{13} & C_{33} & 0 & 0 & 0 \\ 0 & 0 & 0 & C_{44} & 0 & 0 \\ 0 & 0 & 0 & 0 & C_{44} & 0 \\ 0 & 0 & 0 & 0 & 0 & C_{66} \end{pmatrix} \tag{3.14}$$

Figure 3.7 shows the labeled axes for a layered medium.

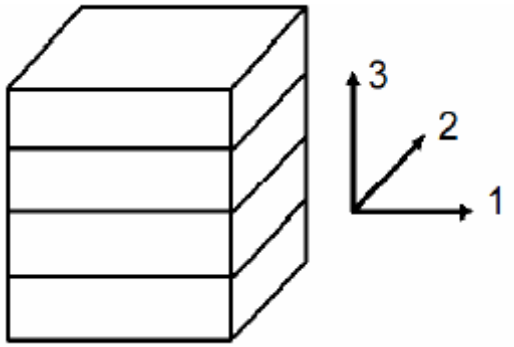

Figure 3.7. A transversely isotropic medium and the three principle axes. The 3, or vertical axis, is azimuthally symmetric in this image.

The stiffness coefficients will be used to compute the Thomsen parameters in Chapter 4. Therefore I show how stiffness can be related to velocity in the following equations from Mavko et al. (1998):

$$C_{11} = \rho V_P^2 \ (90°) \tag{3.15-3.20}$$

$$C_{12} = C_{11} - 2\rho V_{SH}^2 \ (90°)$$

$$C_{33} = \rho V_P^2 \ (0°)$$

$$C_{44} = \mu = \rho V_{SH}^2 \ (0°)$$

$$C_{66} = \frac{1}{2}(C_{11} - C_{12})$$

$$C_{13} = -C_{44} + \sqrt{4\rho^2 V_{P(45°)} - 2\rho V_{P(45°)}^2}^2 (C_{11} + C_{33} + 2C_{44}) + (C_{11} + C_{44})(C_{33} + C_{44})$$

The velocity notation in the subscripts represents the phase angle with respect to the bedding plane where the vertical direction is 0°. V_{S90} is the pure shear wave with particle motion parallel-to-bedding. Figure 3.8 shows the velocity direction and particle motion for the respective waves.

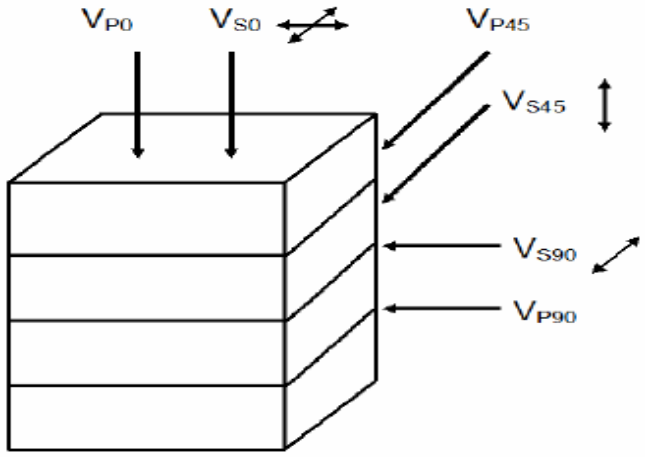

Figure 3.8. This diagram illustrates the velocity directions and particle motion directions necessary to describe TI media. Velocity direction is shown by one-sided arrows and particle motion direction is shown by double-sided arrows. Image from Havens (2011).

The engineering terms are shown by King (1964):

$$E_1 = \frac{(C_{11}-C_{12})(C_{11}C_{33}-2C_{13}^2+C_{12}C_{33})}{C_{11}C_{33}-C_{13}^2} = \frac{\Delta\sigma_1}{\Delta\varepsilon_1} \qquad (3.21\text{-}3.26)$$

$$E_3 = C_{33} - \frac{2C_{13}^2}{C_{11}+C_{12}} = \frac{\Delta\sigma_3}{\Delta\varepsilon_3}$$

$$\nu_{12} = \frac{C_{12}C_{33}-C_{13}^2}{C_{11}C_{33}-C_{13}^2} = -\frac{\Delta\varepsilon_2}{\Delta\varepsilon_1}$$

$$v_{13} = \frac{C_{13}(C_{11} - C_{12})}{C_{11}C_{33} - C_{13}^2} = -\frac{\Delta\varepsilon_3}{\Delta\varepsilon_1}$$

$$v_{31} = \frac{C_{13}}{C_{11} + C_{12}} = -\frac{\Delta\varepsilon_1}{\Delta\varepsilon_3}$$

$$K = \frac{C_{33}(C_{11} + C_{12}) - 2C_{13}^2}{C_{11} + 2C_{33} + C_{12} - 4C_{13}} = \frac{\Delta\sigma}{\Delta\varepsilon_1 + \Delta\varepsilon_2 + \Delta\varepsilon_3} = \frac{\Delta P}{\Delta V}$$

Note that C_{44} is not required to calculate the above relationships. One can design successful hydraulic fracture stimulations without measuring any velocities or stresses at 45° to bedding. To measure the bulk modulus requires uniform compression, which was accomplished during the dynamic experiments. However, the bulk modulus cannot be computed for the static case. The experiments to measure the Young's moduli and Poisson ratios are shown below in Figure 3.9.

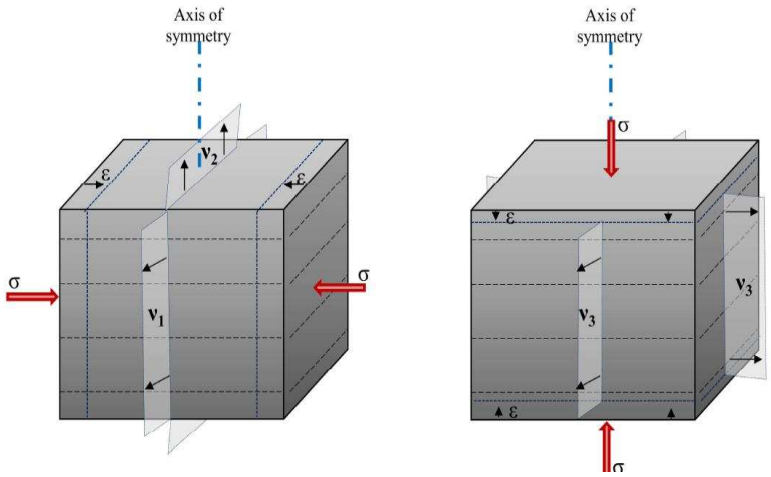

Figure 3.9. The image shows the experiments required to compute the Young's moduli and Poisson's ratios required to accurately design hydraulic fracture stimulations.

3.4.3 Effective Medium Theory

This section discusses the effective medium elastic theories applied in this study. The models discussed are Voigt-Reuss-Hill and Hudson's crack model. The Voigt-Reuss-Hill (VRH) model is applied to our elastic constant data in Chapter 5, and the Hudson's crack model is applied in Chapter 6 to see the role of cracks in causing anisotropy in our study area. VRH was chosen because of its commonality and usefulness in a mixed mineralogy system. The Hudson model was chosen for application to the lab data because the anisotropy discussed in Chapter 6 is believed to originate from vertical cracks. The derived crack density ranges between 0-0.05 for the Aristocrat well and is within the limits of Hudson's model, < 0.1 (Hudson, 1981; Bakulin, 1999). Moreover, the method applied to our well is based on Hudson's model and therefore allows comparison with our laboratory data (Bakulin et al., 1999; Sil, 2013).

The Voigt-Reuss-Hill medium is an average of the stiffest and softest possible material arrangement, and is shown by Hill (1965):

$$M_V = \sum_{i=1}^{N} x_i M_i \tag{3.27}$$

$$\frac{1}{M_R} = \sum_{i=1}^{N} \frac{x_i}{M_i} \tag{3.28}$$

$$M_{VRH} = \frac{M_V + M_R}{2} \tag{3.29}$$

, where *M* is the parameter of interest and *V, R,* and *VRH* represent Voigt, Reuss, and Voigt-Reuss-Hill, respectively. This theory is applied in Chapter 5.

Hudson's crack model will be applied to the laboratory data. Hudson's model assumes parallel, penny-shaped cracks and an isotropic background. Here I will give the equations for cracks aligned normal to the 3-axis (horizontal) in the condensed two-index notation (Hudson, 1981; Mavko et al., 1998):

$$C_{ij}^{eff} = C_{ij}^{iso} + \Delta C_{ij}^{crack} \tag{3.30}$$

The *eff* superscript represents the stiffness matrix of the cracked medium, *iso* is the isotropic background stiffness, and *crack* is the first and second order corrections from Hudson (1981) for the added crack compliance. The effective stiffnesses in the condensed two-index notation from Hudson (1981) and Mavko et al. (1998) are shown as:

$$C_{11}^{eff} = C_{11} - \frac{C_{12}^2}{C_{44}}\varepsilon_{cr}U_3 + \frac{q}{15}\frac{C_{12}^2}{C_{11}}(\varepsilon_{cr}U_3)^2 \tag{3.31-3.38}$$

$$C_{13}^{eff} = C_{12} - \frac{C_{12}C_{11}}{C_{44}}\varepsilon_{cr}U_3 + \frac{q}{15}C_{12}(\varepsilon_{cr}U_3)^2$$

$$C_{33}^{eff} = C_{11} - \frac{C_{11}^2}{C_{44}}\varepsilon_{cr}U_3 + \frac{q}{15}C_{11}(\varepsilon_{cr}U_3)^2$$

$$C_{44}^{eff} = C_{44} - C_{44}\varepsilon_{cr}U_1 + \frac{2}{15}\frac{C_{44}(3C_{11} + 2C_{44})}{C_{11}}(\varepsilon_{cr}U_1)^2$$

$$C_{66}^{eff} = C_{44}$$

$$q = 15\frac{C_{12}^2}{C_{44}^2} + 28\frac{C_{12}}{C_{44}} + 28$$

$$U_1 = \frac{16C_{11}}{3(C_{12} + 2C_{11})}\frac{1}{(1 + M)}$$

$$U_3 = \frac{4C_{11}}{3(C_{12} + C_{44})} \frac{1}{1 + k}$$

Due to the nature of this study, the aspect ratio and crack porosity are not required for modeling purposes. Hudson's crack model is used later in this study to predict how anisotropy, as measured by the Thomsen parameters (1986), changes with increasing crack density.

The following chapters discuss the results of our study. Chapter 4 is a discussion of anisotropy in the Niobrara and the applicability of the ANNIE approximation. Chapter 5 discusses the elastic constants and elastic anisotropy. Chapter 6 discusses the results of a full-waveform fracture detection inversion and its comparison to the laboratory data.

CHAPTER 4

ACOUSTIC ANISOTROPY OF THE SMOKY HILL MEMBER

4.1 Introduction

Quantifying anisotropy enables improved completion design, and it is now widely accepted that shales, due to the presence of platy clay particles, exhibit *at least* weakly anisotropic behavior (Thomsen, 1986; Sayers, 2005, Higgins, 2008). It is common to describe shales by transverse isotropy. Transverse isotropy describes rocks that have an axis of symmetry where the rock mechanical properties are equal in two directions but different in the third (Ruger, 2001; Higgins, 2008). The most common descriptors of P-wave and S-wave anisotropy are the Thomsen parameters: ε, the P-wave anisotropy; γ, the S-wave anisotropy; and δ, the near-vertical P-wave and S_V-wave anisotropy (Thomsen, 1986). These parameters are useful in seismic processing (Thomsen 1986; Tsvankin, 1996) and in-situ stress estimation (Higgins, 2008). For the Niobrara, understanding mechanical anisotropy is useful for improving stress models such as the ANNIE approximation (Schoenberg and Sayers, 1996), where δ is required and often set to zero (Higgins, 2008; Havens 2012). This chapter discusses phase versus group velocity, laboratory-derived Thomsen parameters, and log-derived Thomsen parameters.

4.2 Phase Versus Group Velocity and the Thomsen Parameters

Determining whether phase (V) or group velocity (v_{gr}) is measured for oblique bedding angles in anisotropic media is an important component for ensuring data quality (Vernik and Nur, 1992). Group velocity refers to the energy propagation, whereas the phase velocity assumes a propagating plane wave (Vestrum, 1994). When exactly parallel or perpendicular to

bedding layers, phase and group velocity are equal, but at oblique angles, and especially at 45°, they will be different. This poses challenges during the analysis of anisotropic materials. Moreover, laboratory ultrasonic tests generally measure phase velocity (Dellinger and Vernik, 1992) while borehole sonic logging, where the transducers can be approximated as point sources and receivers at sonic frequencies, measures group velocity (Hornby, 2003).

During laboratory experiments, if the flat part of the velocity surface contacts the receiver, then we claim to have measured the phase velocity. If a curved part of the velocity surface is measured then we claim to have measured the group velocity (Dellinger and Vernik, 1992; Vestrum, 1994). This means that any point on the wavefront has a representative phase and group velocity (Figure 4.1). To know what velocity is measured means knowing the proper distance (sample length/width) and correct angle.

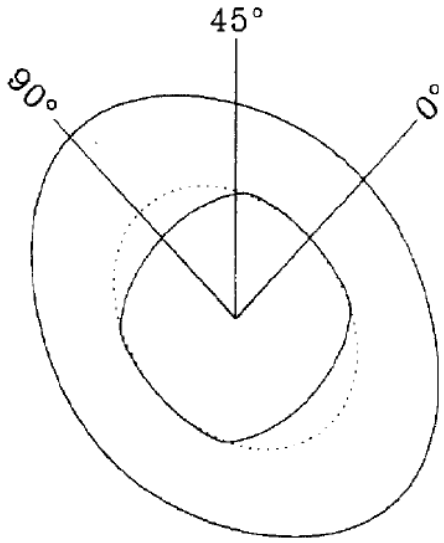

Figure 4.1. This image shows that shapes of simulated wavefronts propagating in an anisotropic medium: qP (outer curve), qSV (inner solid curve), and SH (dotted) are shown. The angle labels indicate the direction of vertical for the corresponding core plugs. Image from Dellinger and Vernik (1992).

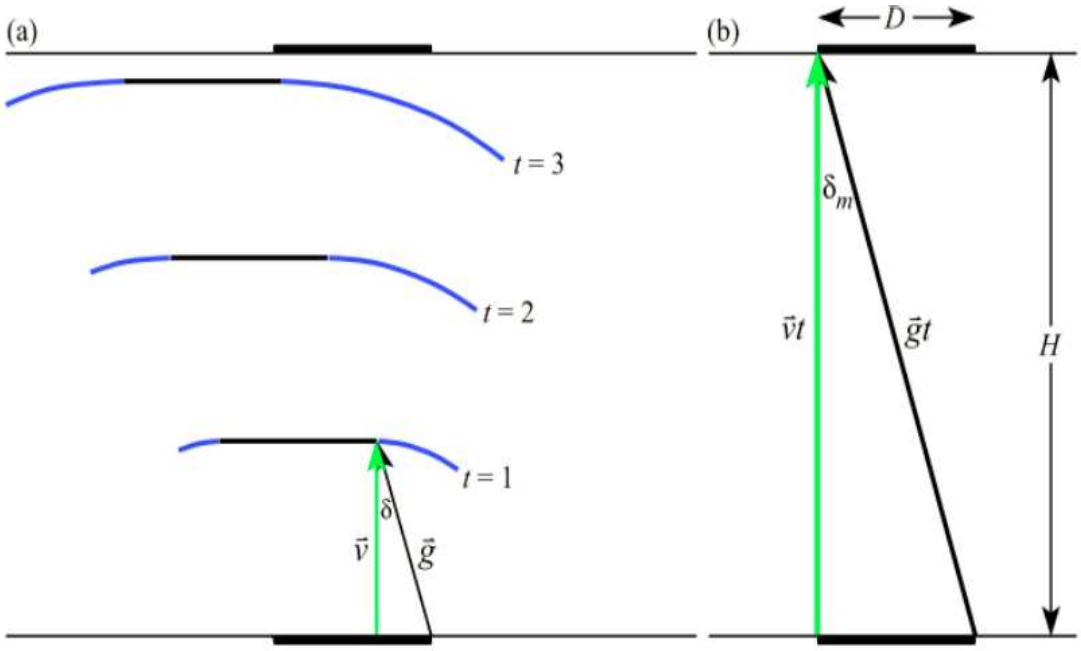

Figure 4.2. (a) The above image is an example of wavefronts propagating from a long transducer. *v* and *g* represent the phase and group velocity vectors, which are shown black and blue, respectively. δ is the difference between the group and phase angle. (b) This image illustrates the lateral displacement (D) of the plane wave. D represents the minimum transducer length necessary to measure phase velocity, and can be calculated if the height (H) and material properties are known (Havens, 2012). Image from Vestrum (1994).

Figure 4.2 (Vestrum, 1994) shows a wavefront propagating from a long transducer. If the portion of the wavefront parallel (black) to the transducer is measured then phase velocity is assumed, and if the curved (blue) portion is measured then we assume group velocity. Vestrum shows that group velocity is greater than phase velocity for a given angle. Havens (2012) summarizes the constraints, which are that:

- $v_{gr} > V$ at a given angle
- *group angle (ψ) > phase angle (θ)* if the primary plane wave is missed

Tsvankin (1996) shows the conversions between group and phase velocity and angle as:

$$v_{gr} = V\sqrt{1 + \left(\frac{1}{V}\frac{dV}{d\theta}\right)^2} \tag{4.1}$$

$$tan\psi = tan\theta\left[1 + \frac{\frac{1}{V}\frac{dV}{d\theta}}{sin\theta cos\theta\left(1 - \frac{tan\theta}{V}\frac{dV}{d\theta}\right)}\right] \tag{4.2}$$

The main issue in these equations is the derivative of the phase velocity with respect to phase angle. This can be explained by the Thomsen parameters: ε, the P-wave anisotropy; γ, the S-wave anisotropy; and δ, the parameter which controls the near-vertical P and S_v velocity response. These parameters are described by Thomsen (1986):

$$\varepsilon = \frac{C_{11} - C_{33}}{2C_{33}} \tag{4.3}$$

$$\gamma = \frac{C_{66} - C_{44}}{2C_{44}} \tag{4.4}$$

$$\delta = \frac{(C_{13} + C_{44})^2 - (C_{33} - C_{44})^2}{2C_{33}(C_{33} - C_{44})} \tag{4.5}$$

Tsvankin (1996) shows that the exact phase velocity equation becomes:

$$\frac{V^2(\theta)}{V_{P0}^2} = 1 + \varepsilon \sin^2\theta - \frac{f}{2} \pm \frac{f}{2}\sqrt{1 + \frac{4\sin^2\theta}{f}(2\delta\cos^2\theta - \varepsilon\cos^2\theta) + \frac{4\varepsilon^2\sin^4\theta}{f^2}} \tag{4.6}$$

, where

$$f = 1 - \frac{V_{S0}^2}{V_{P0}^2} \tag{4.7}$$

The plus or minus sign in front of the radical gives the P-wave velocity or the S_v-wave velocity, and shows the derivative of the phase velocity with respect to phase angle as:

$$\frac{dV}{d\theta} = \frac{\frac{1}{2}V_{P0}^2\left(2\varepsilon cos\theta sin\theta \pm \frac{\frac{1}{4}f(cot\theta(2L+4M)+N)}{(1+L+M)^{\frac{1}{2}}}\right)}{V_{P0}^2\left(1-\frac{f}{2}+\varepsilon \sin^2\theta \pm \frac{1}{2}f(1+L+M)^{\frac{1}{2}}\right)^{\frac{1}{2}}} \tag{4.8}$$

, where

$$L = \frac{4(2\delta \cos^2\theta - \varepsilon cos2\theta)\sin^2\theta}{f} \tag{4.9}$$

$$M = \frac{4\varepsilon^2 \sin^4\theta}{f^2} \tag{4.10}$$

$$N = \frac{4\sin^2\theta(2\varepsilon sin2\theta - 4\delta cos\theta sin\theta)}{f} \tag{4.11}$$

Tsvankin (2001) simplified the expression by introducing the linearized phase velocity expression,

$$\frac{dV_{p(\theta)}}{d\theta} = V_{P0} sin2\theta(\delta cos2\theta + 2\varepsilon \sin^2\theta) \tag{4.12}$$

and also simplifying the angle conversion with:

$$\psi = \theta + (\delta + 2(\varepsilon - \delta)\sin^2\theta)\, sin2\theta \tag{4.13}$$

The linearized equations are useful in seismic surveys since most sampling in seismic surveying involves low angles, but when dealing with laboratory data the measured angles are greater (θ >25°) and the equations are insufficient. The linearized equations may be applied to seismic applications once accurate Thomsen parameters are determined.

Thomsen parameters were determined via laboratory ultrasonic tests conducted on core plugs from the D Chalk and D Marl by performing calculations with wellbore dipole-sonic and density data. The Thomsen parameters were determined for the core samples by assuming a VTI case. However, when acquired wellbore data corresponds to normal-stress environments in the presence of vertical fractures an HTI medium can be assumed and anisotropy can be employed for fracture detection. Assuming a horizontal transverse isotropic (HTI) medium, such as the one shown in Figure 4.3, is necessary to calculate the Thomsen parameters down-well for fracture location. The methodology is discussed in greater length in Chapter 6, but the HTI Thomsen parameters are presented in Section 4.4.

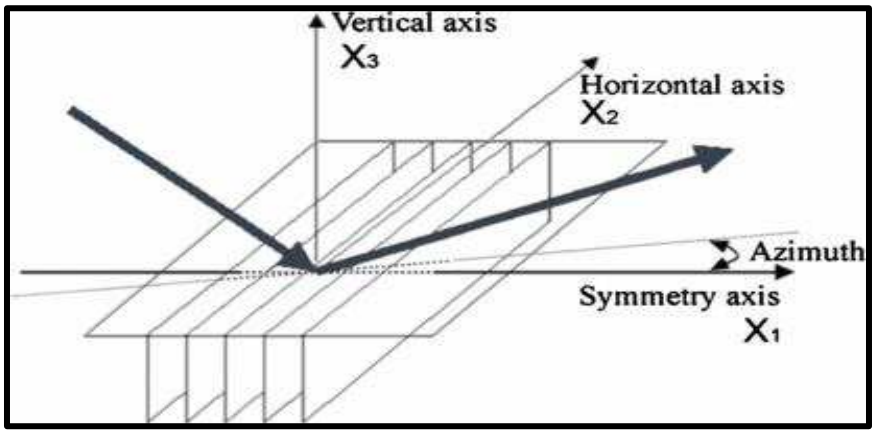

Figure 4.3. Sketch of an HTI model. The symmetry axis is intersected by the horizontal axis. Shear waves polarized parallel and normal to the horizontal axis have different velocities. In nature this phenomenon may be caused in HTI media by upturned layered rocks or vertical fractures.

In seismic surveying anisotropy may result from clay-layering or fractures. For a normally stressed environment with rocks of negligible layering, the first-order model for azimuthal anisotropy is transverse isotropy with a horizontal axis of symmetry, or HTI (Ruger, 2001). Assuming that the symmetry axis of the HTI model is parallel to the x_1 direction, the symmetry axis (x_1- x_3) is known as the *symmetry-axis* plane. Waves propagated through the symmetry axis exhibit no velocity variations with propagation angle, meaning that the medium is isotropic within the symmetry axis plane. The symmetry axis plane may also be referred to as the *fracture plane* (Ruger, 2001). Vertically propagating shear waves travel with two different velocities, one for the direction normal to the symmetry axis and one for the direction orthogonal to the symmetry axis, resulting in the shear-wave "splitting" that serves as a fracture indicator.

The relationship between VTI and HTI is similar but varies due to difference in the symmetry axes. The relationship between VTI/HTI is shown below with an analogy given by Ruger (2001):

$$C_{VTI} = \begin{pmatrix} C_{11} & (C_{11}-2C_{66}) & C_{13} & 0 & 0 & 0 \\ (C_{11}-2C_{66}) & C_{11} & C_{13} & 0 & 0 & 0 \\ C_{13} & C_{13} & C_{33} & 0 & 0 & 0 \\ 0 & 0 & 0 & C_{55} & 0 & 0 \\ 0 & 0 & 0 & 0 & C_{55} & 0 \\ 0 & 0 & 0 & 0 & 0 & C_{66} \end{pmatrix} \quad (4.14)$$

$$C_{HTI} = \begin{pmatrix} C_{11} & C_{13} & C_{13} & 0 & 0 & 0 \\ C_{13} & C_{33} & (2C_{33}-2C_{44}) & 0 & 0 & 0 \\ C_{13} & (C_{33}-2C_{44}) & C_{33} & 0 & 0 & 0 \\ 0 & 0 & 0 & C_{44} & 0 & 0 \\ 0 & 0 & 0 & 0 & C_{55} & 0 \\ 0 & 0 & 0 & 0 & 0 & C_{55} \end{pmatrix} \quad (4.15)$$

The Thomsen parameters for the HTI model are given as well, where:

$$\delta^V = \frac{(C_{13}+C_{55})^2-(C_{33}-C_{55})^2}{2C_{33}(C_{33}-C_{55})} \tag{4.16}$$

$$\varepsilon^V = \frac{C_{11}-C_{33}}{2C_{33}} \tag{4.17}$$

$$\gamma^V = \frac{C_{66}-C_{44}}{2C_{44}} \tag{4.18}$$

The Thomsen parameters for the HTI model can be related to the parameters of the VTI model with the following relationships:

$$\delta^V = \frac{\delta-2\varepsilon\left(1+\frac{\varepsilon}{f}\right)}{(1+2\varepsilon)\left(1+\frac{2\varepsilon}{f}\right)} \tag{4.19}$$

$$\varepsilon^V = -\frac{\varepsilon}{1+2\varepsilon} \tag{4.20}$$

$$\gamma^V = -\frac{\gamma}{1+2\gamma} \tag{4.21}$$

By using anisotropy parameters defined with the VTI model, the parameters for the HTI model can be determined in lab testing. This enables the determination of Thomsen parameters compatible with field seismic surveys and likewise enables calibration for inversions, such as those that entail fracture detection.

4.3 Thomsen parameters for various shale formations

Very little data concerning Thomsen parameters exists for the Niobrara. In order to calibrate our expectations we acquired data from a paper prepared by Sone and Zoback (2013). In Figures 4.4 and 4.5, ε and γ values are plotted over clay and kerogen content. Anisotropy data from the Barnett, Haynesville, Eagle Ford, Bossier/Haynesville, and Niobrara are shown. Observe that both shear-wave and compressional-wave anisotropy generally increase with increasing soft-material fraction.

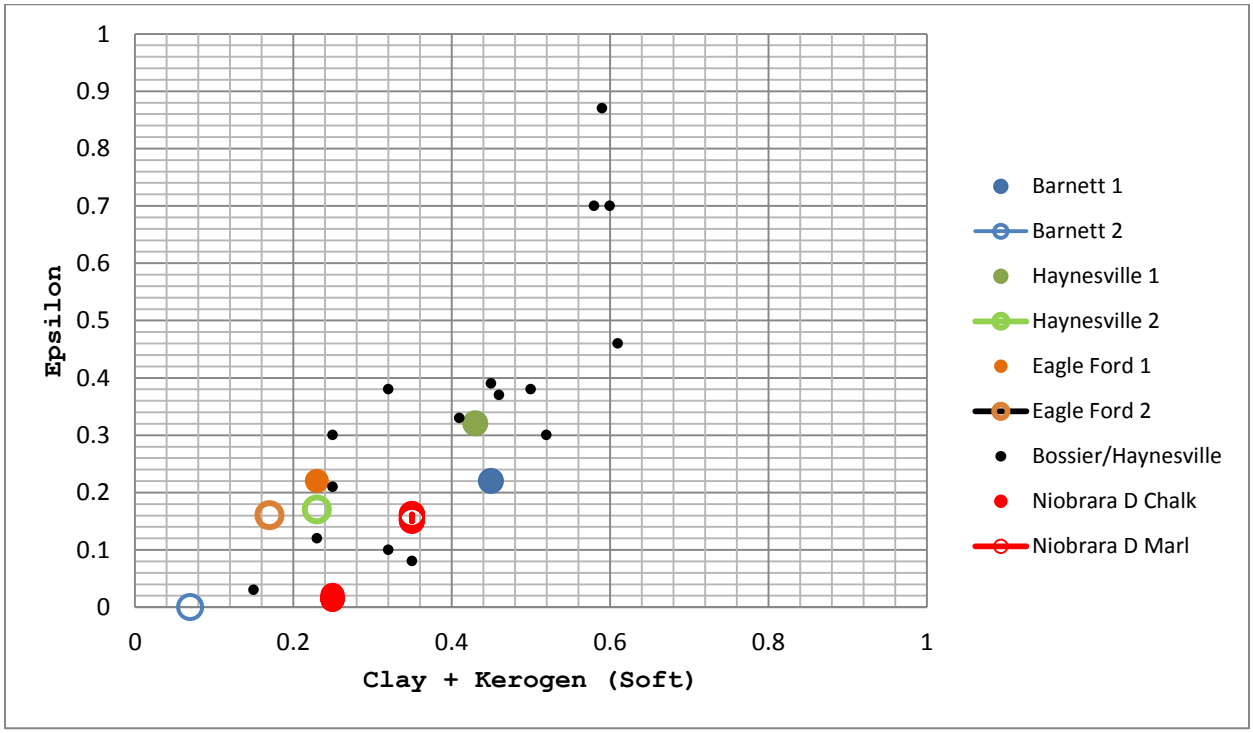

Figure 4.4. P-wave anisotropy for various shale formations. Anisotropy increases with soft-material fraction. Data sourced from Sone and Zoback (2013). Niobrara data comes from this study.

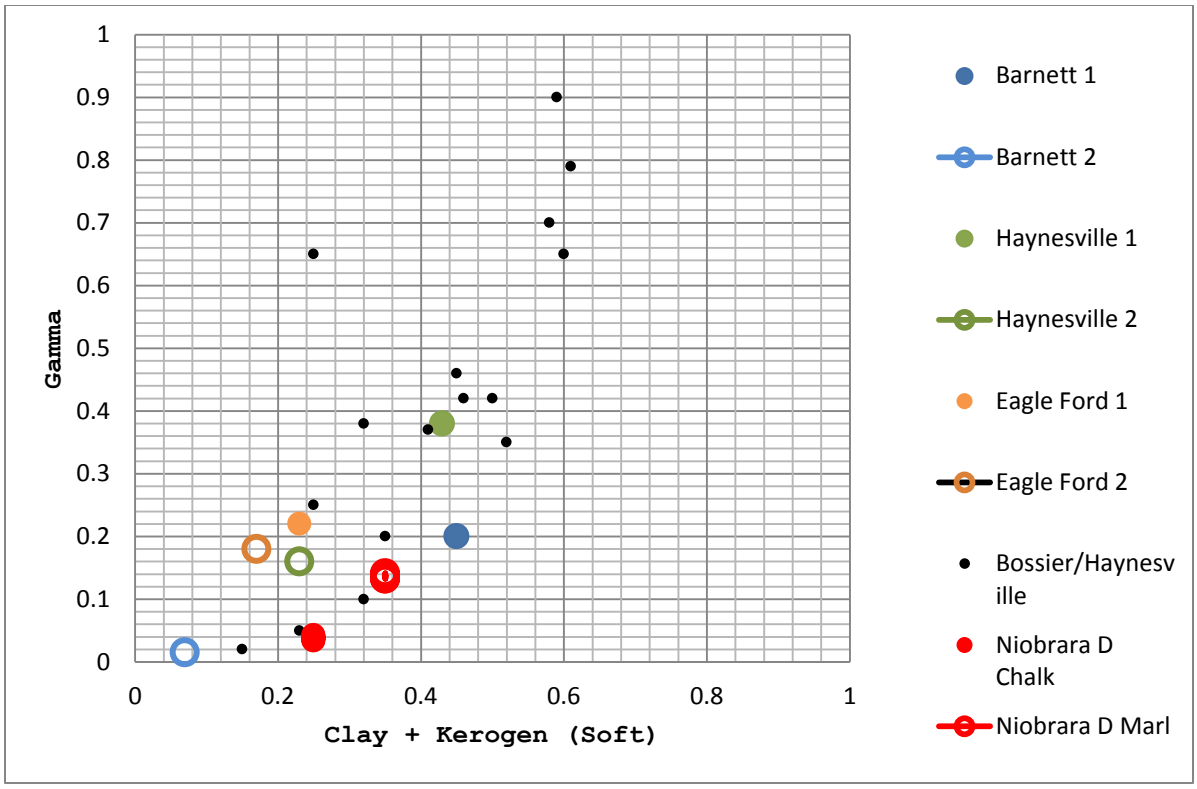

Figure 4.5. S-wave anisotropy for various shale formations. S-wave anisotropy increases with soft-material fraction. Data sourced from Sone and Zoback (2013). Niobrara data comes from this study.

A general trend is observed where directional anisotropy increases with increasing clay and kerogen content, which can be explained by the phenomenon of preferential layering. However, clay and kerogen content do not explain the entirety of the anisotropy as there are various data points falling outside the trend. These outliers may result from fractures, kerogen, or other inclusions (Vernik and Nur, 1992; Sone and Zoback, 2013).

To develop an understanding of the mathematical relationship between soft-material content and anisotropy, as well as the general relationship between ε and γ, I plotted the individual parameter relationships in Figures 4.6 and 4.7. I also plotted a general relationship between ε and γ in Figure 4.8.

The relationship between the anisotropy parameters and clay content do a poor job explaining the fabric anisotropy, as shown by the low R^2 values. My hypothesis is that clay content, organic content, compaction, and maturity each contribute a noteworthy amount and that anisotropy is a complex variable. The general relationship between the ϵ and γ for various carbonate shales is shown in Figure 4.8 as $\gamma = 1.1167\epsilon$. The correlation for these two variables is very strong, and expectedly so, since they both correspond to direction wave anisotropy. A strong relationship between γ and ε enables determination of δ, and previous work from Havens (2014), who used data from Vernik and Nur (1992) shows the predicted shale response correspondent to δ and ϵ as $\delta = 0.44\varepsilon^{0.82}$.

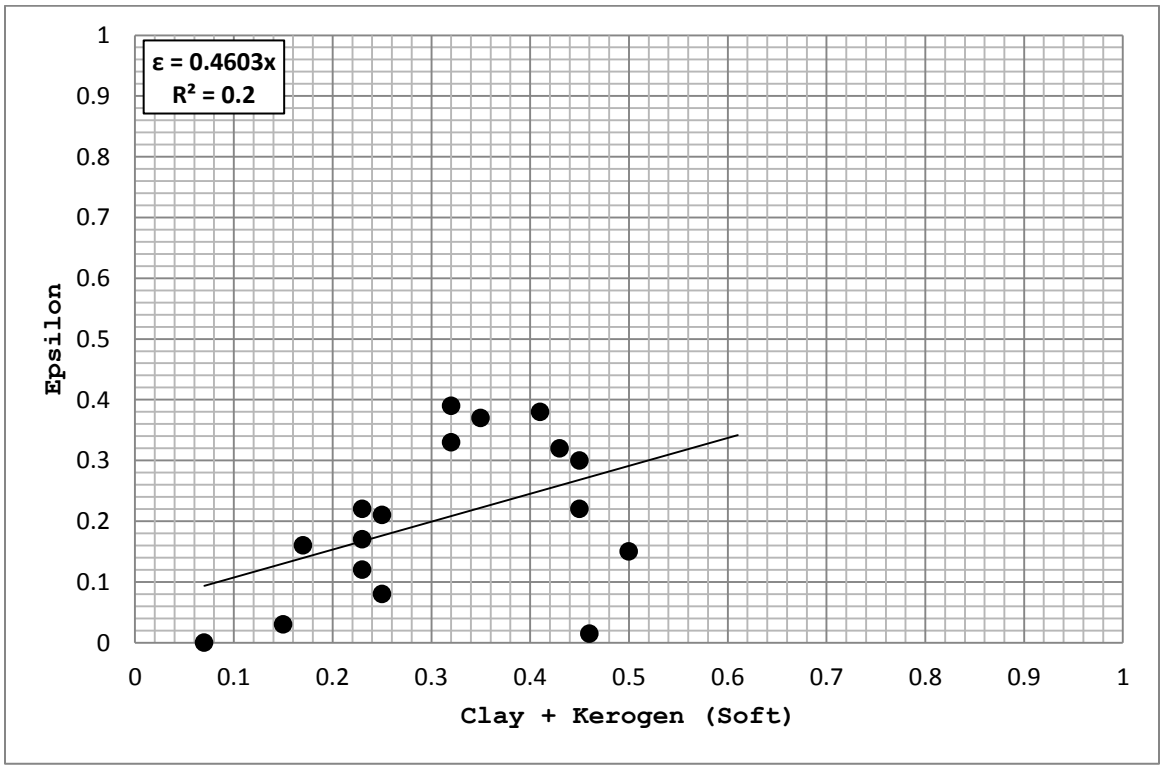

Figure 4.6 Epsilon plotted over clay + kerogen content.

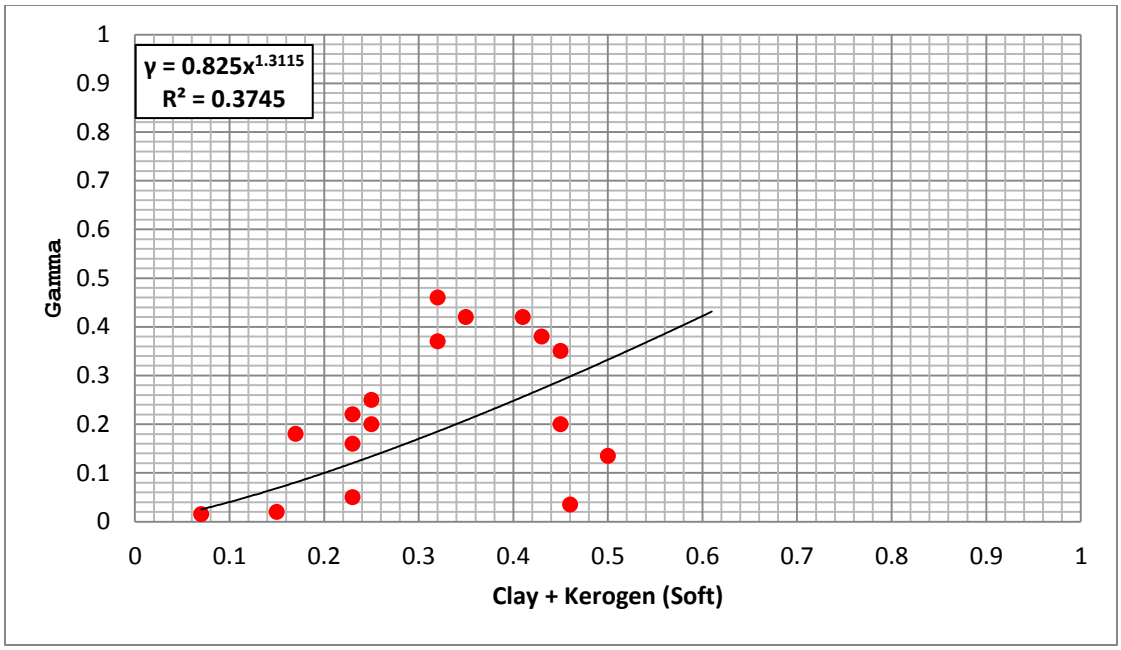

Figure 4.7 Gamma plotted over clay + kerogen content.

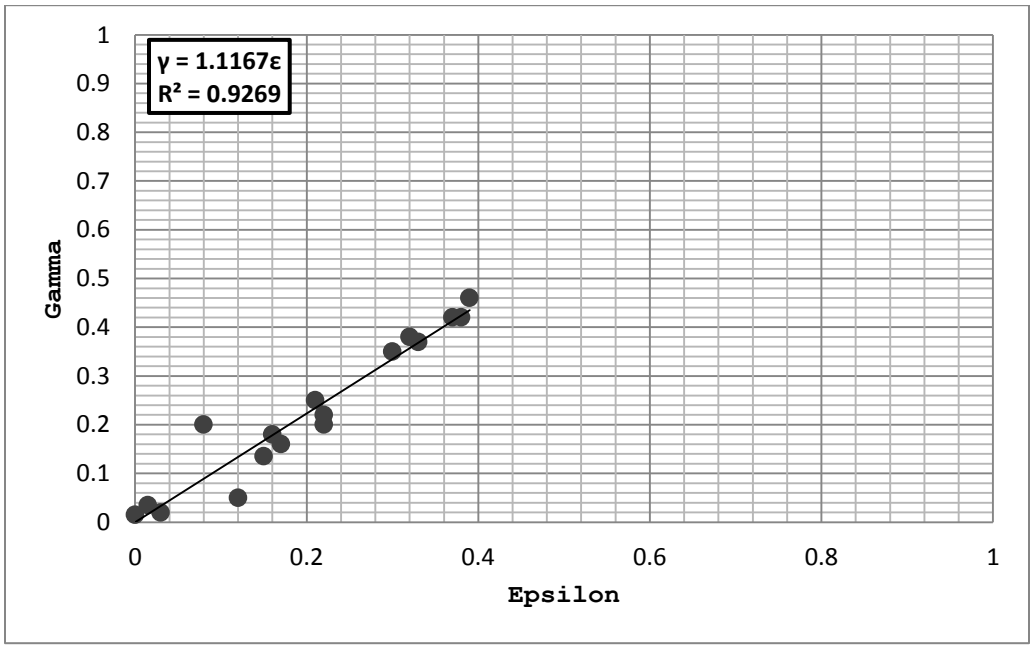

Figure 4.8 γ versus ε for various shale formations. The values show a very close correlation. Outliers were removed to enable the best fit.

4.4 Laboratory-derived Thomsen parameters

Figure 4.9 illustrates the VTI-derived Thomsen parameter values for the Smoky Hill facies. The D chalk is isotropic. ε and δ for the D chalk show a very close relationship, and their values converge above 35 MPa indicating that the experiments didn't fracture the samples and that phase velocity was successfully measured. Directional anisotropy is weak for the D chalk, ranging between 0.01-0.04 at 5 MPa, and values for ε and γ are 0.01 and 0.03 at 45 MPa. δ decreases from 0.03 to 0.01 throughout the experiment, and the D chalk may be considered isotropic at reservoir depths.

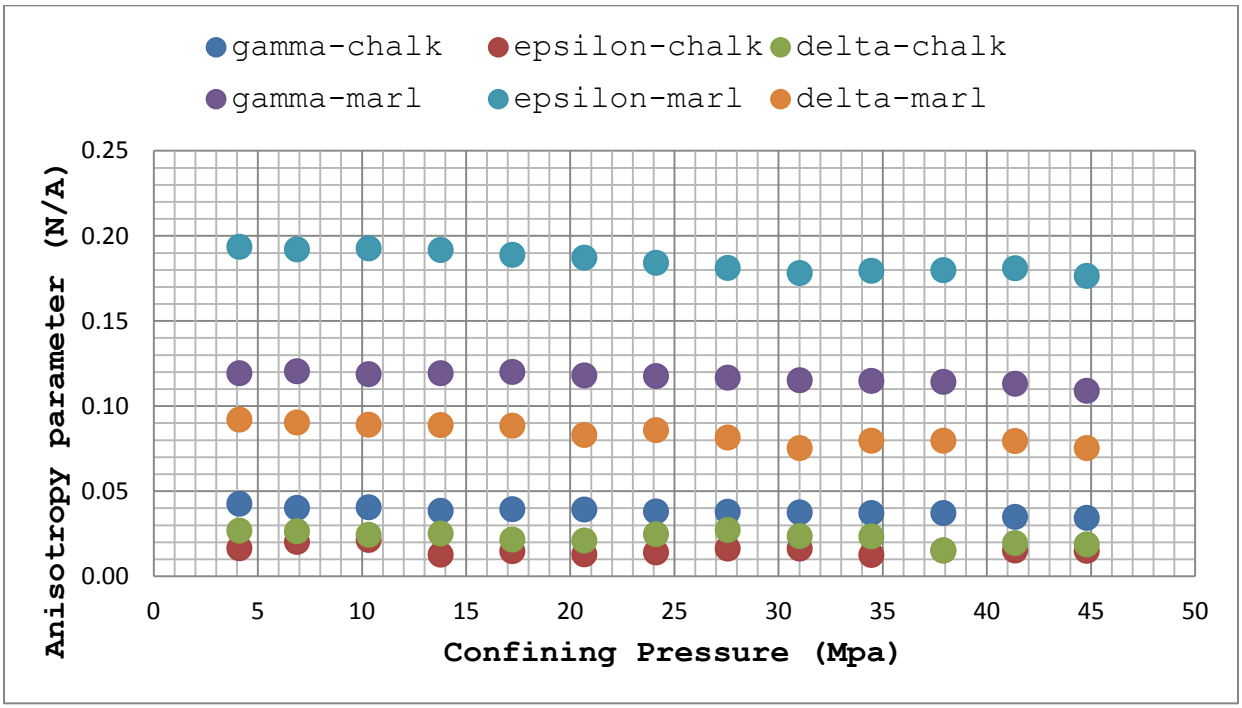

Figure 4.9. Thomsen parameters with respect to pressure for the Smoky Hill member. These parameters were determined with laboratory ultrasonic data. The values for the D chalk, shown by circles, indicate very weak anisotropy. The marl values indicate that anisotropy decreases with increasing confining pressure.

The D Marl exhibits preferential clay orientation as shown by parameters ϵ and γ. Anisotropy decreases as soft-materials, having a higher internal porosity than the stiff components, are compressed by the confining pressure. The δ values reported for the D Marl ranged between 0.09-0.07.

All anisotropy values decrease with increasing confining pressure, and the pressures applied in the lab are less than those present in the Smoky Hill member in the Aristocrat well. This means that the D chalk might exhibit *no* anisotropy at reservoir depths, and the D marl might be substantially less anisotropic. Moreover, due to lateral heterogeneities (Pollastro and Scholle, 1996) and the effects of loading-unloading cycles (Sone and Zoback, 2013), the mechanical characteristics may differ substantially from the laboratory-derived values from well-to-well, and this is discussed in a later section.

Figures 4.10 and 4.11 show the relationships between γ and ϵ for the D chalk and D marl, respectively. There is no observable relationship between the parameters for the D chalk, but a strong relationship ($R^2=0.75$) is observed between the parameters for the D marl. The relationship can be described as a power function and written as $\gamma = 0.41\epsilon^{0.75}$.

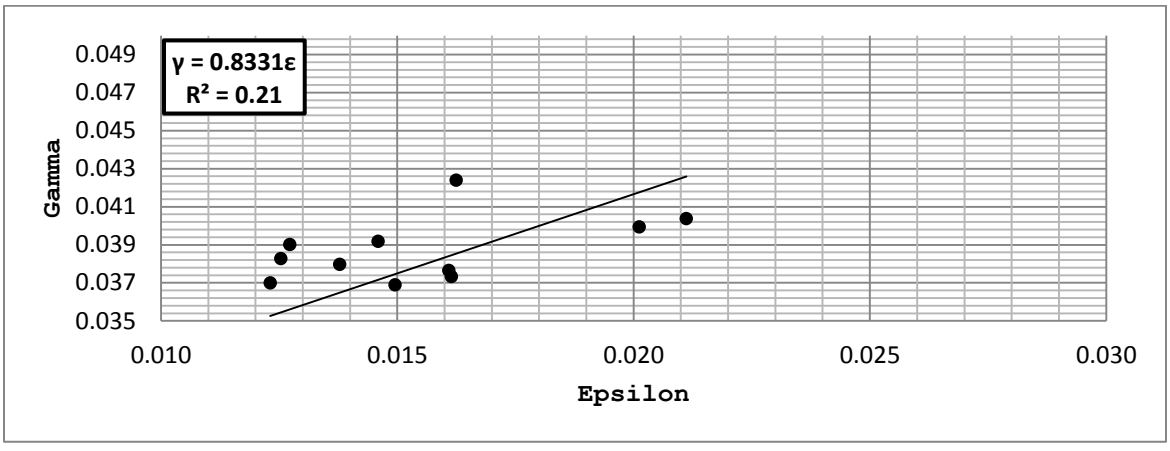

Figure 4.10 Gamma vs. Epsilon for D Chalk. There is a weak relationship between the two parameters.

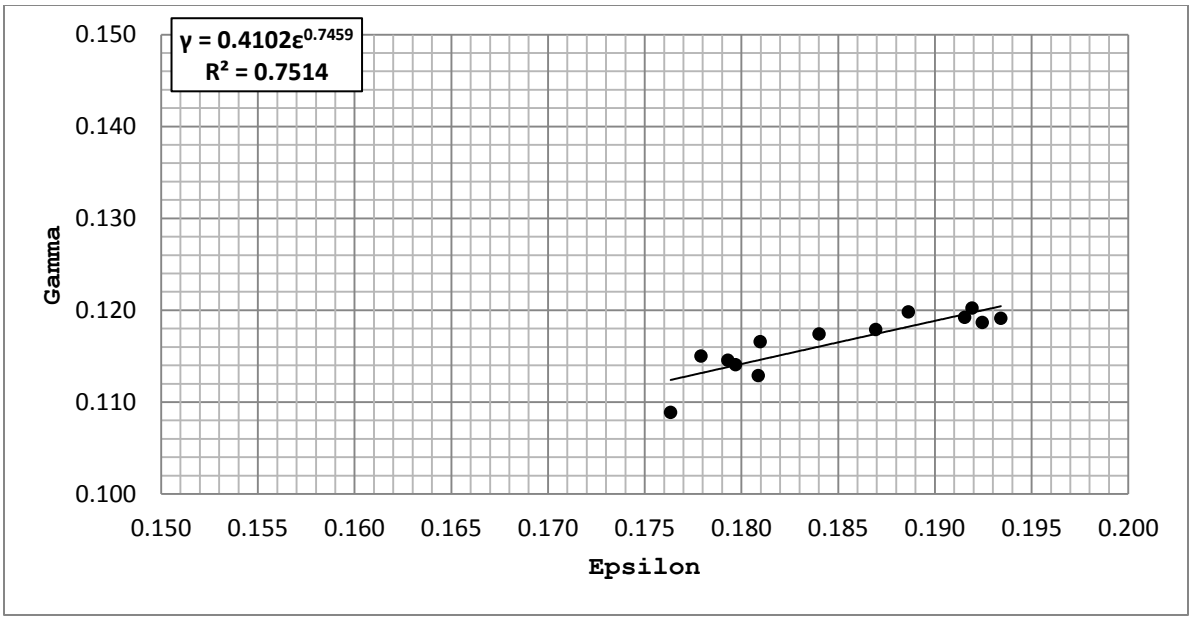

Figure 4.11. Gamma vs. Epsilon for D Marl. A strong relationship exists between the parameters.

The relationships between δ and ε are plotted in Figures 4.12 and 4.13.

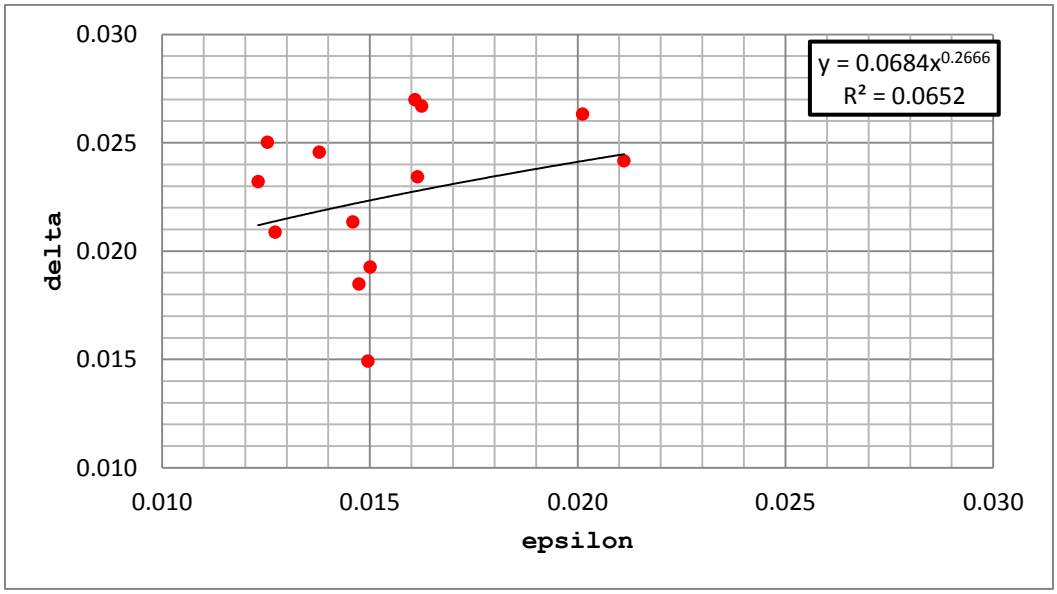

Figure 4.12 δ versus ε for the D chalk. The relationship between the parameters is poor.

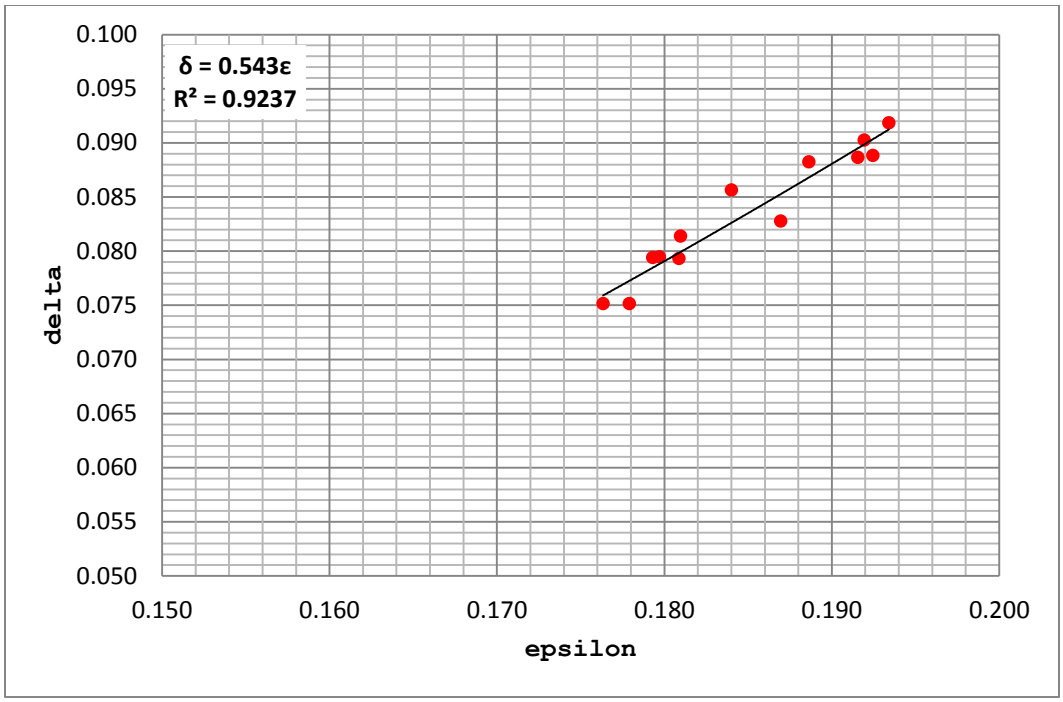

Figure 4.13 δ versus ε for the D marl. A very strong relationship is observed.

δ and ε again show a poor correlation for the D chalk but exhibit a strong (R^2=0.92) relationship for the D marl. These relationships are used to find the values of the unknown stiffness tensors for the Aristocrat well. Since both relationships are power functions, the log-derived Thomsen parameter values go to zero in the absence of anisotropy. The lab-derived values fall within the bounds given by Vernik and Milovac (2011), which are $0.4\varepsilon < \delta < 0.8\varepsilon$. They also strongly correlate to the expected shale response noted by Havens (2014).

I used Equations 4.16, 4.17, and 4.18 to convert the VTI Thomsen parameters derived from the laboratory ultrasonic tests into HTI values for quality control during the fracture detection inversion discussed in Chapter 6 (Figure 4.14). The HTI values for the D chalk again indicate isotropy, with the values for δ ranging between 0 and -0.02, ε between -0.02 and -0.01, and ranging between -0.04 and -0.03 for γ. Marl HTI values again indicate weak anisotropy, and

δ is much higher because the axis of symmetry now intersects the clay layers. This behavior should be noted for cases where steeply dipping layered media are being modeled. Since the background material is weakly anisotropic the Niobrara becomes a candidate for fracture detection inversion application.

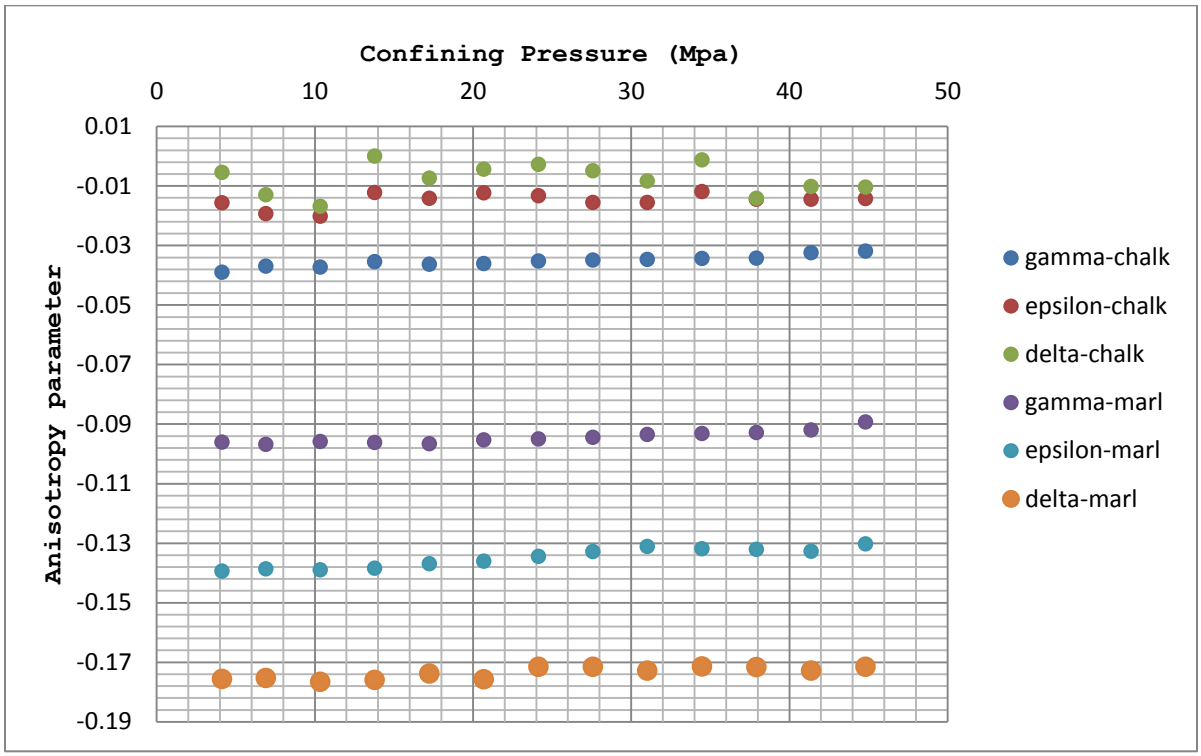

Figure 4.14. HTI Thomsen parameters for the D marl facies.

To show how pore fluid pressure affects anisotropy I used a dataset from Maldonado (2010) and plotted the results in Figures 4.16 and 4.17. In Maldonado's work, the P-wave velocities were the only velocities reported, so a relationship was required to estimate the S-wave values. To do this, I used Maldonado's reported E and v values for the horizontal and vertical

marl facies, and estimated the S-wave values with the following relationship from Mavko et al. (1998):

$$V_S = \sqrt{\frac{E}{2\rho(1+v)}} \tag{4.22}$$

I then calculated ε and γ using the velocity values. ε decreases as both pore and confining pressure increase (Figure 4.15). As fluids fill the pores of the sample it exerts stress on the sample skeleton, increasing its stiffness in all directions. Since P-waves are also sensitive to fluid content, the presence of pore fluid lowers anisotropy. It is observed that P-wave anisotropy decreases monotonically with increasing confining and pore pressure.

Figure 4.16 illustrates the effects of pressure on γ. As differential pressure increases, γ decreases, albeit along a flatter trend than that observed for ε. However, at lower differential pressures, increasing the pore pressure had twice the effect as that observed for the P-wave anisotropy. S-wave velocity is generally unaffected by fluid content since ideal fluids do not resist shear, but fluid pressure in the marl samples caused the S-wave anisotropy to decrease by 3% at 8 MPa, and throughout most of the experiment the increase in pore pressure at the various differential pressure steps affected the decrease in S-wave anisotropy more so than the precedent increase in differential pressure. This could be due to bulk skeleton stiffening caused by the pressurized fluids, and while the shear waves are insensitive to ideal fluids they will respond to changes in the bulk skeleton. Based on the results shown in Figure 4.17 one might conclude that γ is sensitive to pore pressure.

Based on the data discussed in this section I conclude that the D chalk anisotropy ranges between weakly anisotropic to isotropic, and the D marl is weakly anisotropic. The data indicates

that the mechanical anisotropy of the marl units in the Smoky Hill member is primarily determined by preferential alignment of platy minerals and decreases with increasing confining and pore pressures.

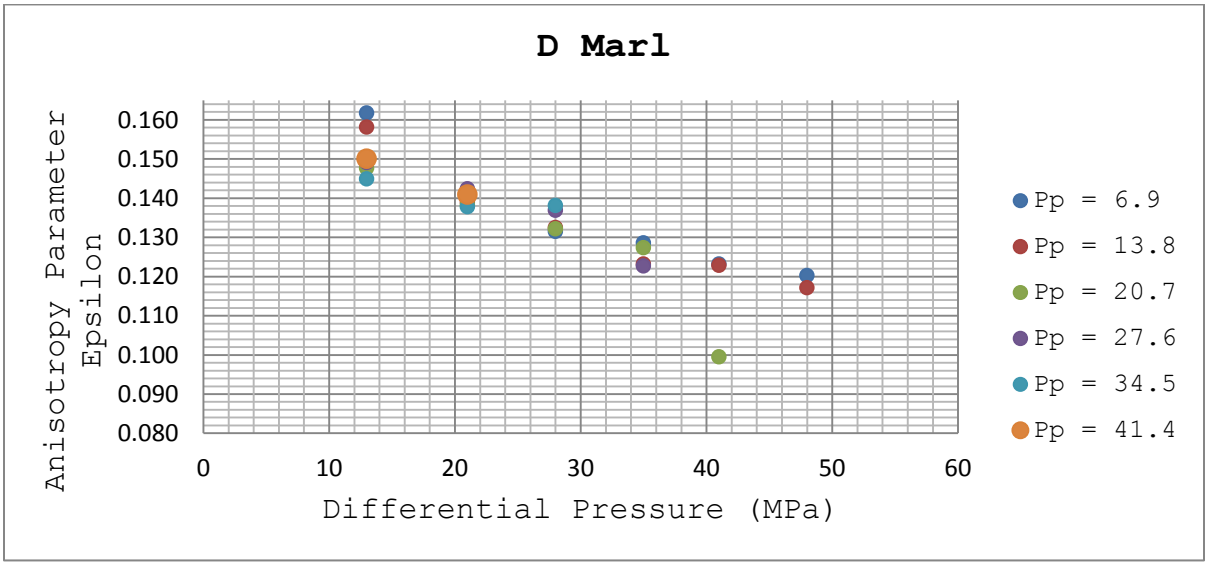

Figure 4.15 Epsilon values for the D marl at various pore and confining pressures. Epsilon, the P-wave anisotropy, generally decreases with increasing pore and confining pressures.

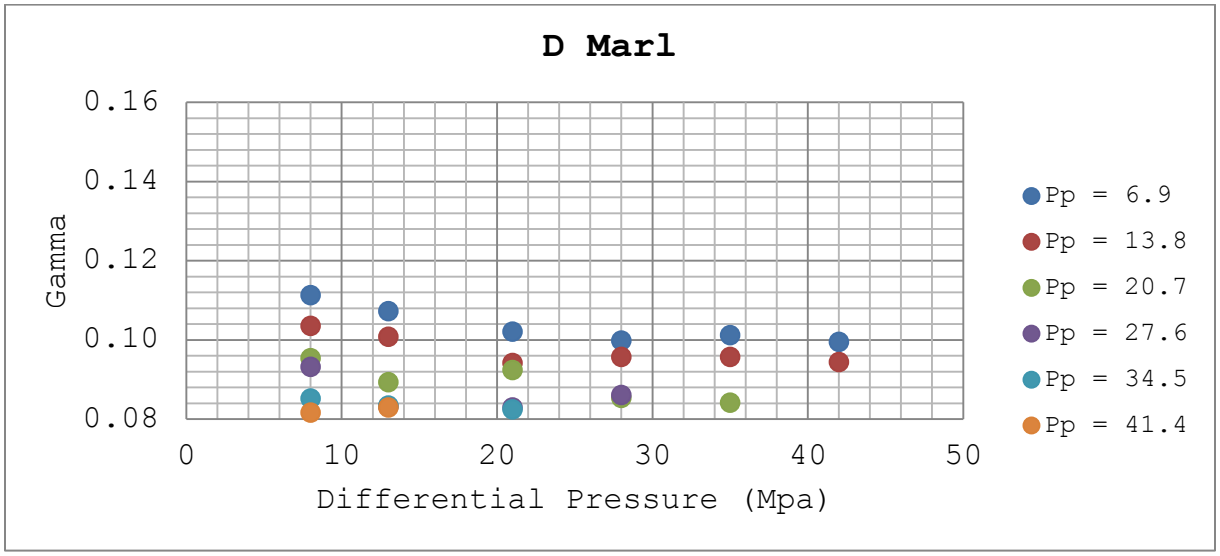

Figure 4.16 Gamma values for the D marl at various pore and confining pressures. Gamma, the S-wave anisotropy, generally decreases with increasing pore and confining pressures, but pore pressure had the greatest effect in this particular experiment.

4.5 Well Log-Derived Thomsen Parameters and the ANNIE approximation

The laboratory-derived relationships discussed in Section 4.4 were used to calculate the VTI and HTI Thomsen parameters for the Smoky Hill member, which are illustrated in Figures 4.19-20. The bulk density (RHOBB), P-wave, and dipole S-wave logs used in the Thomsen parameter calculations are shown in Figure 4.18. Note the velocity sensitivity to pressure and clay content in the log figure.

Anisotropy, both for the VTI and HTI cases in the Smoky Hill member, is weak. The highest δ values were observed for the D units, which have the highest clay content (see GR) and indicate that preferential clay orientation is the primary determinant of the Niobrara's anisotropy. The study interval δ values indicate that the ANNIE approximation is appropriate for use.

Five independent parameters are required to fully characterize a transversely isotropic system: C_{33}, C_{44}, C_{66}, C_{11}, and C_{13}. For vertical wells with flat bedding planes, C_{33} represents the vertically propagating compressional wave, C_{44} is the vertically polarized shear wave, and C_{66} is the horizontally polarized shear wave (Higgins, 2008). Only three out of the five parameters are obtained for vertical wells normal to bedding planes (Higgins, 2008). The ANNIE approximation (Schoenberg and Sayers, 1996) can be used to estimate the remaining two parameters. Schoenberg and Sayers derived the approximation based on seismic observations where Thomsen's δ is very small and generally set to zero. In our study area δ is small, but we use the derived value in the approximation. Setting δ to zero assumes mechanical isotropy and means that the isotropic and anisotropic methods are equal.

The relationship for C_{13} can be written:

$$C_{13} + 2C_{44} - C_{33} = \delta(2C_{33}(C_{33} - C_{44})) \qquad (4.23)$$

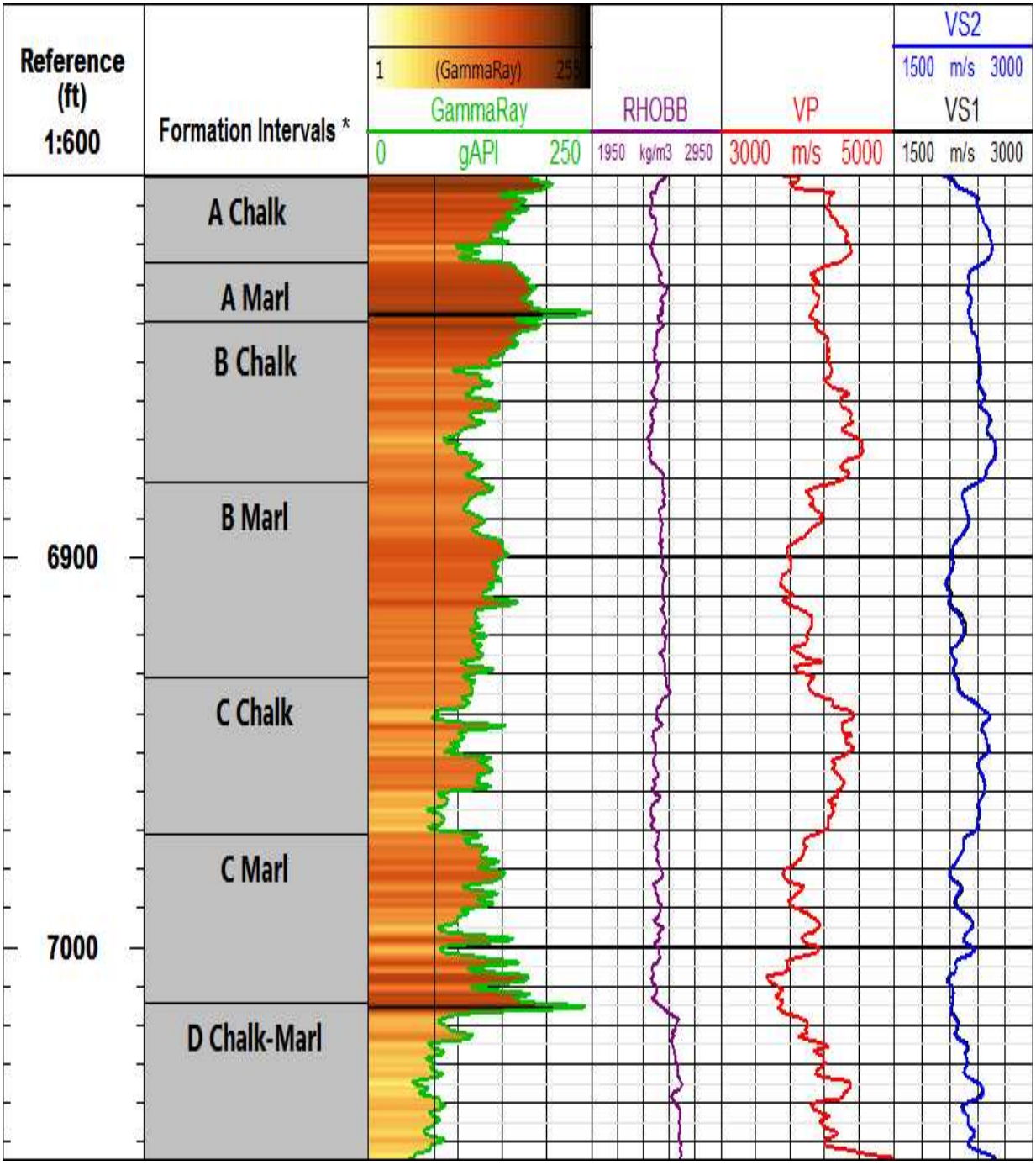

Figure 4.17 Bulk density (RHOBB), VP, VS1, and VS2 logs for the Aristocrat well plotted alongside gamma ray. Note that velocity tends to increase as clay content, illustrated by the gamma ray log, decreases.

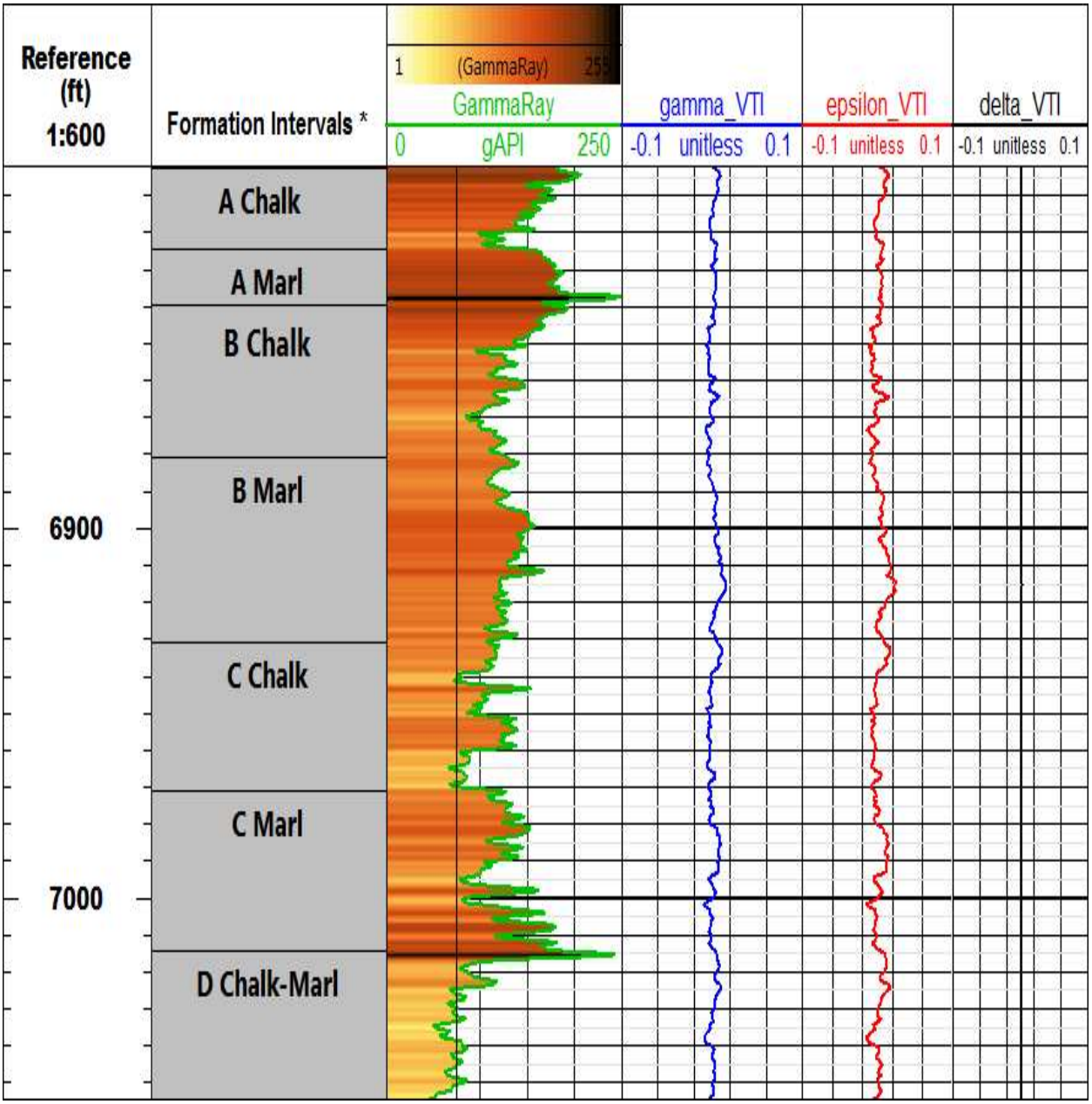

Figure 4.18 VTI Thomsen parameters for Smoky Hill member, Noble Aristocrat well. The Smoky Hill member in this location is isotropic to weakly anisotropic and has little effect on ANNIE approximation-derived stiffnesses.

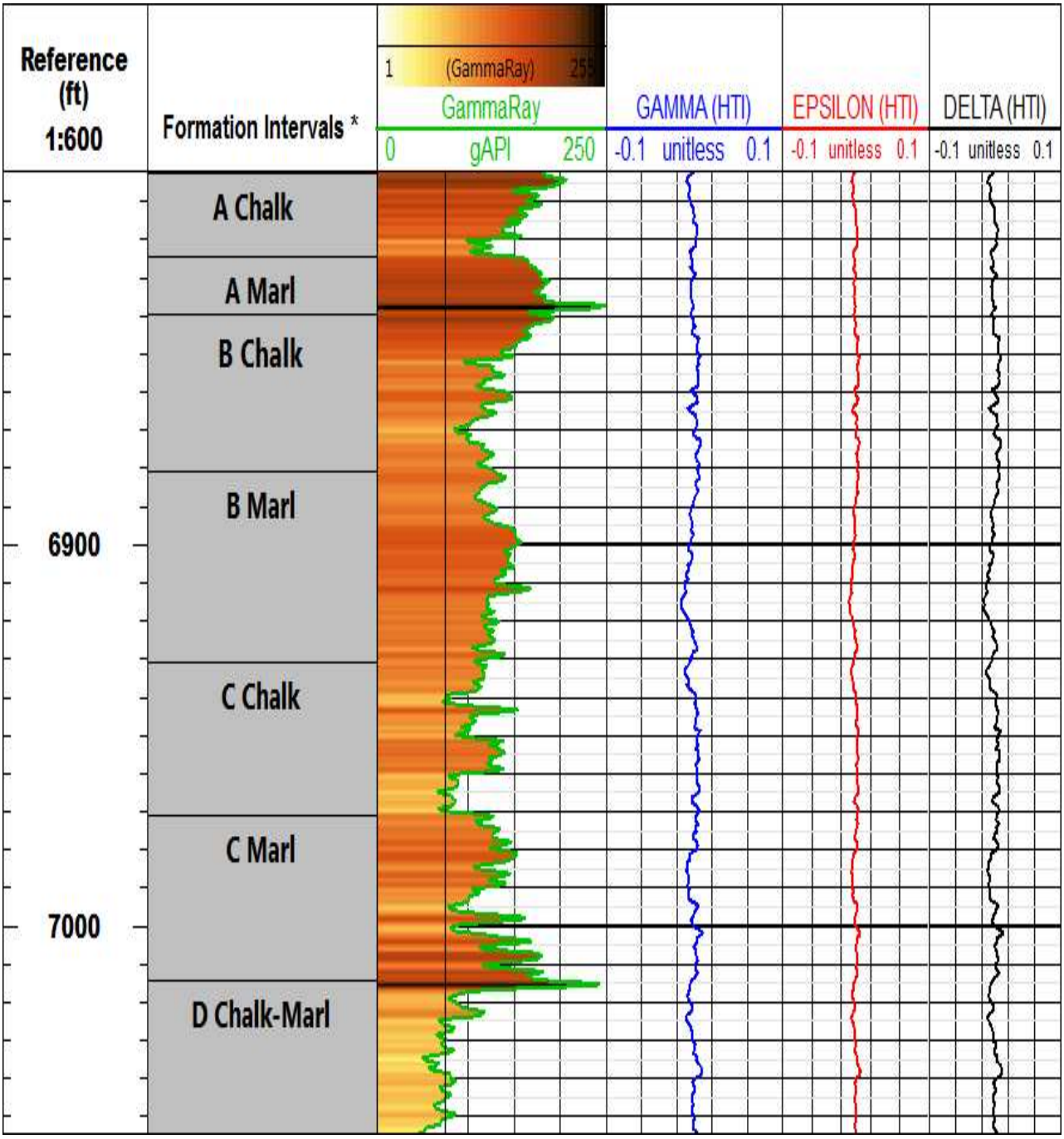

Figure 4.19 HTI Thomsen parameters for the Smoky Hill member, Noble Aristocrat well. The parameters were calculated by using Ruger's (2001) conversion method. HTI anisotropy in this location is weak.

As δ goes to zero the relationship becomes:

$$C_{13} + 2C_{44} - C_{33} = 0 \qquad (4.24)$$

For many shales, C_{13}=C_{12} (Higgins, 2008), therefore:

$$C_{13} = C_{12} = C_{11} - 2C_{66} \qquad (4.25\text{-}28)$$

$$C_{66} = \frac{C_{11} - C_{12}}{2}$$

$$C_{44} = \frac{C_{33} - C_{13}}{2}$$

Combining equations 4.26 and 4.27 yields:

$$C_{66} - C_{44} = \frac{C_{11} - C_{33}}{2}$$

Based on the above derivation, C_{13} and C_{11} can be expressed via relationships to C_{33}, C_{44}, and C_{66}.

Figure 4.20 shows the log data for the ANNIE approximation-derived stiffnesses, and Figures 4.21, 4.22, and 4.23 illustrate the relationships between the compressional and shear stiffnesses and the values of C_{13}, respectively. The VTI compressional and shear stiffness values, shown in Figures 4.21-22, indicate that the Smoky Hill member is isotropic. As expected, the

crossplots show that stiffness generally decreases with increasing clay content, which is indicated by GR.

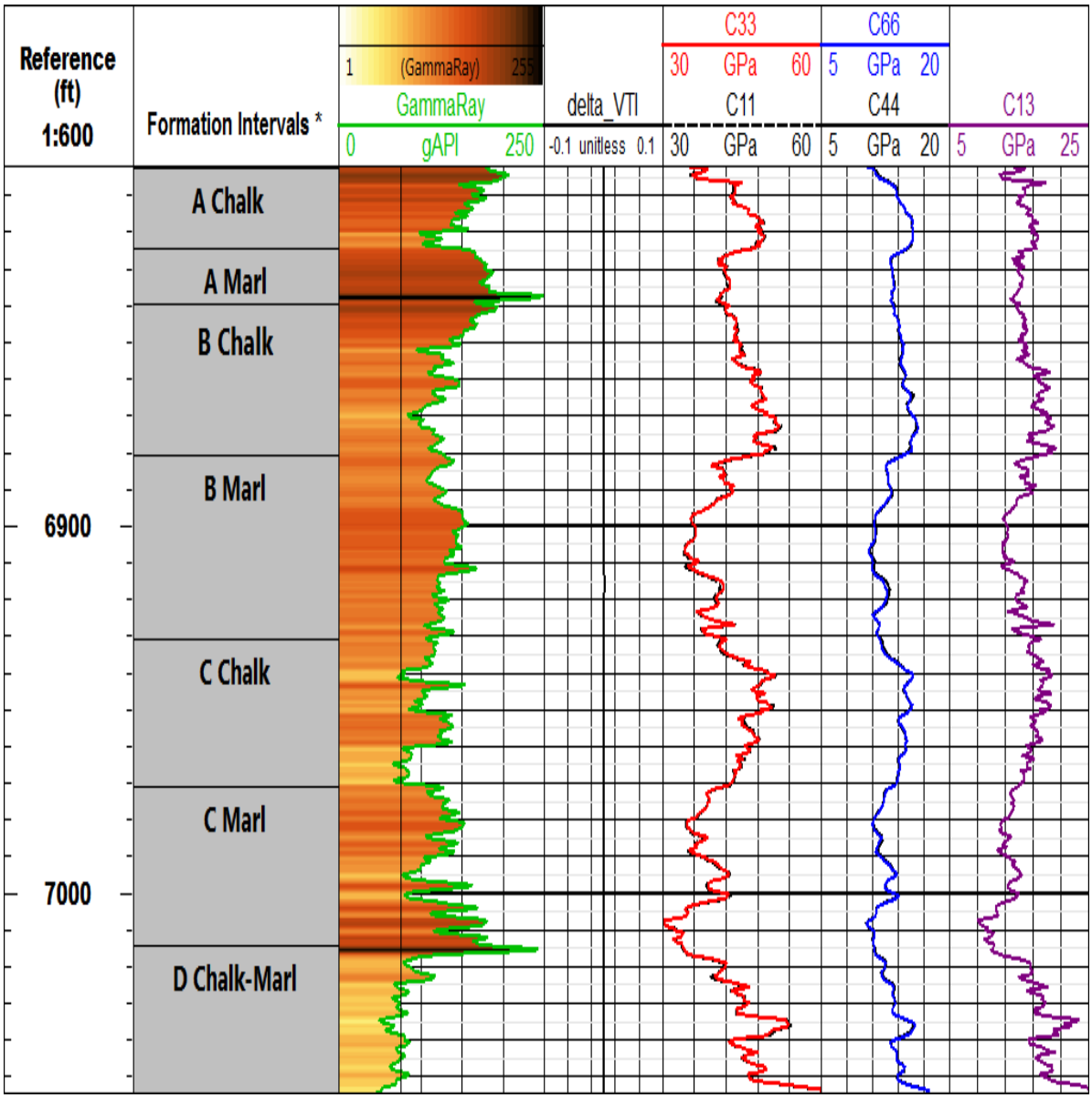

Figure 4.20. Stiffness tensors C_{11}, C_{13}, C_{33}, C_{44}, and C_{66} from the ANNIE approximation. Since δ is equal to zero the value relationships correspond to those of an isotropic medium.

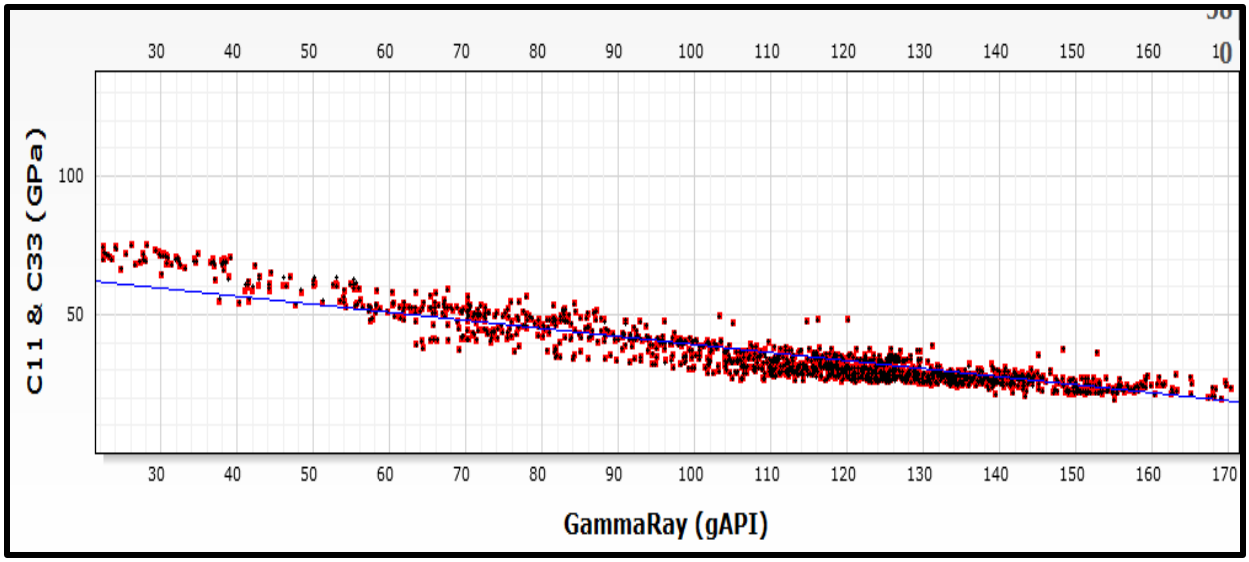

Figure 4.21 C33 and C11 from the ANNIE approximation for the D chalk and D marl. C33 is shown by the black dots, and C11 is shown by red dots. The values of the two stiffnesses equal one another and decrease with increasing clay content.

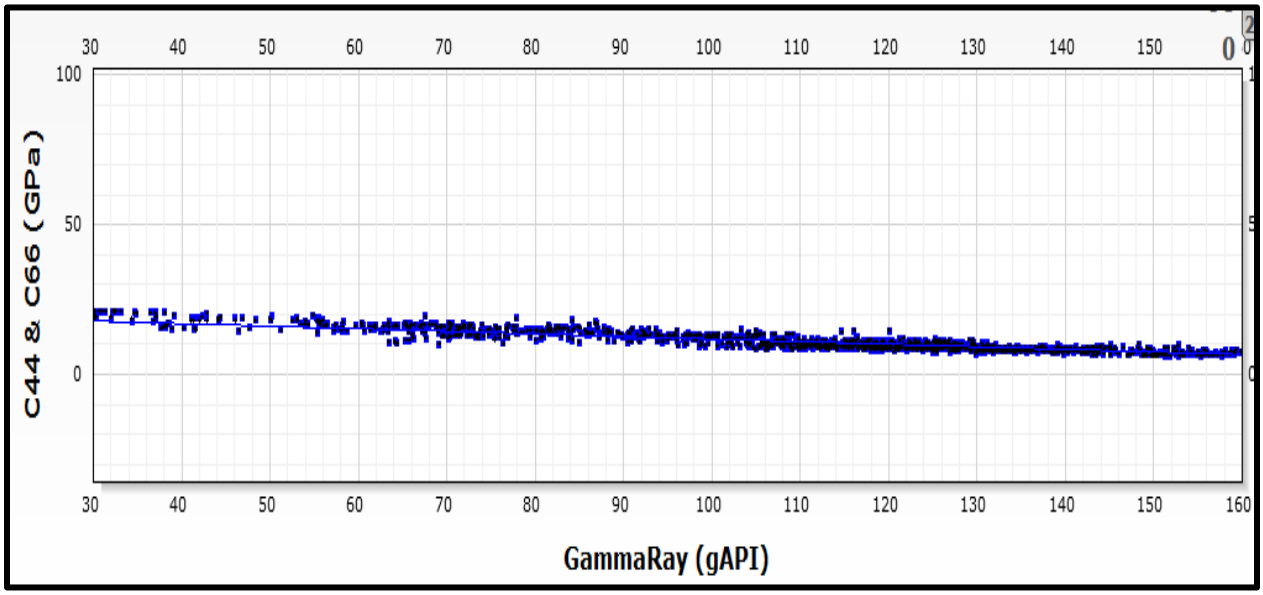

Figure 4.22 C44 and C66 from the ANNIE approximation for the D chalk and D marl. C44 is shown by blue dots, and C66 is shown by black dots. The stiffnesses decrease with increasing clay content and are roughly equal.

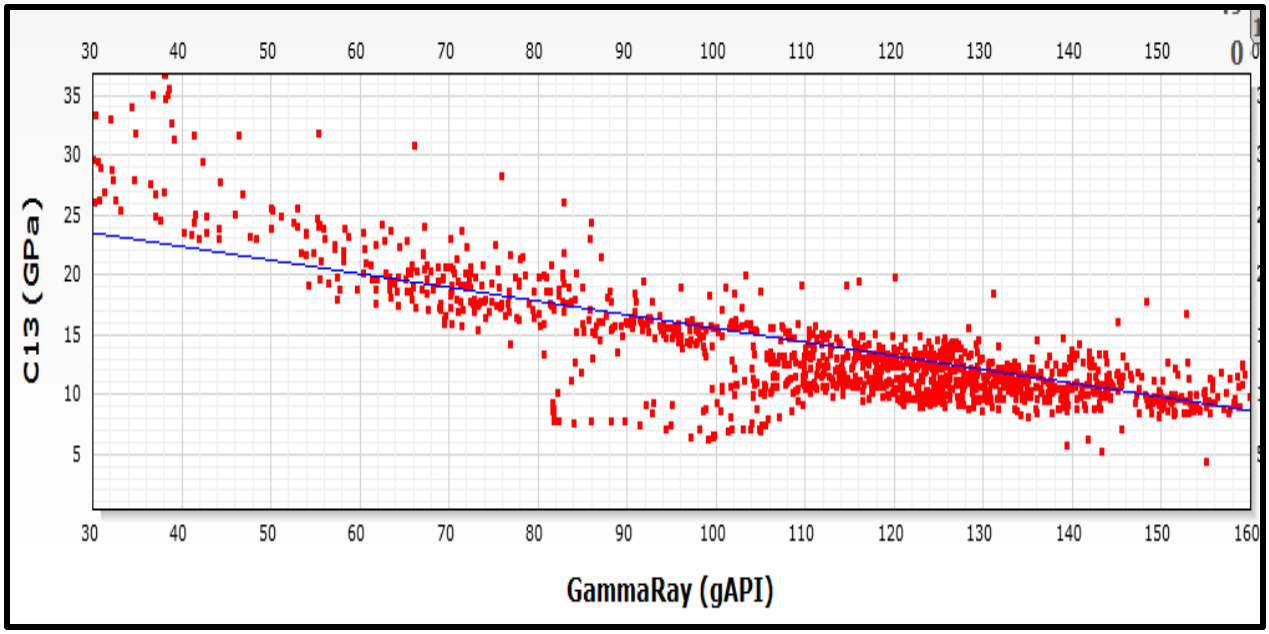

Figure 4.23 C13 from the ANNIE approximation for the D chalk and D marl. C13 decreases with increasing clay content.

σ_h error arising from utilizing Equation 4.28 are illustrated in Figures 4.24 and 4.25, where the anisotropy-induced variation in C_{13} and σ_h are shown. The equation required to measure C_{13} under transverse isotropic conditions is shown by Thomsen (1986):

$$C_{13} = \sqrt{\delta\left(2C_{33}(C_{33} - C_{66})\right) + (C_{33} - C_{66})^2} - C_{66} \qquad (4.27)$$

Underestimating δ can lead to errors when estimating C_{13} and ultimately σ_h, shown by Katahara (2009):

$$\sigma_h = \sigma_v \frac{C_{13}}{C_{33}} \qquad (4.28)$$

Figure 4.25 shows the resultant error arising from δ underestimation. In the extreme case, where δ is 0.5 the corresponding error is 100%. σ_h is the most important parameter under

consideration during completion design and errors of this magnitude could adversely impact completion design.

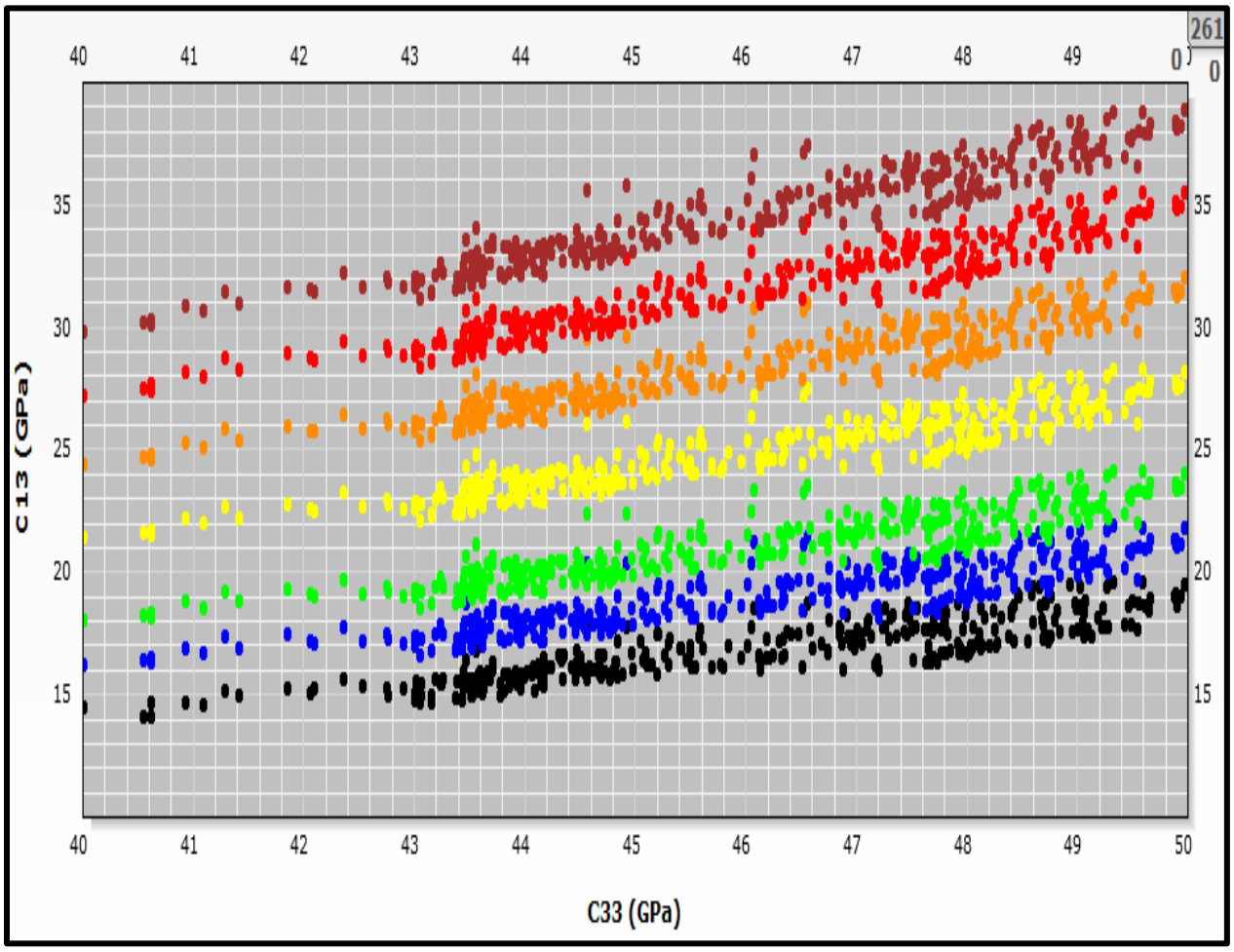

Figure 4.24 C_{13} for various δ assumptions: the black dots represent δ values of 0; the blue dots represent values of 0.05, the green dots represent values of 0.1; the yellow dots represent values of 0.2; the orange dots represent values of 0.3; the red dots represent values of 0.4; and the brown dots represent values of 0.5.

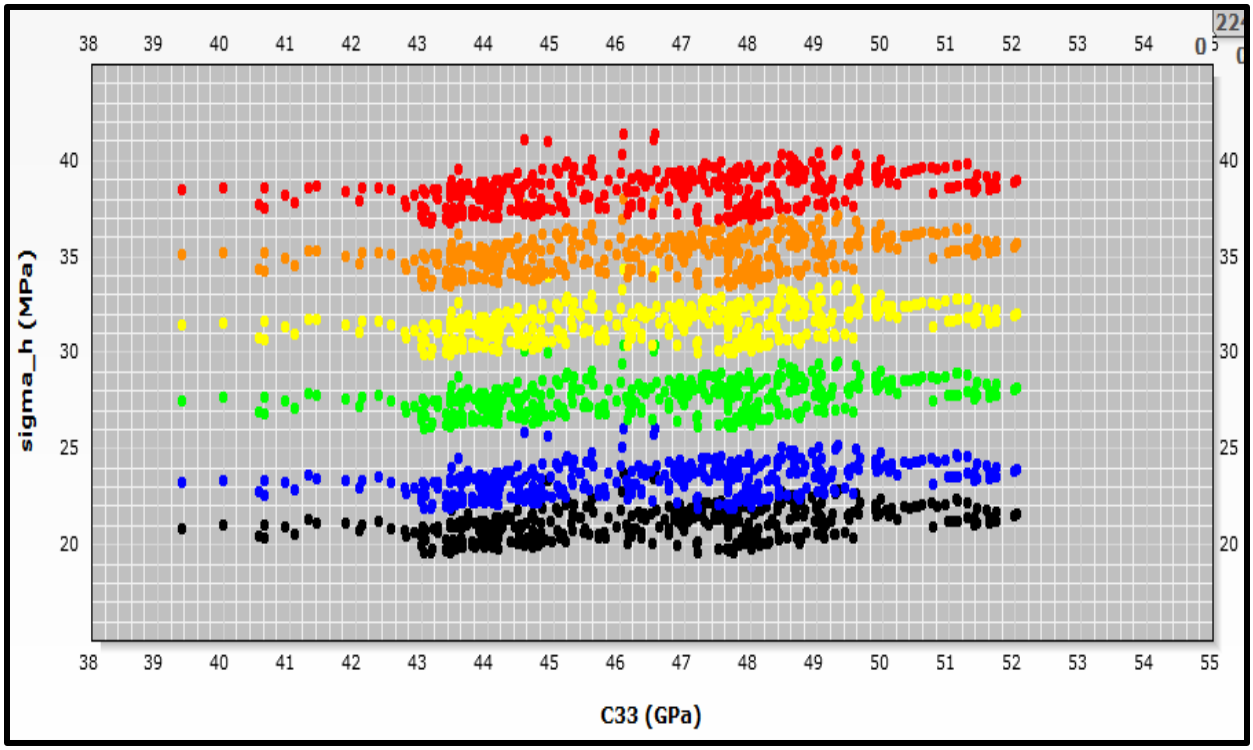

Figure 4.25 σ_h employing various assumptions of δ to calculate C_{13}. For δ, black = 0, blue = 0.1, green = 0.2, yellow = 0.3, orange = 0.4, and red = 0.5. When δ reaches 0.5, assuming zero anisotropy results in roughly 100 % error.

Conclusions

In this chapter we have discussed the wave anisotropy of the Smoky Hill member. We discussed our experimental procedures in Chapter 3 which indicate that we measure phase velocity. The measured Thomsen parameters we measured indicate that the D chalk is isotropic and the D marl is anisotropic. However, anisotropy is controlled by a variety of factors: compliant material content, layering, preferential clay orientation, cracking, and shale compaction and maturity. This means that the Niobrara mechanical properties differ laterally and with increasing depths. Anisotropy also varies with pore pressure. ε and γ decrease with increasing pore and confining pressure.

The ANNIE approximation is viable for use in the study area given the low measured anisotropy in the study well. The well log-derived Thomsen parameter values, most notably δ, were low enough such that the approximation was deemed appropriate for calculating elastic properties that will be discussed further in Chapter 5. The stiffness of the Smoky Hill member decreases with increasing clay content as might be expected. Future work on the Thomsen parameters for the Niobrara will benefit from extracting cores from reservoir depths, instead of using outcrop analogs.

When applying anisotropic methodology to well data, it is important to accurately estimate δ when facilitating data is available. The reported comparatives show that estimating σ_h under false assumptions of δ values leads to large errors.

CHAPTER 5

ELASTIC PARAMETERS AND MINIMUM HORIZONTAL STRESS

5.1 Introduction

This chapter discusses the elastic parameters of the Smoky Hill member as tested in the laboratory and calculated from well log data. Section 5.2 discusses the static elastic parameters and the static elastic anisotropy. Section 5.3 discusses the dynamic elastic parameters, dynamic elastic anisotropy, and the relationship between the static and dynamic parameters. Section 5.4 discusses how the lab and log-derived elastic properties conform to the Voigt, Reuss, and Voigt-Reuss-Hill theoretical boundaries. Section 5.5 calculates the wellbore elastic parameters and minimum horizontal stress. The chapter closes with a discussion of the errors inherent in the different minimum horizontal stress calculation methods and the in-situ variables affecting the measurements.

The elastic parameters E and v are required inputs when designing hydraulic fracture stimulation models. In well log analyses, E and v are used to calculate the minimum horizontal stress, σ_h, a variable required to ensure that the appropriate amount of force is applied during hydraulic fracturing. Understanding the relationship between the static and dynamic elastic parameters is useful to maximize accuracy, and this is achieved through understanding the sedimentary controls affecting the rock mechanical properties (Sone and Zoback, 2013). The Smoky Hill member, deposited in a shallow-sea environment, consists of different depositional sequences that often result in intrareservoir lithological heterogeneities (Pollastro, 1992; Passey et al., 2010; Sonnenberg, 2011). This means that clay content, which correlates with lower Young's modulus and higher Poisson's ratio values, may vary between wells.

Other factors determinant in the mechanical nature of the rock fabric include, but are not limited to: the distribution of platy clay minerals (Hornby et al., 1994; Sone and Zoback, 2013); the presence of organic materials in shale (Vernik and Nur, 1992; Vernik and Liu, 1997; Havens, 2011; Sone and Zoback, 2013); the maturity of shales (Sone and Zoback, 2013); and the number of tectonic loading and unloading cycles (Sone and Zoback, 2013). The distribution of platy clay minerals and organic materials determines the elastic anisotropy of reservoir rocks, while kerogen maturity and orientation are variables that determine both the stiffness and mechanical anisotropy of shales (Vernik and Nur, 1992). Previous loading and unloading sequences also affect the elastic properties of rocks. Vertical stylolites and horizontal filled fractures have been observed at the quarry outcrop. These relate to previous stress regimes and indicate that the Niobrara has undergone a horizontal loading and unloading phase within the study area, and that calculating horizontal stresses assuming uniaxial strains may lead to errors (Katahara, 2009).

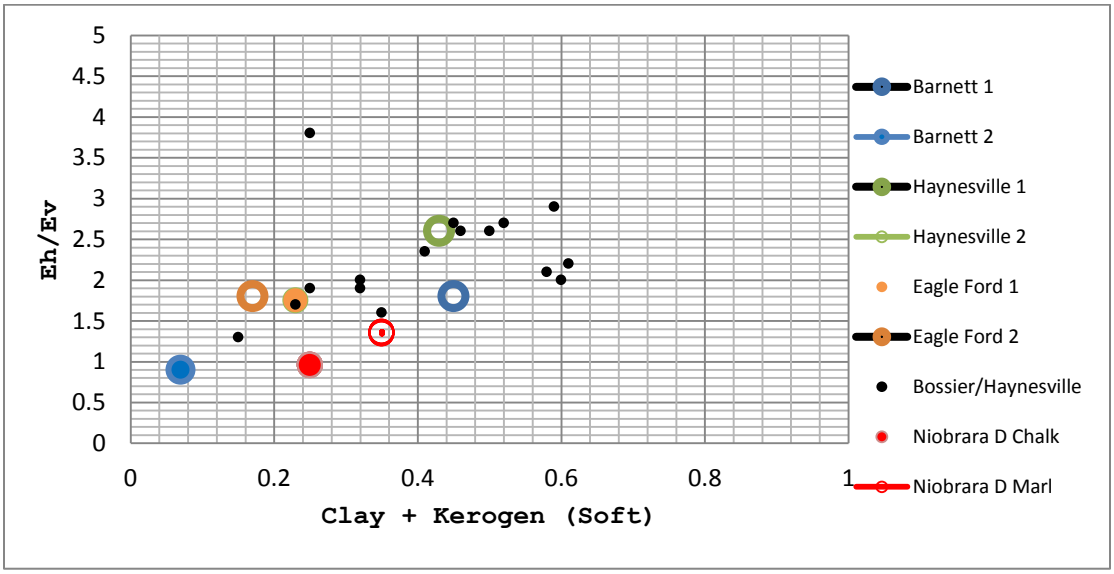

Figure 5.1. Elastic anisotropy, shown by the E_h:E_v ratio, plotted over Clay + Kerogen content. Elastic anisotropy increases as the presence of soft materials increases. The values for the D chalk and D marl are plotted with solid red circles and red rings, respectively. Data other than the Niobrara samples come from Sone and Zoback (2013).

Figure 5.1 shows the relationship between elastic anisotropy and clay and kerogen content. The chart shows that as clay and kerogen increase the amount of elastic anisotropy increases. Since clay is more compliant than calcite and quartz and consists of platy grains, the presence of clay particles increases the directional stiffness of rock materials. Clay matter, when preferentially oriented, is more compliant in the direction normal to bedding but stiffer parallel to bedding. Kerogen, when preferentially oriented has similar effects, with the magnitude of those effects highly dependent on kerogen maturity (Vernik and Nur, 1992).

Calculation of σ_h can be achieved for the isotropic and anisotropic cases, and for purposes of this study quantifying anisotropy is therefore important. Observing the E_h:E_v values for the D chalk and D marl (Figure 5.4) one finds that the chalk sections are elastically isotropic. However, the observed elastic anisotropy present in the marl sections is substantial enough to pose problems when calculating $\sigma_{h,}$ and in the Niobrara the marl sections should serve as fracture barriers, thus making accurate determination of σ_h critical.

5.2 Static Elastic Parameters

The static elastic parameters were obtained from the uniaxial stress versus strain measurements. The D Chalk samples measured were massive, exhibited no laminations, and had no observed cracks. Young's moduli for both facies are plotted in Figure 5.2. *E* values decrease with increasing clay content. The *E* values of the D Chalk increase with increasing axial pressure up to 20 MPa, and thereafter the measurements are constant, ranging between 26.0-28.0 GPa. 20 MPa was interpreted as the pressure where compaction was terminal. The *E* values of the D marl are more variable with respect to bedding angle, and it is quite obvious that the D marl is

anisotropic at lower confining pressures. At 8 MPa, *E* values range between 15.0-20.0 GPa, and at 42 MPa *E* values range between 18.0-20.0 GPa, bedding angle dependent. The higher concentration of low aspect ratio, platy minerals present in the marl samples has a great effect on the elastic behavior. When pressure is applied parallel to bedding angle, *E* ranges between 19.6-20.1 GPa for axial pressure values ranging between 8.0-42.0 MPa. However, the ranges of *E* for the vertical and 45-degree samples range between 15.0-18.0 GPa and 17.0-19.0 GPa for the same axial pressure range, respectively. This means that the clay minerals and organic content relax, and undergo further mechanical compaction in the vertical direction, but as bedding angle increases the clay materials are stiffer. Ergo, the material becomes less compliant.

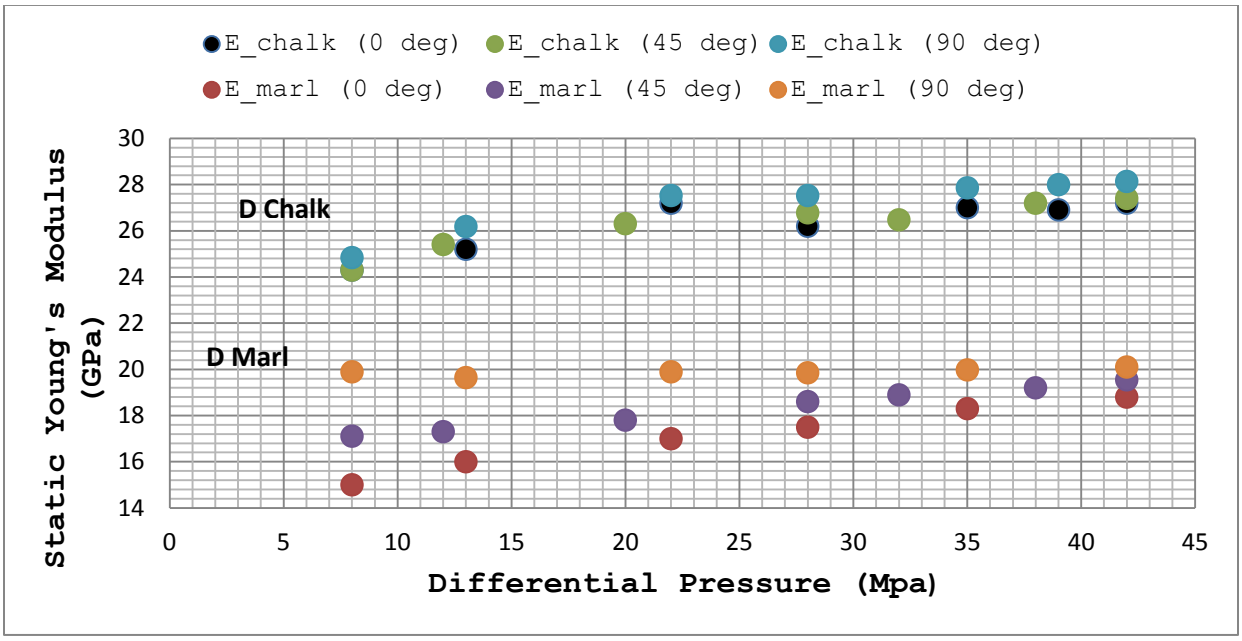

Figure 5.2. Laboratory-derived static Young's modulus for the D chalk and D marl facies. The D chalk is isotropic, and the D marl is anisotropic, with the values converging at high pressures. The compliance of the clay minerals in the D marl explains the change in static *E* values with pressure.

The Poisson's ratio values are plotted in Figure 5.3. The chalk is weakly anisotropic at low confining pressures and isotropic at 42 MPa, with values ranging between 0.2-0.24. *v* is curiously lower for the marl samples, and similar results were obtained by Maldonado (2011). This result was interpreted primarily as a function of pore topology where platy clay minerals filled the larger pore spaces, thus resulting in a stiffer matrix (Revil, 2013). For the D marl samples, the vertical and 45-degree samples range between 0.10-0.15 and 0.11-0.16, respectively, between axial pressures ranging between 8-42 MPa. The increasing stiffness with respect to bedding angle is again observed as the horizontal *v* values range between 0.15-0.17 throughout the experiment.

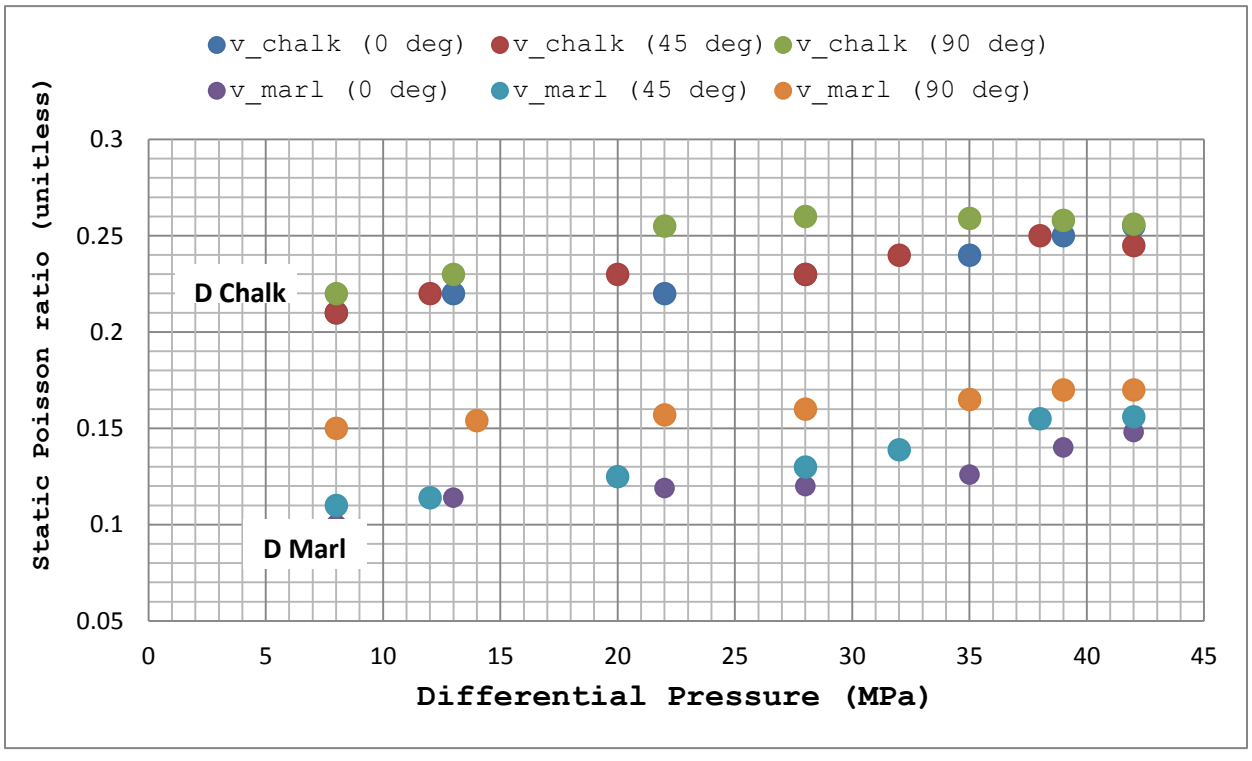

Figure 5.3. Static Poisson's ratio for the D Chalk and D Marl facies.

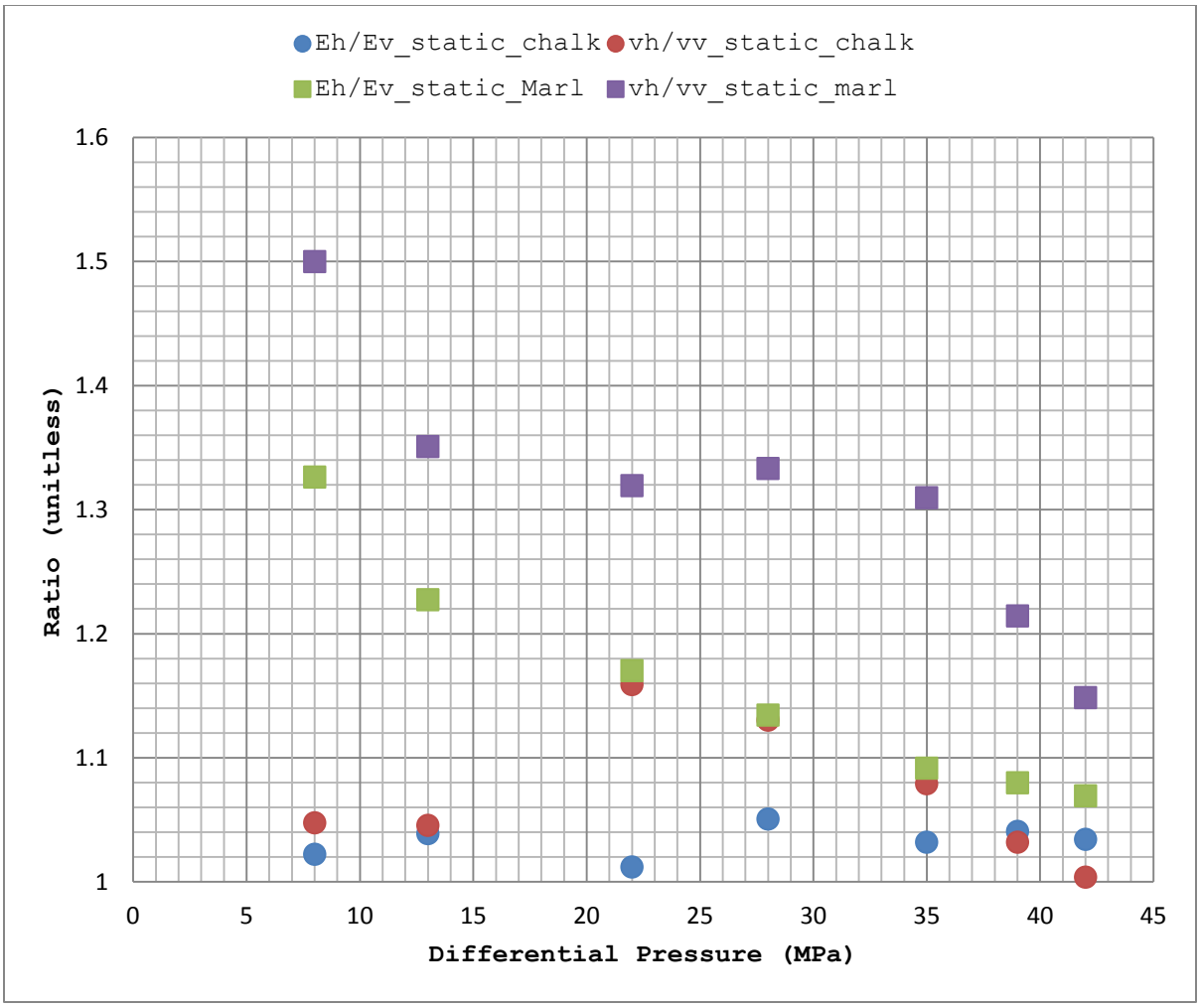

Figure 5.4. Ratios between vertical and horizontal Young's moduli and Poisson ratios for the D chalk and D marl facies. The D chalk is isotropic and the D marl becomes less anisotropic with increasing pressure.

The average E_h:E_v for the D chalk (Figure 5.4) was found to be 1.03, low enough such that the D Chalk might be considered elastically isotropic. Alqahtani et al. (2013) showed that E_h:E_v for the Mancos shale is 1.06. The v_h:v_v average for the D chalk is 1.07. The values obtained for this ratio contains outliers that are plotted between 22-28 MPa, increasing the elastic parameter derived anisotropy considerably. These values might be the result of experimental error caused by pump malfunction during measurement. By removing the outlying values the

average E_h:E_v and ν_h:ν_v values become 1.03 and 1.04, respectively. Based on the elastic anisotropy parameter ratios the D chalk is isotropic.

The E_h:E_v and ν_h:ν_v averages for the D marl are 1.2 and 1.3, respectively. These averages are misleading due to the drastic decrease in elastic anisotropy with increasing pressure. At 8 MPa, E_h:E_v and ν_h:ν_v are 1.32 and 1.50, respectively, and these values decrease to 1.07 and 1.14, respectively, as axial pressure approaches 42 MPa. These changes in elastic anisotropy are attributed to creep observed in the vertical samples, and again the interpretation is that the clay layers become compressed with increasing pressure and decrease the effects of preferential clay orientation.

5.3 Dynamic Elastic Parameters

The ultrasonic velocities measured during the Thick-Walled Cylinder testing were used to calculate dynamic elastic parameters (Figures 5.5-6). Velocities were acquired at confining pressures ranging between 4.5-45 MPa for the D Chalk and D Marl on samples cored 0, 45, and 90 degrees to bedding. The elastic parameter values for the D Chalk and the D Marl were calculated using the anisotropic version of Hooke's Law discussed in Chapter 3.

The *E* values measured for the D Chalk measured approximately 36.7-38 GPa for the vertical samples and 34.0-35.1 for the horizontal samples. The observed low pressure sensitivity is a function of measuring dry rock properties under confining pressure, unlike the static experiments where differential pressure was applied. The low pressure sensitivity observed is also largely attributable to measuring immature shale samples, which have lower velocity response to increased pressures (Vernik et al., 2010). Poisson's ratio values follow a similar trend, and increase from 0.22-0.24 for the vertical samples, and range 0.27-0.28 for the horizontal samples. The E_h:E_v values for the chalk were 0.94 throughout the experiment. Future

work should include measuring the static properties with displacement transducers, an experimental method less susceptible to strain gauge failure (Sone and Zoback, 2013). Measuring the dynamic and static properties separately allowed for more static measurements to be taken by circumventing strain gauge failure in the Thick-Walled Cylinder (Maldonado, 2010; Havens, 2011).

The marl samples also exhibited low pressure sensitivity in the Thick-Walled Cylinder. E_{horz} ranged between 42.8-44.0 GPa throughout the experiment, and E_{vert} ranged between 31.4-32.6 GPa. ν values for the D Marl are 0.34 for ν_{horz}, and the values range between 0.30-0.32 for ν_{vert}. Again it was observed that the D marl is more compliant in the vertical direction than the horizontal direction. E_h:E_v values measured 1.36 at 5 MPa confining pressure, and decreased slightly to 1.35 (Figure 5.7).

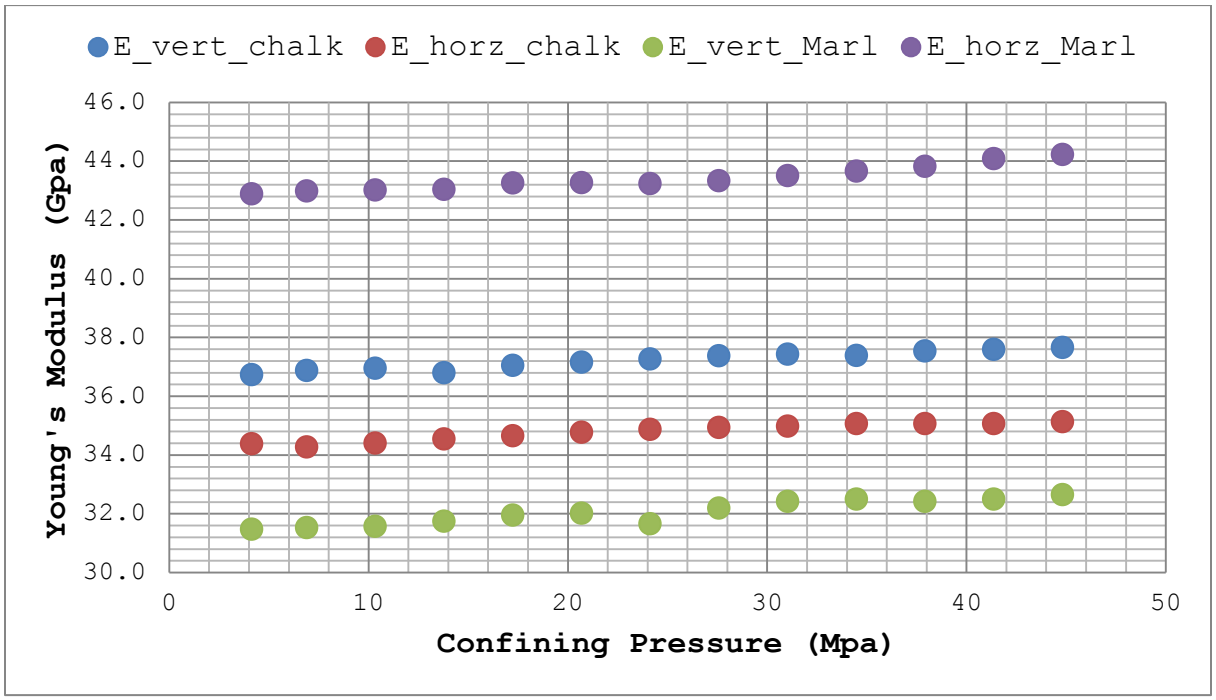

Figure 5.5. Dynamic Young's modulus values for the D Chalk and D Marl.

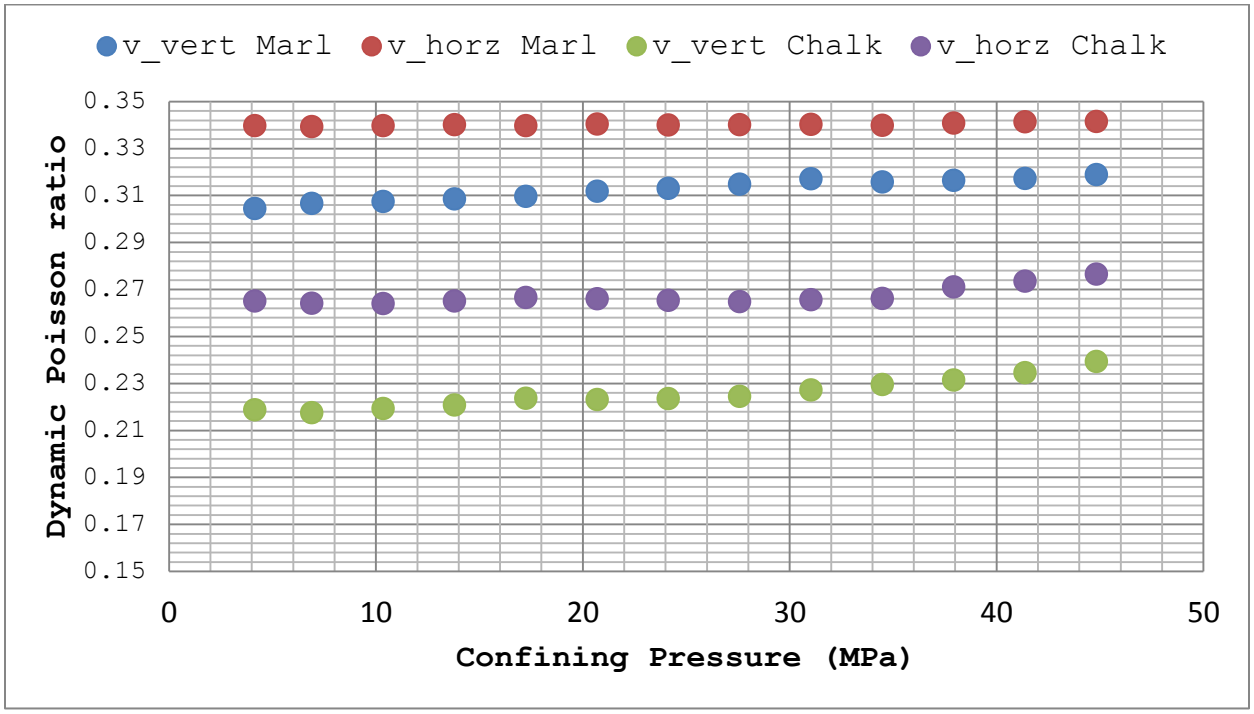

Figure 5.6. Dynamic Poisson's ratio values for the D chalk and D marl.

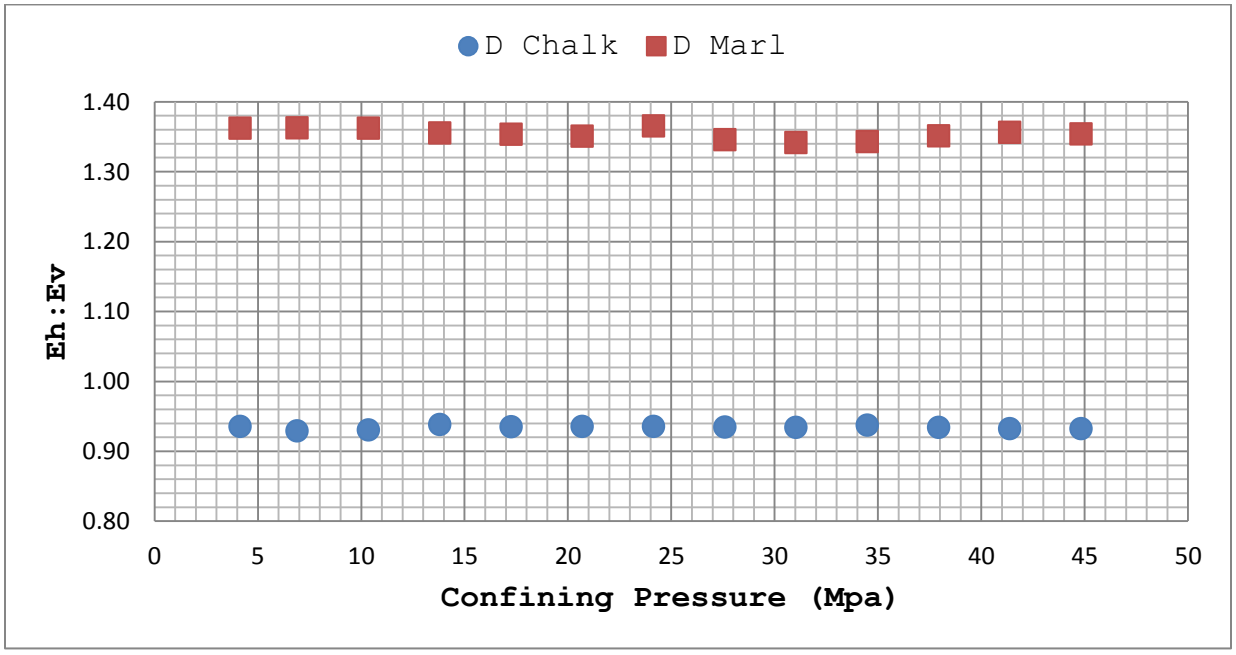

Figure 5.7. Dynamic Eh:Ev for the D Chalk and D Marl.

The lab-derived constants were compared to Voigt, Reuss, and Voigt-Reuss-Hill boundaries to better understand variability and check the lab measurement accuracy. The boundaries were constructed by considering the facies as simple aggregates of "soft" and "stiff" components primarily composed of calcite, quartz, and clay. The mineralogy of the components used to construct the Voigt, Reuss, and Hill boundaries along with the Young's modulus of the various mineral constituents is shown in Figure 5.10. The laboratory dynamic constants fit the theoretical model and fall between the Reuss and Hill boundaries. The static Young's modulus data falls lower than predicted and this is attributable to differences in the dynamic and static properties of the clay components. The large strains exerted on the porous soft components during the static testing results in more deformation during large-strain static loading, and this makes the soft aggregate appear more compliant (Sone and Zoback, 2013). Sone and Zoback (2013) showed that by lowering the modulus of the soft components, boundaries can be shifted to accommodate the lower soft-component moduli measured in laboratory static testing. This was accomplished by lowering the soft-component modulus by half. However, the primary purpose of static testing in these experiments is to acquire static measurements to correct the dynamic values measured during borehole logging, and the theoretical boundaries bear minimal importance outside of general quality control measures.

The acquisition of the dynamic and static elastic parameters permits the calculation of a correction ratio. Since the dynamic elastic parameters are higher than static elastic parameters in rocks it is useful to correct them to the static values if data is available. This presumably reduces error when calculating σ_h. I selected 42 MPa, the highest pressure measurement, to serve as the standard case for reservoir pressure and selected the corresponding values for E_{dyn}, E_{stat}, ν_{dyn}, and $\nu_{stat.}$ These values were used to compute ratios that enable the correction of the log-derived

Table 5.1. Mineral composition of soft and stiff components and their *E* values

Mineral	Calcite	Mg Calcite	Dolomite	Quartz	Plagioclase	Pyrite	Anhydrite	Kaolinite	Illite-Smectite	Stiff (%)	Soft (%)
E (GPa)	84	84	117	95	70	305	72	6	3	N/A	N/A
D Chalk (%)	48	0.4	0.6	16	5	0.9	0.6	2	22	75	25
D Marl (%)	37	1	1	14	6	4	0.8	3	32	65	35

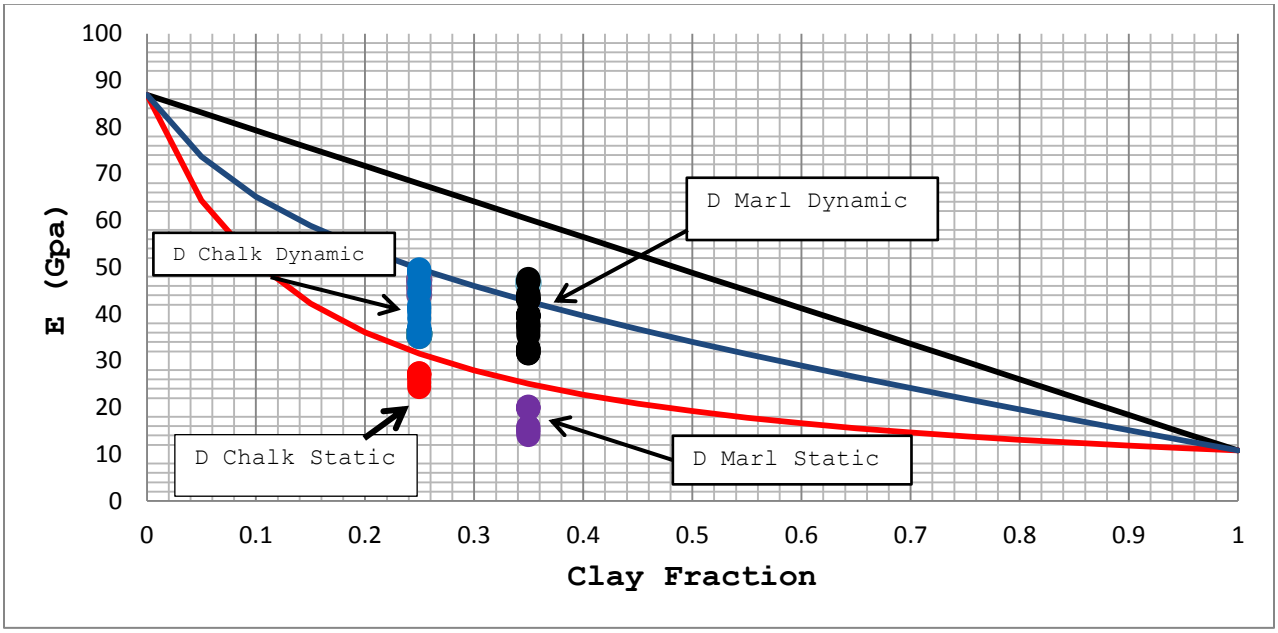

Figure 5.8. Voigt, Reuss, and Voigt-Reuss-Hill theoretical constraints for the Niobrara formation Young's modulus. The dynamic values for the Young's modulus fall between the Reuss and Hill average values, but the static values fall outside of the theoretical constraints.

elastic parameter values. The assumption behind this method is that the static elastic parameters *E* and *v* are the "true" values and that the dynamic parameters should be corrected to be representative of the true medium elasticity. Also assumed is that there is minimal model error such that the relationships derived in the lab, where ultrasonic frequencies (MHz) are measured,

are able to be employed to correct the borehole sonic measurements, where lower frequencies (KHz) are measured. Therefore the grand assumption is that the resultant parameters facilitate more accurate calculation of σ_h, and enables methodological comparisons between values derived via isotropic and anisotropic dynamic assumption. The ratios employed are shown in Table 5.2.

Table 5.2. Dyn:Stat for D Chalk and D Marl; P_{axial} = 42 MPa

Sample	E_{dyn} (GPa)	E_{stat} (GPa)	v_{dyn}	v_{stat}	$E_{dyn:stat}$	$v_{dyn:stat}$
D Chalk (vert)	35.0	27.0	0.275	0.165	1.30	1.67
D Chalk (horz)	33.0	28.0	0.24	0.17	1.18	1.41
D Marl (vert)	37.8	19.0	0.34	0.248	1.99	1.37
D Marl (horz)	44.0	20.0	0.32	0.25	2.20	1.28

5.4 Well log-derived elastic parameters and minimum horizontal stress

The elastic constants were calculated for the Noble Aristocrat well. The stiffness coefficients required for the engineering calculations were derived using the ANNIE approximation (Schoenberg and Sayers, 1996), which was shown in Chapter 4. *E* and *v* values were calculated for the dynamic anisotropic case, and the laboratory-derived static-to-dynamic correction ratios were applied. To check the relationship between the laboratory-derived and log-derived elastic constants I fitted the lab data to the log by using P-wave velocities. The lab-derived elastic parameter values are lower than the log-derived values, most likely a function of higher clay content in the laboratory test samples which have clay content measuring 5-7% higher than the various chalk and marl intervals analyzed in the well. The laboratory

measurements enabled application of a dynamic-to-static correction. The static values for the Young's modulus were generally 20 % lower than the dynamic values while the static Poisson's ratio was only 4% lower.

The lack of elastic anisotropy means that error in the calculation of σ_h, arising from using dynamic rather than static parameters may be minimized by using the uniaxial strain approximation, an approach which is implemented due to the lack of strain data.

Minimum horizontal stress is the salient parameter to estimate when designing a hydrofracture model, for it determines the force that must be applied to open fractures. The inputs required to calculate minimum horizontal stress are E, ν, σ_v, Biot's coefficient α, and pore pressure, σ_{PP}. For this study I calculate the minimum horizontal stress assuming uniaxial strain, which assumes that σ_v is the only force acting on the system. Katahara (2009) discusses the drawbacks in these assumptions, and Karig and Hou (1992) have shown that lateral strain energy builds up during laboratory experiments where samples are subjected to uniaxial strain. The tectonic history of the Niobrara might have resulted in significant non-elastic deformation that causes the calculations to underestimate σ_h, and lack of available strain introduces some uncertainty.

At this point we have calculated the Young's moduli and Poisson's ratios for the D chalk and D marl facies. We have obtained the ratios between the dynamic and static measurements and calculated a correction factor to apply to the well log. The well log for the Noble Aristocrat well in Wattenberg Field, CO was chosen for this study. The log contains density and dipole sonic, so the isotropic and anisotropic cases of σ_h can be found (Higgins et al., 2008).

To calculate the minimum horizontal stress I used the following equations from Higgins et al. (2008):

$$\sigma_h - \alpha\sigma_{pp} = \frac{v}{1-v}\left(\sigma_v - \alpha\sigma_{pp}\right) + \frac{E}{1-v^2}\varepsilon_h + \frac{Ev}{1-v^2}\varepsilon_H \qquad (5.1)$$

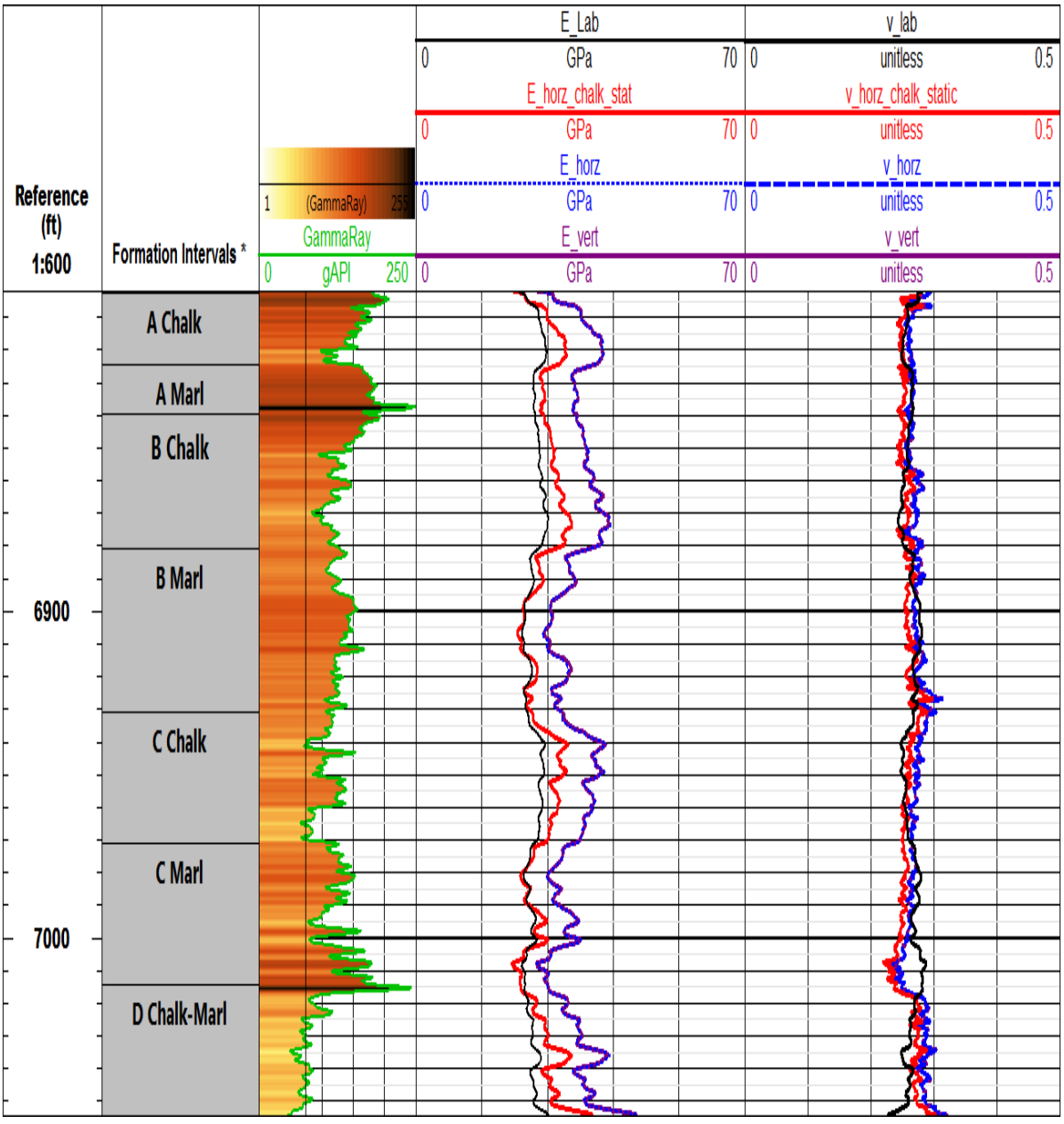

Figure 5.9 Elastic parameters E and v for the Smoky Hill member, Aristocrat well, Wattenberg Field. The log-derived elastic parameters are greater than those measured for the lab due to higher clay content in the lab samples. The static-corrected elastic parameters enable greater accuracy in the prediction of σ_h.

$$\sigma_h - \alpha\sigma_{pp} = \frac{E_{horz}}{E_{vert}}\frac{v_{vert}}{1-v_{horz}}\left(\sigma_v - \alpha\sigma_{pp}\right) + \frac{E_{horz}}{1-v_{horz}^2}\varepsilon_h + \frac{E_{horz}v_{horz}}{1-v_{horz}^2}\varepsilon_h \qquad (5.2)$$

Assuming uniaxial strain we now have:

$$\sigma_h - \alpha\sigma_{pp} = \frac{v}{1-v}\left(\sigma_v - \alpha\sigma_{pp}\right) \qquad (5.3)$$

,and

$$\sigma_h - \alpha\sigma_{pp} = \frac{E_{horz}}{E_{vert}}\frac{v_{vert}}{1-v_{horz}}\left(\sigma_v - \alpha\sigma_{pp}\right) \qquad (5.4)$$

Minimum horizontal stress was calculated for four cases: dynamic isotropic, dynamic anisotropic, static isotropic, and static anisotropic. The static case assumes that the corrective ratio acquired in the lab is appropriate for application to the chalk and marl in Wattenberg Field. Figure 5.14 shows σ_h, calculated for the various cases, plotted alongside gamma ray, *DPHI* and *NPHI*, σ_v, σ_{PP}, *UCS*, which represents uniaxial compressive stress, and *PFRAC*, or fracture pressure. The *PFRAC* and *UCS* logs were calculated by Halliburton and provided with the log suite. There is negligible difference between the dynamic isotropic and anisotropic assumptions. However, percent error between the dynamic and static cases ranges between *5-15 %*, depending on the model used (Figure 5.14).

Figures 5.11, 5.12, and 5.13 show the respective error for each method. To calculate the percent error in each method I used two separate equations. The first concerns the percent error between the two dynamic cases:

$$Percent\ error = \left|\frac{\sigma_{h_{dyn_{anisotropic}}} - \sigma_{h_{dyn_{isotropic}}}}{\sigma_{h_{dyn_{anisotropic}}}}\right| x\ 100 \qquad (5.5)$$

The second equation calculates the percent difference between the dynamic cases and the corresponding static case:

$$Percent\ error = \left| \frac{\sigma_{h_{static}} - \sigma_{h_{dynamic}}}{\sigma_{h_{static}}} \right| x\ 100 \qquad (5.6)$$

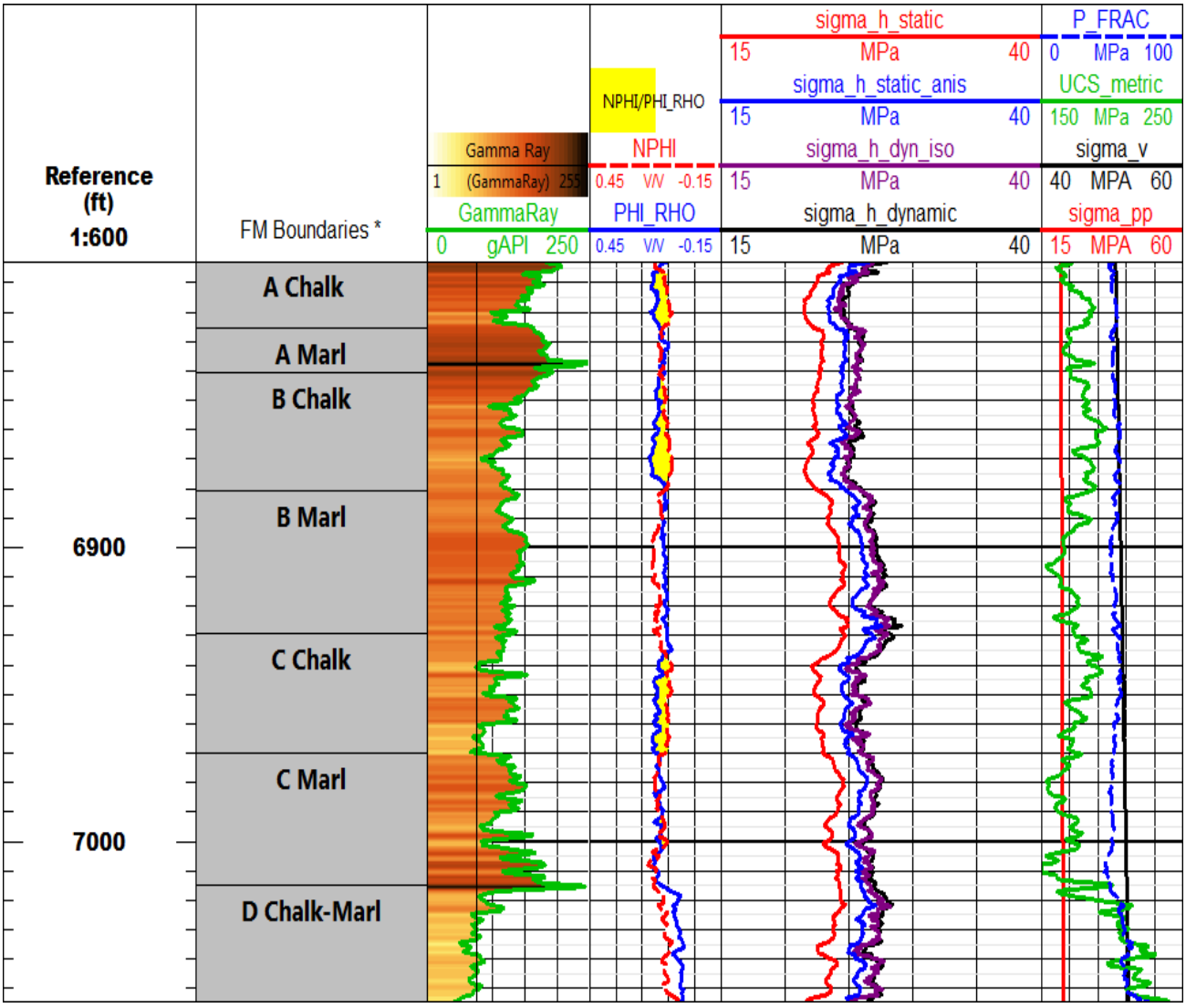

Figure 5.10. Minimum horizontal stress calculated for the dynamic isotropic, dynamic anisotropic, static isotropic, and dynamic anisotropic cases. The difference between the static and dynamic isotropic cases is roughly 15 %, while the anisotropic static and dynamic cases differ by only 5 %. The horizontal stress curves are plotted alongside gamma ray, density porosity, neutron porosity, pore pressure, fracture pressure, uniaxial compressive stress, and overburden stress.

To illustrate the effects of improper assumptions I selected the zones that show DPHI:NPHI crossover in Figure 5.14. After calculating the percent error for the apparent reservoir intervals, I plotted the error values over σ_h. The plots are shown in Figures 5.15-5.17.

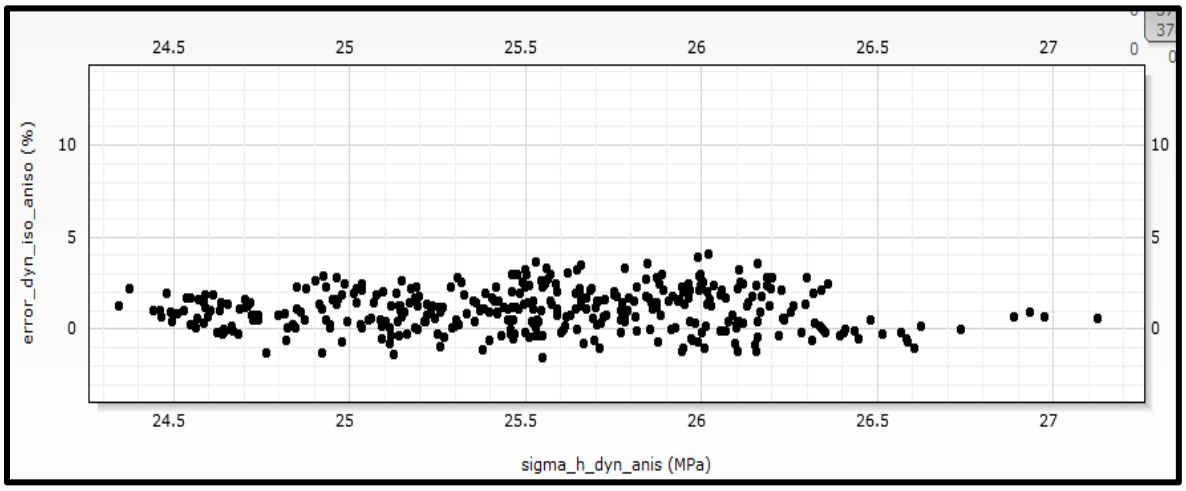

Figure 5.11 Percent error between dynamic isotropic and dynamic anisotropic calculations of σ_h for the selected reservoir intervals. Error values generally range between -2.0 and 3.0 percent.

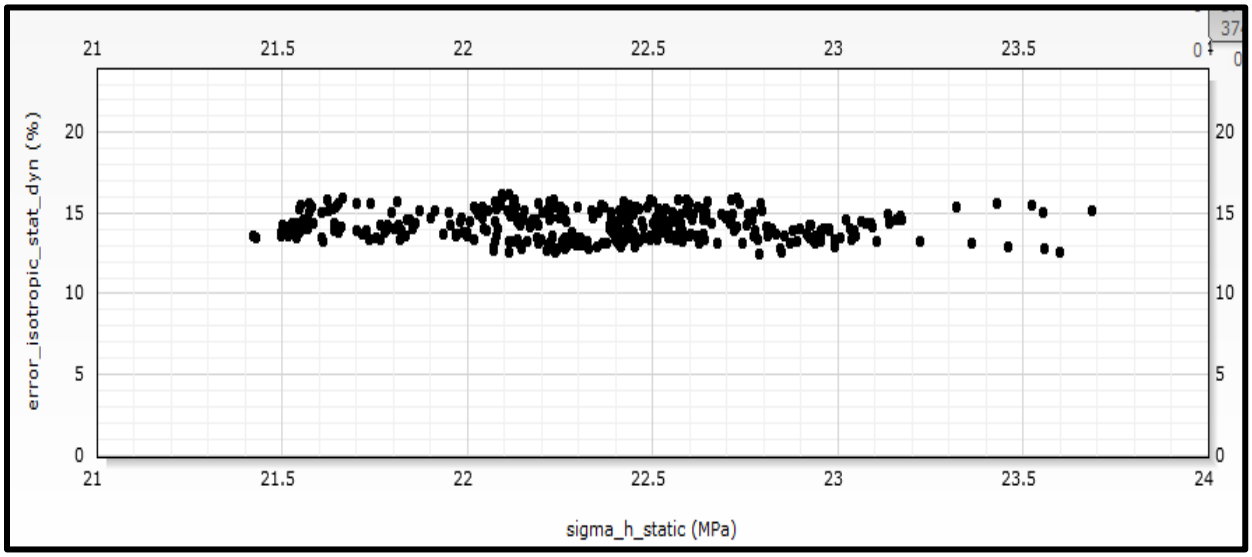

Figure 5.12 Percent error between dynamic isotropic and static isotropic calculations of σ_h for the selected reservoir intervals. Percent error generally ranges between 12-16 percent.

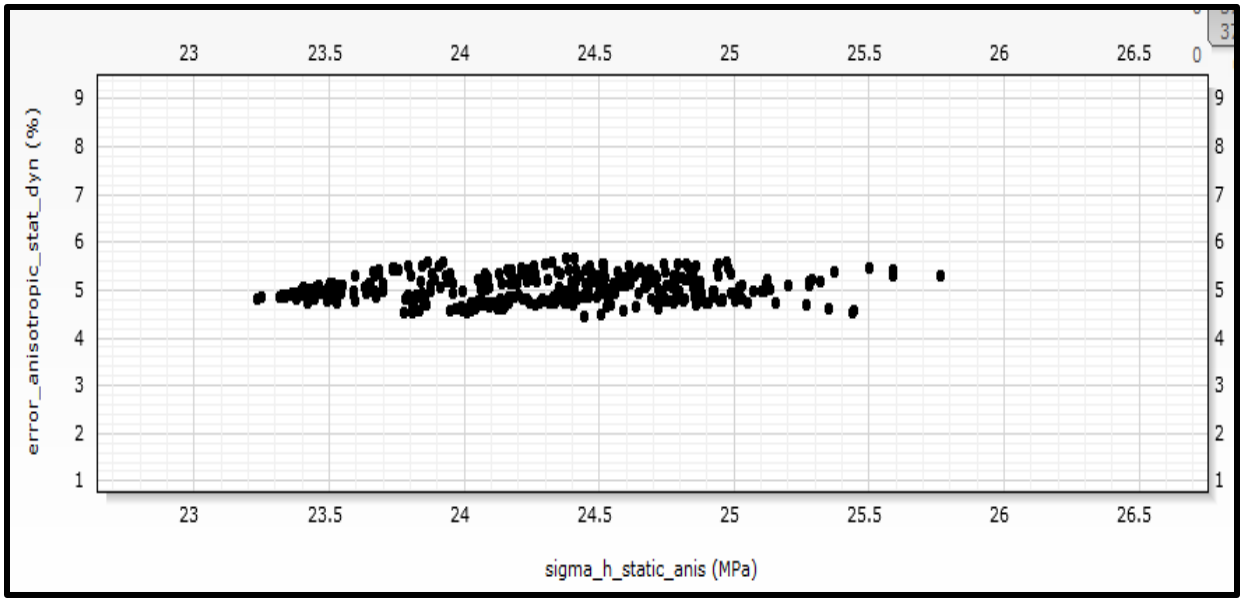

Figure 5.13 Percent error between dynamic anisotropic and static anisotropic calculations of σ_h for the selected reservoir intervals. Percent error generally ranges between 4.5-5.5 percent.

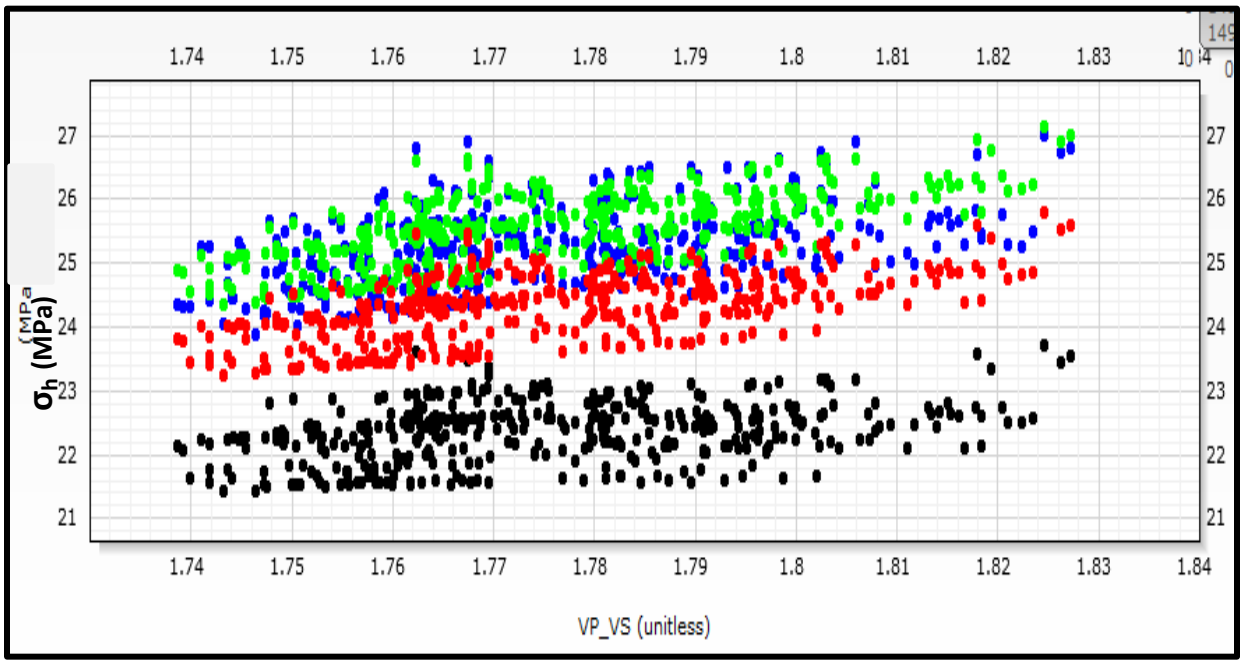

Figure 5.14. Minimum horizontal stress values for the selected reservoir zones. The black dots represent the isotropic static case; the red dots represent the anisotropic static case; the blue and green dots represent the dynamic isotropic and anisotropic cases, respectively. VP:VS was chosen for the X-axis for smoothness of presentation since the data are zoned.

The percent error values between the dynamic isotropic and anisotropic cases are negligible, ranging between *2* and *3* percent. However, the percent errors between the dynamic and static cases are more substantial. For the dynamic anisotropic versus static anisotropic case the percent error when assuming the dynamic case ranges between *4.5* and *5.5* percent. The isotropic static versus dynamic is the most acute: the percent error generally ranges between *12* and *16* percent. From these analyses we can conclude that, given data availability, assuming anisotropy is the best practice and that, when possible, it is best to obtain static correction ratios for correction.

In order to estimate how σ_h changes during production, I obtained a dataset from Maldonado (2010) with triaxial test results for the D chalk and D marl facies. I used the saturated *E* and *v* values and created plots that show how the dynamic minimum horizontal stress changes during production. The results can be shown in Figures 5.15 and 5.16.

Maldonado (2010) attempted to estimate ratios between the dynamic and static parameter cases. Strain gauge failure during triaxial testing prohibited discovery in the cases of the vertical chalk and marl. To calculate the static σ_h values with respect to pore and confining pressure I used the dynamic-to-static ratio Maldonado obtained for the horizontal D chalk, 1.5, and considered the D chalk elastically isotropic. The percent error calculated for σ_h using the saturated dataset is similar to the log-derived error. σ_{PP} for the Smoky Hill member in the Aristocrat well is roughly *20-25 MPa*, and the derived error ranges between *12-16 %*, which is close to the lab-derived values of *12-20 %* observed at *50 MPa* for the Maldonado dataset.

Figure 5.17 shows the percent error for the dynamic case with respect to various P_p and P_c values. The plot shows that percent error increases with increasing P_c. However, percent error is negatively correlated with P_p. This means that as pore pressure increases, the effects of making

improper assumptions concerning elastic parameters become less acute. It also means that as a reservoir drains the error in the calculated σ_h increases, and this is important to note since σ_h is important to estimate for pressure control and proppant selection purposes. The trend on the plot indicates that as differential pressure goes to zero the static and dynamic values of σ_h equal one another.

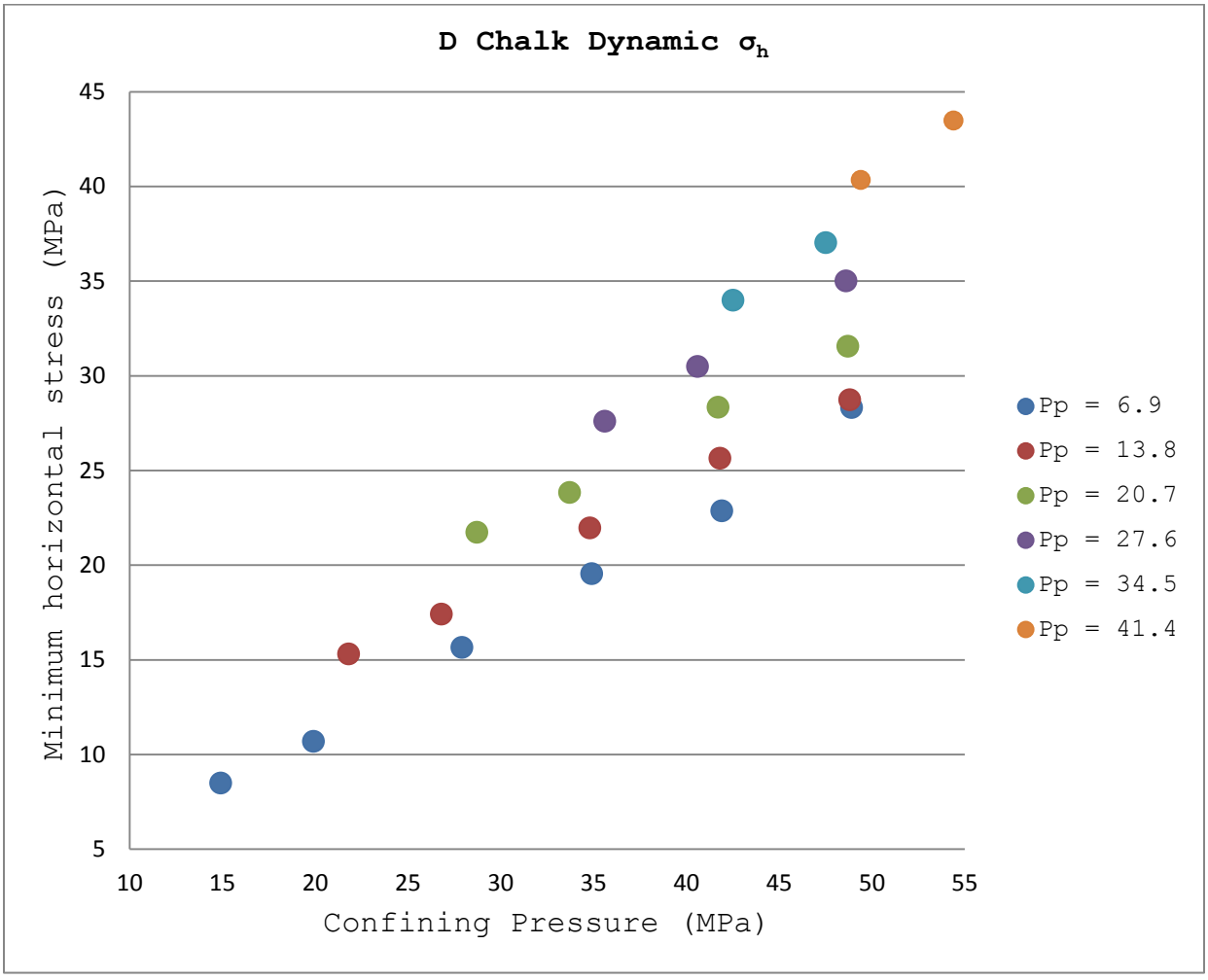

Figure 5.15. Minimum horizontal stresses calculated with dynamic elastic parameters for various pore and confining pressures. This chart indicates how minimum horizontal stress changes in a reservoir during production. The data is from triaxial experiments performed on samples of the D chalk.

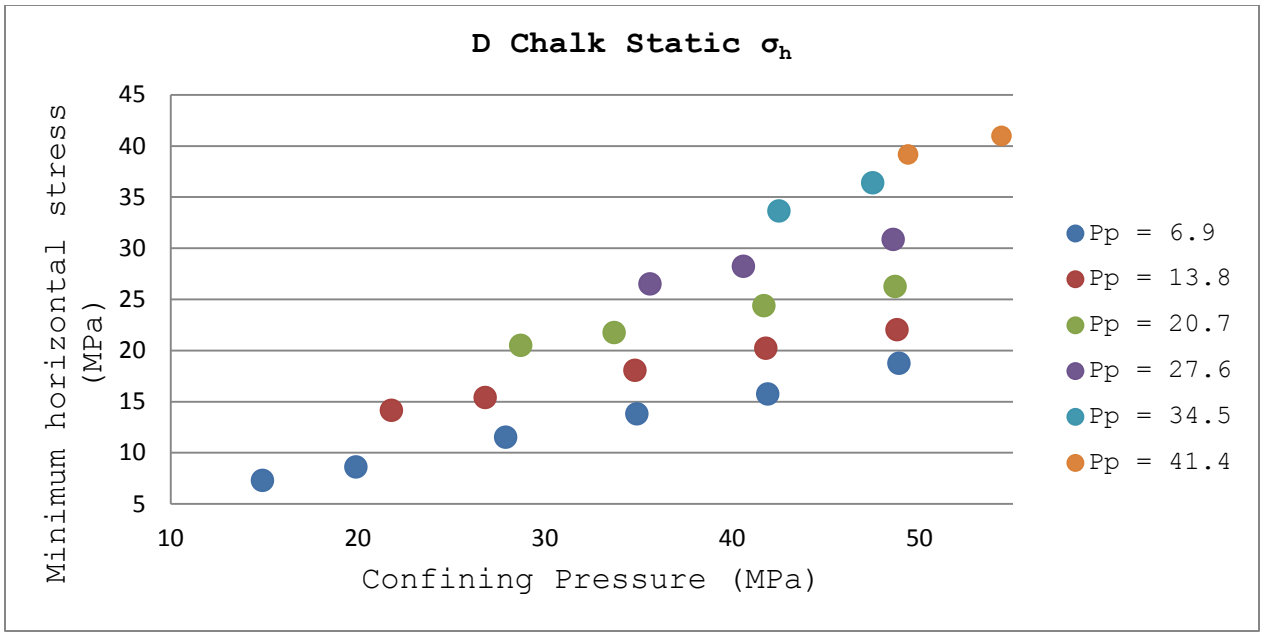

Figure 5.16. Minimum horizontal stresses calculated with static elastic parameters for various pore and confining pressures. This chart indicates how minimum horizontal stress changes in a reservoir during production. The data is from triaxial experiments performed on samples of the D chalk.

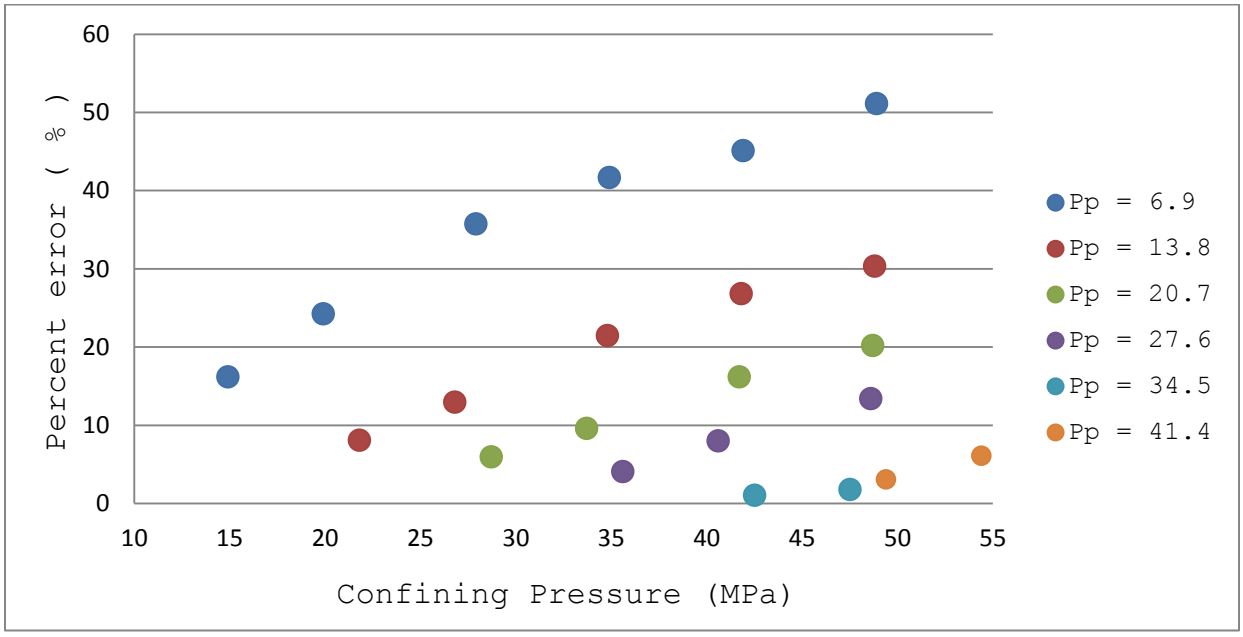

Figure 5.17. Percent error for minimum horizontal stress calculation at various pore and confining pressures for the D chalk. As confining pressure increases, the error in using the dynamic elastic parameter values increases. However, increasing pore pressure reduces assumptive error.

Conclusion

In this chapter we have discussed the elastic parameters, elastic anisotropy, and minimum horizontal stress. E and v are required inputs for calculating σ_h, and estimating them for the anisotropic case is important because they determine the value of the stress coupling coefficient, K_o. For the Smoky Hill member the chalk units are isotropic and the marl units are anisotropic due to preferential clay orientation. E and v both decrease as clay content increases. The chalk and marl samples measured contain 25 % and 35 % clay fraction, respectively. At 20 MPa confining pressure, measured dynamic to static ratios range between 1.25-1.43 for E_{chalk}; 1.81-2.16 for E_{marl}; 1.04-1.08 for v_{chalk}; and 2.27-2.38 for v_{marl}. At reservoir depths in the Smoky Hill member ratios are near unity.

Elastic anisotropy values for the Smoky Hill member decrease with increasing pressure and elastic anisotropy does not exist in our study wells at reservoir depth and pressure. To calculate the well log-derived elastic parameters we employed the ANNIE approximation and were successful due to the negligible δ values. The parameters were used to calculate minimum horizontal stress for the isotropic dynamic and static cases and the anisotropic dynamic and static cases. Under the dynamic isotropic assumption for σ_h the percent error ranges between 12-16%; under the anisotropic dynamic assumption percent error ranges between 4.5-5.5%; and the dynamic isotropic and anisotropic cases for the Smoky Hill member in our study area result in negligible error. The dynamic isotropic and anisotropic cases yield variable error values because for the anisotropic case the static correction is applied to the individual constants comprising K_o. We also compared minimum horizontal stress under varying confining and pore pressures and found that error increases during increasing confining pressures but decreases due to increasing

pore pressures. During hydrocarbon production pressure control requires greater error assumption as reservoir pressures approach the fracture closure stress.

CHAPTER 6

FRACTURE DENSITY DETERMINATION FROM WELL LOG DATA

6.1 Introduction

While minimum horizontal stress is important to determine for hydraulic fracture stimulation design optimization, it is also desirable to locate subsurface fracture networks to enhance production. Fracture detection is an important subject for hydrocarbon recovery, mine stability, waste isolation, and earthquake studies (Teng, 1998). Subsurface fracture networks are zones of increased permeability and storage capacity, and improved production rates in existing fields is currently very important to the petroleum industry. Fractured zones can also be zones to avoid during secondary and tertiary recovery phases due to the potential for fluid and solvent diffusion away from the reservoir. In both cases fractured-zone location improves field development planning and support the premise that fracture detection should be pursued when data is available. This chapter discusses the application of a downhole fracture detection inversion in the study area.

6.2 Background and methodology

Preferential orientation of fracture networks renders a medium azimuthally anisotropic with respect to seismic wave propagation (Bakulin et al., 1999; Ruger, 2001). Studies conducted by Tsvankin (1997) have also shown that P-wave signatures can constrain fracture density, and work by Sayers and Rickett (1997) and Ruger and Tsvankin (1997) show that P-wave signatures can also discriminate between dry, gas-filled, and fluid-filled fractures. The simplest fracture-detection model available assumes a horizontal axis of symmetry (HTI) caused by vertical

fractures in an isotropic host rock (Bakulin, 1999; Sil, 2013). This type of model was chosen to attempt location of fractured sections in the chalk units of the Smoky Hill member.

Use of wellbore data to obtain the physical characteristics of fracture networks depends on accurate assumptions involving the orientation and compliances of fractures and on the elastic properties of the host rock (Bakulin et al., 1999). Quality control is obtained by comparing the results of the wellbore data to effective medium theory, which, in this study, is Hudson's crack model (Hudson, 1980). Bakulin et al. (1999) showed that Hudson's model is equivalent to various other linear-slip models proposed (Schoenberg, 1980, 1983; Schoenberg and Douma, 1988; Schoenberg and Sayers 1995; Thomsen, 1995), and as long as fracture density remains low (< 0.1) Hudson's model can be compared to the results.

Wave reflection traveltimes in HTI media can be expressed through the HTI Thomsen-type parameters: ε^{v}, δ^{v}, and γ^{v} (Ruger, 1997; Tsvankin, 1997). It is important to note that these parameters are not equal to the generic parameters normally defined with respect to a horizontal symmetry axis (Bakulin et al., 1999). Chapter 4 discussed the laboratory (background) and borehole Thomsen parameters. Now that estimated the anisotropy of the background media has been estimated, one can attempt location of anomalies that enable the location of "sweet spots," or natural fractures that contain oil and/or gas. Since the maximum principal stress, σ_v, is vertical in the study area it was assumed that fractures are vertical and parallel to the maximum horizontal stress, σ_H. These conditions were assumed to result in an HTI medium (Ruger, 1998; Sil, 2013) where the source of anisotropy is vertical fractures. The unfractured host rocks, the A-D chalks, are considered isotropic.

Subsurface fractures generally occur in large sets with similar orientations (Aguilera, 1998) that are parallel to the maximum principal stress. Apertures may vary, but it is generally

accepted that in-situ fracture openings do not deviate substantially from an average of 0.02 to 0.03 mm (Romm, 1985; Bakulin et al., 1999). However, in this study the method applied only targets fracture density, and does not require the fracture porosity and aspect ratio. The only geologic assumption is that permeability and storage capacity have the potential to increase significantly with increasing fracture density, *e*, which is shown by Bakulin et al. (1999):

$$fracture\ density = e = \frac{number\ of\ fractures}{meter} \tag{6.1}$$

Assuming an HTI medium and penny-shaped, non-interactive fractures I derive the Thomsen-type parameters and fracture density, *e*, from a vertical well log containing $V_{P,}$ V_{S1}, $V_{S2,}$ and $\rho_{b.}$ The fast and slow S-wave velocities and shear stiffnesses are shown by Wang (2002) as:

$$\rho V_{S1}^2 = C_{44} \tag{6.2}$$

and

$$\rho V_{S2}^2 = C_{55} = C_{66} \tag{6.3}$$

C_{ij} represents the stiffness matrix elements of the HTI medium. Ruger (1998) shows γ^v as:

$$\gamma^v = \frac{V_{S2}^2 - V_{S1}^2}{2V_{S1}^2} \tag{6.4}$$

or by modifying Liu et al. (2000):

$$\gamma^v = -\frac{1}{2}\mu Z_T \tag{6.5}$$

where

$$\mu = C_{44} \tag{6.6}$$

C_{44} and μ are both ways to denote the shear modulus. Once Z_T is calculated I consider the penny-shaped fractures/cracks model and use a relationship defined by Sayers and Kachanov (1995):

$$\frac{Z_N}{Z_T} = 1 - \frac{v}{2}, \tag{6.7}$$

where Z_N and Z_T are the normal and tangential fracture compliances, and v is the Poisson ratio of the background isotropic medium. Once Z_N, Z_T, background V_P and V_S, and ρ_b are known then the compliance matrix (S_{ij}) for the HTI medium can be written as (Schoenberg and Sayers, 1995; Sil, 2013):

$$S_{ij} = \begin{bmatrix} \frac{\lambda+\mu}{\mu(3\lambda+2\mu)} + Z_N & -\frac{\lambda}{2\mu(3\lambda+2\mu)} & -\frac{\lambda}{2\mu(3\lambda+2\mu)} & 0 & 0 & 0 \\ -\frac{\lambda}{2\mu(3\lambda+2\mu)} & \frac{\lambda+\mu}{\mu(3\lambda+2\mu)} & -\frac{\lambda}{2\mu(3\lambda+2\mu)} & 0 & 0 & 0 \\ -\frac{\lambda}{2\mu(3\lambda+2\mu)} & -\frac{\lambda}{2\mu(3\lambda+2\mu)} & \frac{\lambda+\mu}{\mu(3\lambda+2\mu)} & 0 & 0 & 0 \\ 0 & 0 & 0 & \frac{1}{\mu} & 0 & 0 \\ 0 & 0 & 0 & 0 & \frac{1}{\mu} + Z_T & 0 \\ 0 & 0 & 0 & 0 & 0 & \frac{1}{\mu} + Z_T \end{bmatrix} \quad (6.8)$$

where λ is Lame's first parameter. Schoenberg and Sayers (1995) also show the stiffness matrix for the HTI medium, which can be written as:

$$C_{ij} = \begin{bmatrix} M_b(1-\delta_N) & \lambda(1-\delta_N) & \lambda(1-\delta_N) & 0 & 0 & 0 \\ \lambda(1-\delta_N) & M_b(1-r^2\delta_N) & \lambda(1-r\delta_N) & 0 & 0 & 0 \\ \lambda(1-\delta_N) & \lambda(1-r\delta_N) & M_b(1-r^2\delta_N) & 0 & 0 & 0 \\ 0 & 0 & 0 & \mu & 0 & 0 \\ 0 & 0 & 0 & 0 & \mu(1-\delta_T) & 0 \\ 0 & 0 & 0 & 0 & 0 & \mu(1-\delta_T) \end{bmatrix} \quad (6.9)$$

where

$$M_b = \lambda + 2\mu, \quad (6.10)$$

$$r = \frac{\lambda}{K}, \quad (6.11)$$

$$\delta_T = \frac{Z_T\mu}{1+Z_T\mu}, \quad (6.12)$$

and

$$\delta_N = \frac{Z_N K}{1+Z_N K}, \tag{6.13}$$

where K is the bulk modulus, r is a compressibility coefficient, and δ_T and δ_N are the tangential and normal fracture weaknesses, respectively. Once the values for the stiffness matrix have been derived we can derive the Thomsen-type parameters, ε^v and δ^v using equations from Ruger (1998):

$$\varepsilon^v = \frac{C_{11}-C_{33}}{2C_{33}} \tag{6.14}$$

and

$$\delta^v = \frac{(C_{13}+C_{55})^2-(C_{33}-C_{55})^2}{2C_{33}(C_{33}-C_{55})} \tag{6.15}$$

The HTI anisotropy parameters should show a deviation from the background values in the presence of fractures, and once the HTI anisotropy parameters have been derived from the well log the fracture density, e, can be derived from the following equation (Bakulin et al., 1999):

$$\delta_T = \frac{16e}{3(3-2g)} \tag{6.16}$$

In Equation 6.16, g is the square of the vertical V_S:V_P ratio, e is fracture density, and δ_T is the fracture compliance introduced earlier.

6.3 Field data and comparisons to previous work

Previous research applied fracture detection methodology to a tight gas sand reservoir located in Colorado, USA (Sil, 2013). Sil cites a 1991 study by Lorenz and Finley which indicates a regional stress regime resulting in vertical fractures at the reservoir level. The method derives the fracture density, e, by using the normal fracture weakness, δ_N:

$$\delta_N = \frac{16e}{3(3-2g)} \tag{6.17}$$

, however, I choose to use the identity given by Bakulin and Tsvankin (1999):

$$\delta_T = \frac{16e}{3(3-2g)} \tag{6.18}$$

This study employed Sil's method, but modified the approach to constrain it to the existing fracture anisotropy theory, i.e. by employing the δ_T-derived fracture density. The Noble Aristocrat well, Wattenberg Field, CO contains gamma ray, density, P-wave, and dipole shear-wave data (Figure 6.1). Figure 6.2 shows the fracture density, e, plotted alongside the Thomsen-type anisotropy parameters ε^v, δ^v, and γ^v. The inversion indicates minor fracturing in the Aristocrat well, with e values ranging between 0-0.01. Anisotropy correlates with the indicated fractures and anisotropy parameter peaks are observed where fracture density peaks. The sign of the anisotropy parameters is dependent on whether the greater compliance is observed fracture-normal or bedding normal.

Bakulin et al. (1999) gave several relationships that one should expect to observe between *e* and the Thomsen-type parameters, and these relationships were plotted to check how the inversion complied with the theoretical constraints. These relationships are shown in Equations 6.17-19. For dry (or gas-filled) cracks:

$$\varepsilon^{v} = -\frac{8}{3} \tag{6.19}$$

$$\delta^{v} = -\frac{8}{3} e \left[1 + \frac{g(1-2g)}{(3-2g)(1-g)}\right] \tag{6.20}$$

$$\gamma^{v} = -\frac{8e}{3(3-2g)} \tag{6.21}$$

The anisotropy parameters are shown plotted against dry fracture density in Figures 6.3, 6.4, and 6.5. The data from the Aristocrat well fit the theoretically predicted values very well. γ^{v} fits the predicted values near-perfectly, while there are minor trend deviations correspondent to the values of ε^{v} and δ^{v}. The data fits the dry fractures model well enough to assume, when basing the conclusion off the fracture model and the *TNPH/DPHI* crossover observed in Chapter 5, that gas is the primary hydrocarbon source in the Aristocrat well (Bakulin et al., 1999).

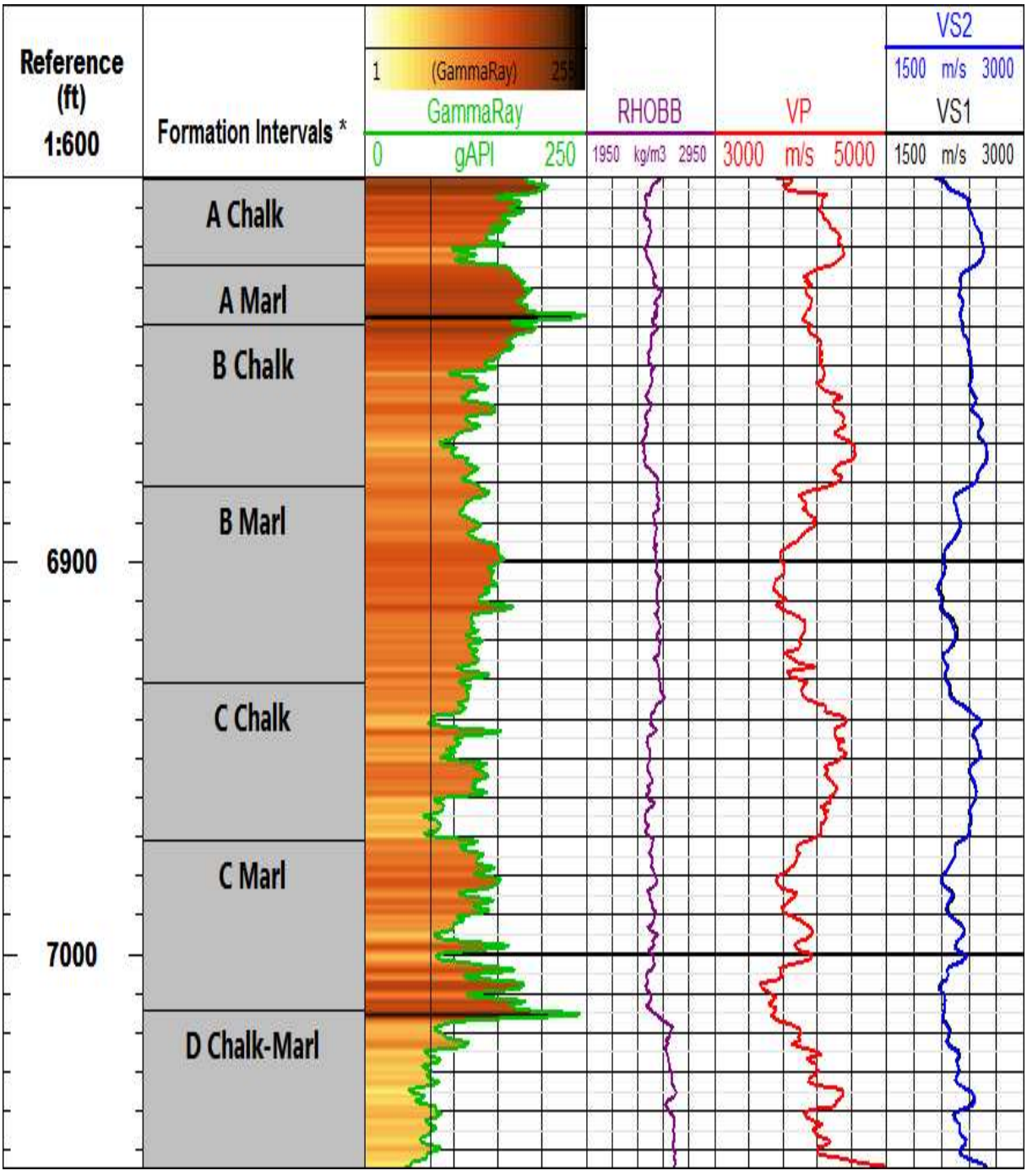

Figure 6.1 Gamma ray, density (RHOBB), P-wave (VP), and dipole shear-wave data (VS1 and VS2) for the Noble Aristocrat well. This data was used to derive the HTI Thomsen parameters and fracture density.

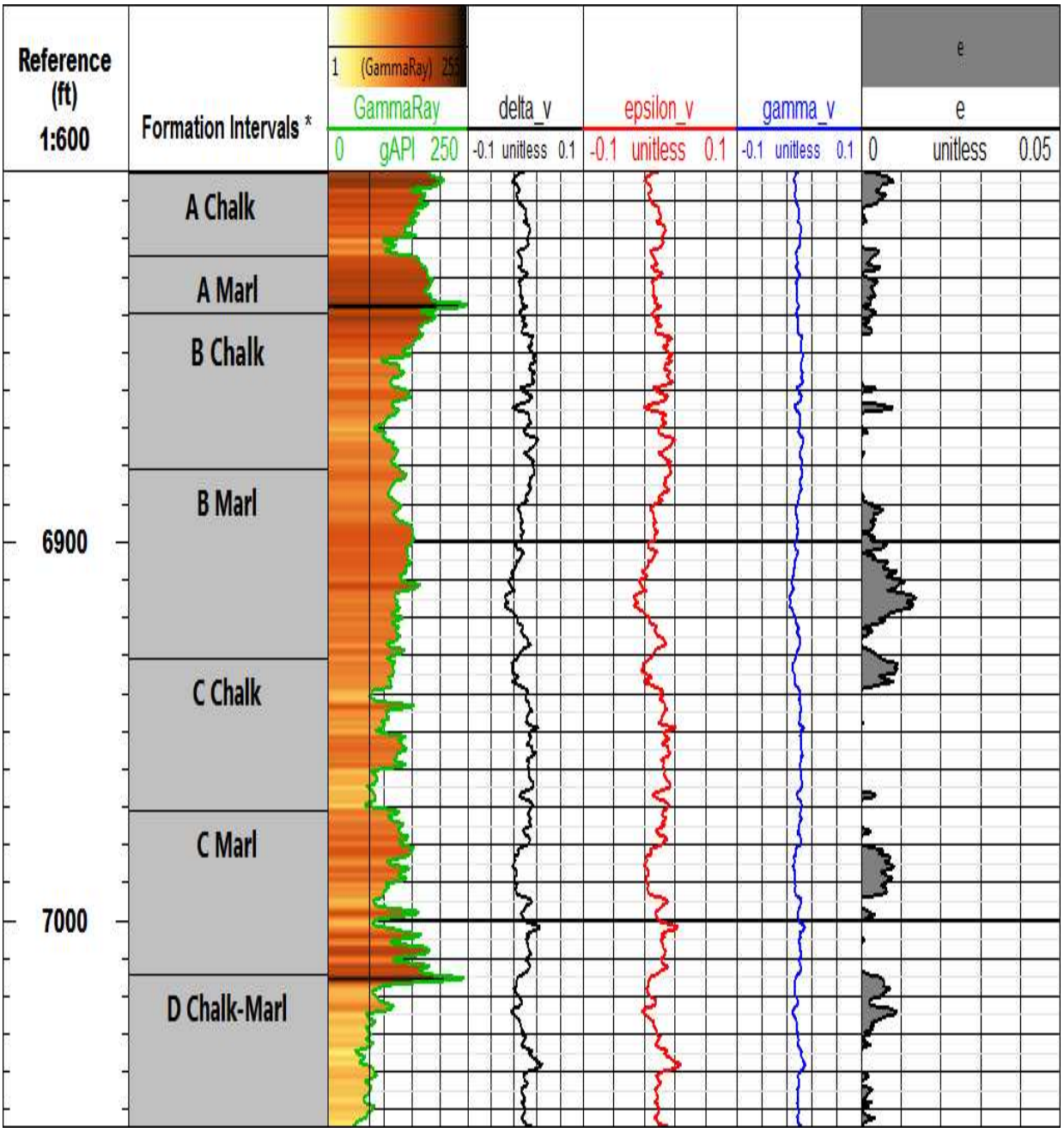

Figure 6.2. Fracture density, *e*, plotted with the Thomsen-type anisotropy parameters for the Noble Aristocrat Well, Wattenberg Field, CO.

The anisotropy in the Smoky Hill member is low enough such that fracture detection is theoretically possible by assuming an isotropic background host rock with a horizontal symmetry axis resulting from vertical fractures.

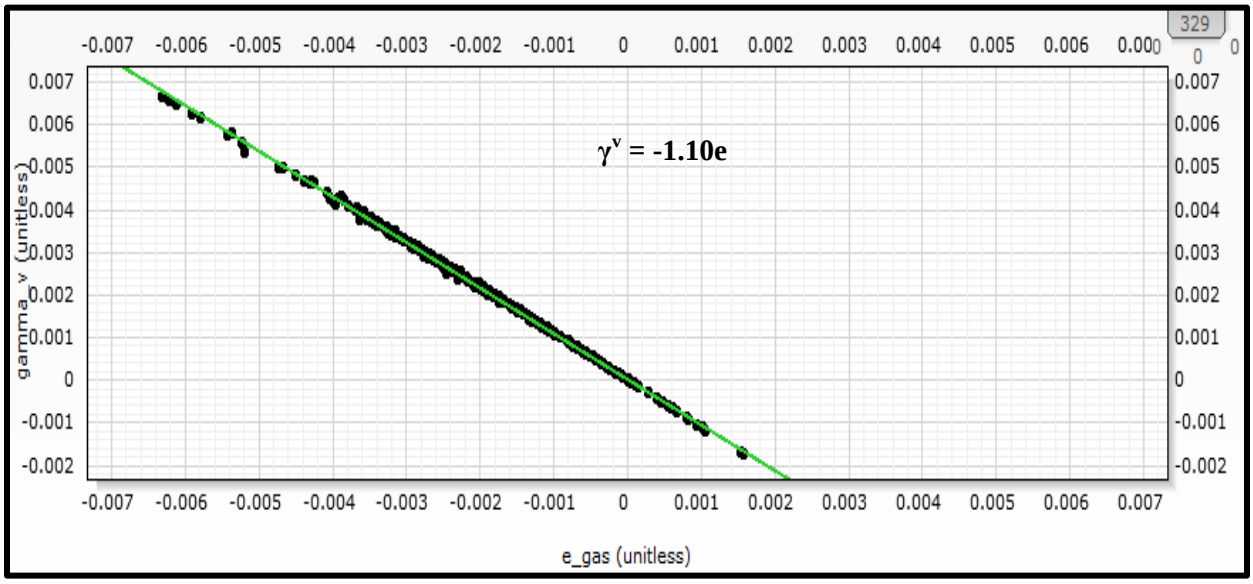

Figure 6.3. Gamma vs. e for fractured sections of the Smoky Hill member. The observed fractures fit the theoretical data very well.

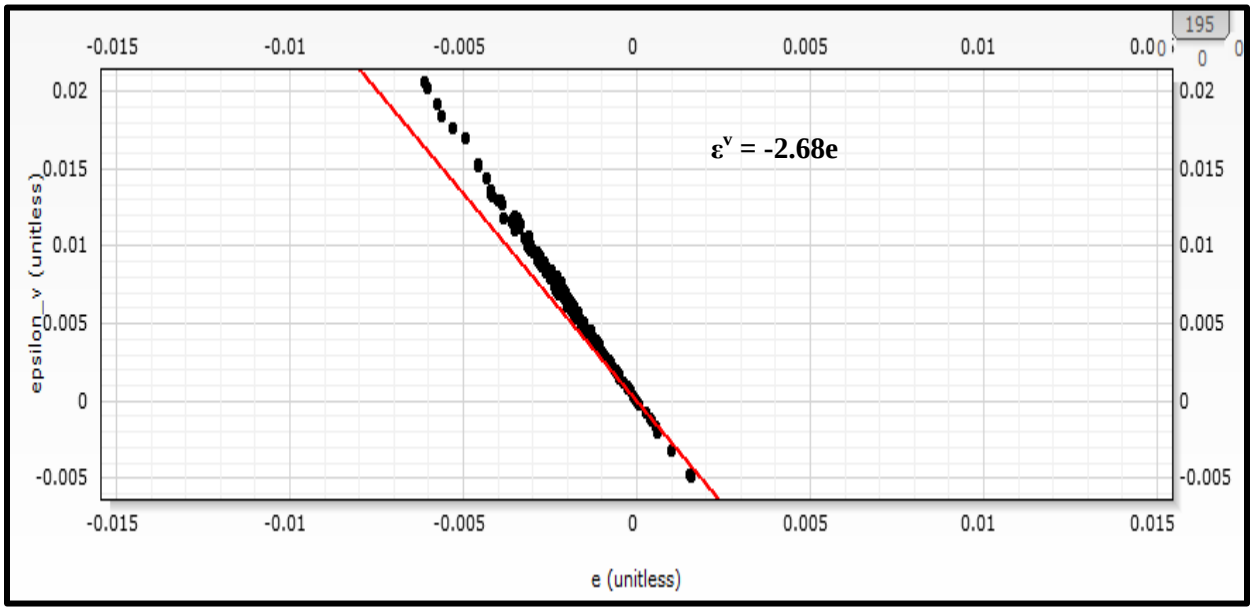

Figure 6.4 Epsilon vs. e for fractured sections of the Smoky Hill member. The observed values fit the theoretical trend well.

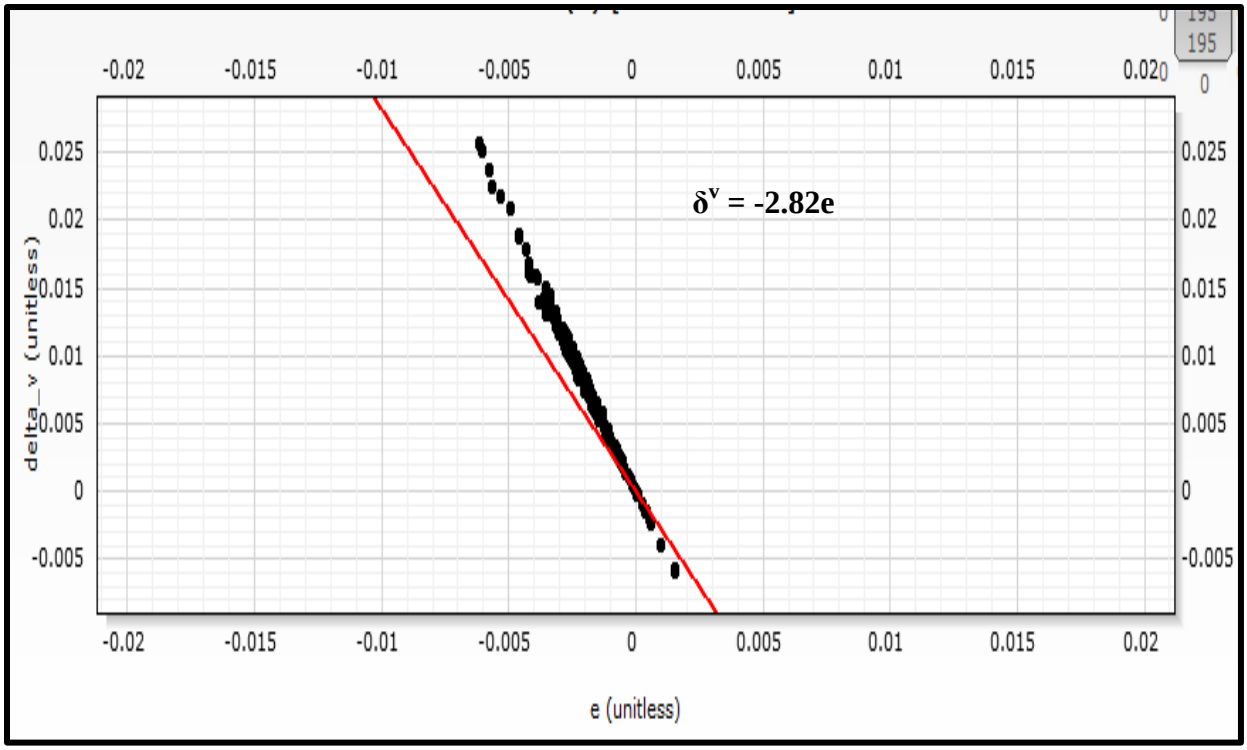

Figure 6.5 Delta vs. e for fractured sections of the Smoky Hill member. The observed values fit the predicted trend fairly well.

The Thomsen-type parameter values are controlled by the fracture weaknesses and the ratio of λ and μ, which is expressed by g, the square of V_S:V_P. It is important to constrain the values of the various parameters since hydrocarbon classification relies on accurate petrophysical characterization, and in seismic surveys fracture content can be estimated utilizing fracture inversion methods. Bakulin and Tsvankin show that the shear-wave splitting parameter, γ^v, can be written as:

$$\gamma^v = -\frac{\delta_T}{2}. \tag{6.22}$$

By constraining g and assuming $0.35 \leq V_S/V_P \leq 0.65$, or equivalently assuming $0.12 \leq g \leq 0.42$, one is able to constrain ε^v and δ^v by specifying the range of γ^v. For each pair of g and δ_T

values, Bakulin et al. calculated the parameter values for various cases of δ_N ranging between 0 and 1. Results where Z_N:Z_T exceeded 1, which is possible when implementing Hudson's (1980, 1981) theory, were ignored. For the Aristocrat well, γ^v values were less than |0.03|, and the theoretical expectations are shown in Figure 6.6 below. In figure 6.7 ε^v versus δ^v is shown. For dry cracks Bakulin et al. also state that anisotropy will be elliptical, from the image I conclude that dry cracks are the primary contributor to anisotropy and excess compliance in the well.

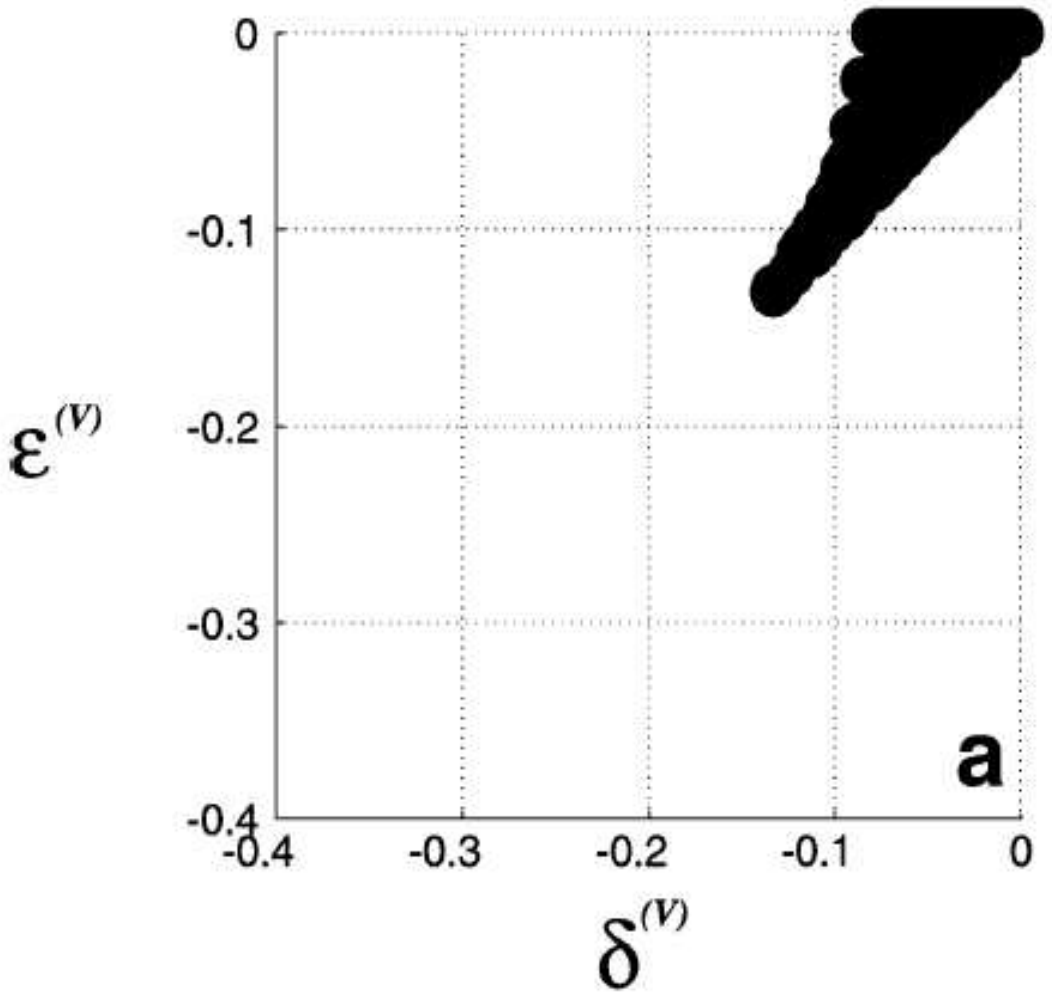

Figure 6.6. Possible ranges for ε^v and δ^v in our study area, where $|\gamma^v| \leq 0.05$. Image sourced from Bakulin et al. (1999).

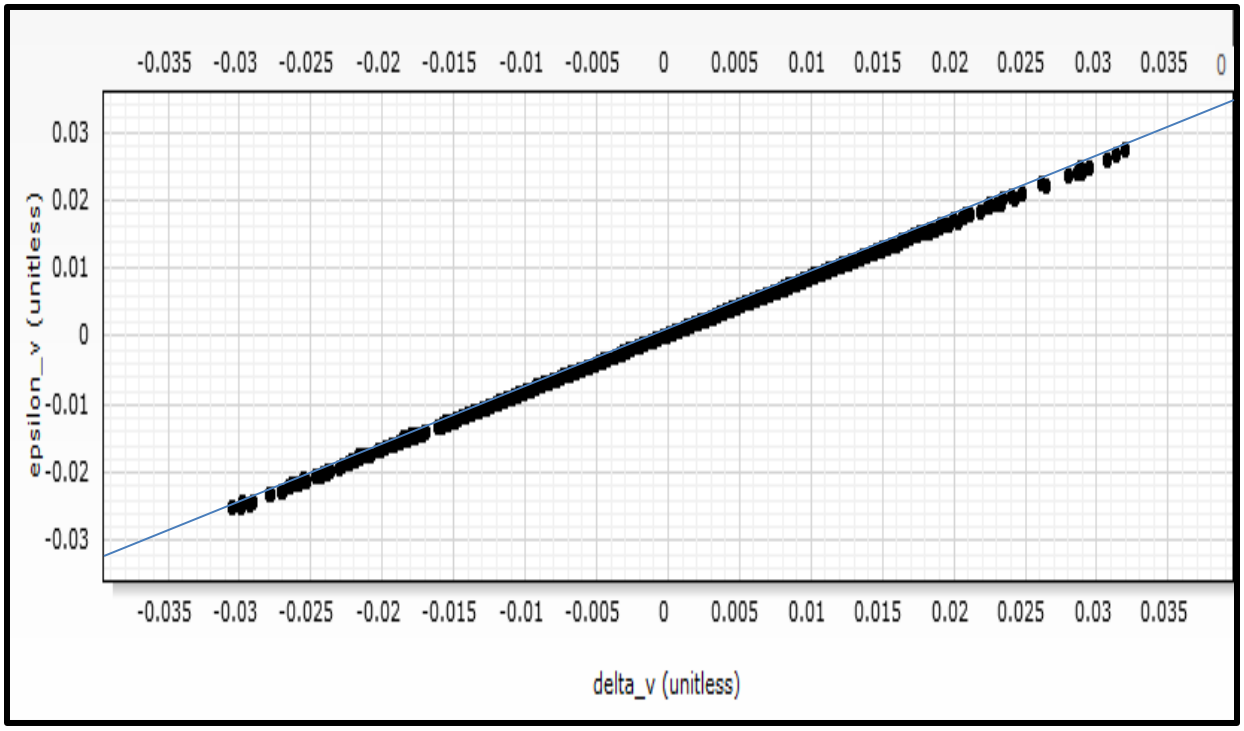

Figure 6.7. Observed ε^v and δ^v for the Aristocrat well. The anisotropy parameters fall within the theoretical boundaries.

Hudson's crack model (1980) was applied to the laboratory core data, and was then compared to the well log-derived parameters (6.8). Hudson's crack model was chosen due to the low limit for crack density, which is less than 0.1 (Hudson, 1981; Bakulin et al., 1999). To plot the laboratory data against the well log data I first calculated the various C_{ij}^{eff} values. I used the values of C_{33}, C_{11}, C_{13}, C_{44}, and C_{66} to compute ε^v, γ^v, and δ^v. The anisotropy parameters were first calculated for the VTI case and then converted using the method of Ruger (2001). This method was discussed in Chapter 4. The parameters were fitted to the well log with the fracture density, *e*. The Hudson Crack Model fits the γv curve nearly perfectly, and with the exception of some higher fracture density portions, δ^v_{Hudson} fits the data well, also. ε^v_{Hudson} predicts the well log-derived values poorly, primarily since Hudson's crack model fails to account for the

variability of g. Modeling in dry cracks should incorporate the dry crack relationship for γv to be predictive.

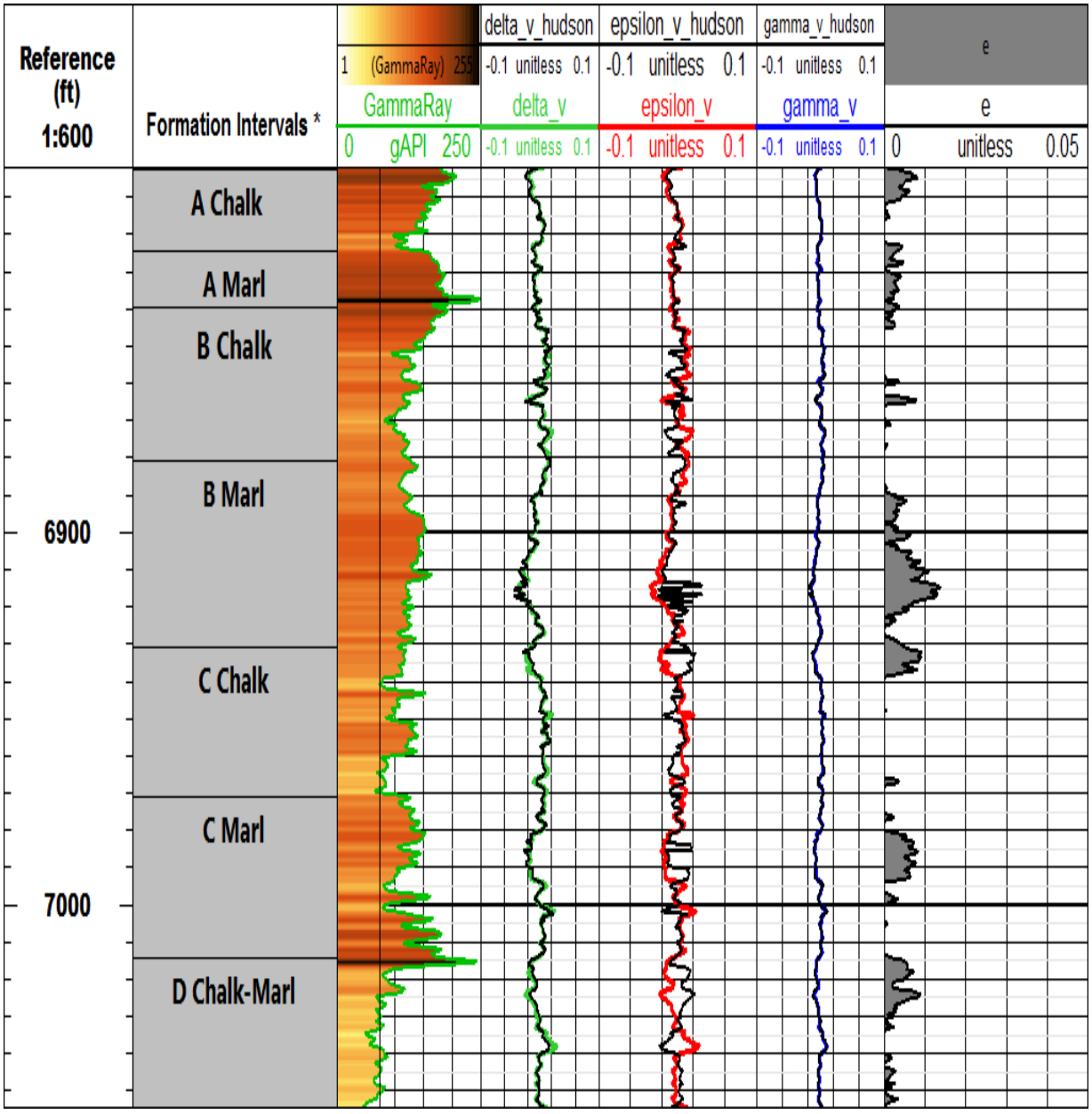

Figure 6.8 Comparison of well log-derived Thomsen-type parameter values and Hudson Crack Model-estimated values. The Hudson Crack Model fits the data well.

6.4 Discussion

This study has demonstrated a method to derive fracture-induced seismic anisotropic parameters from vertical well logs. The assumptions required for the method are that vertical P-wave velocity equals background isotropic P-wave velocity, and that the main cause of the anisotropy is vertical fractures, which result in a medium similar to that shown in Figure 6.9.

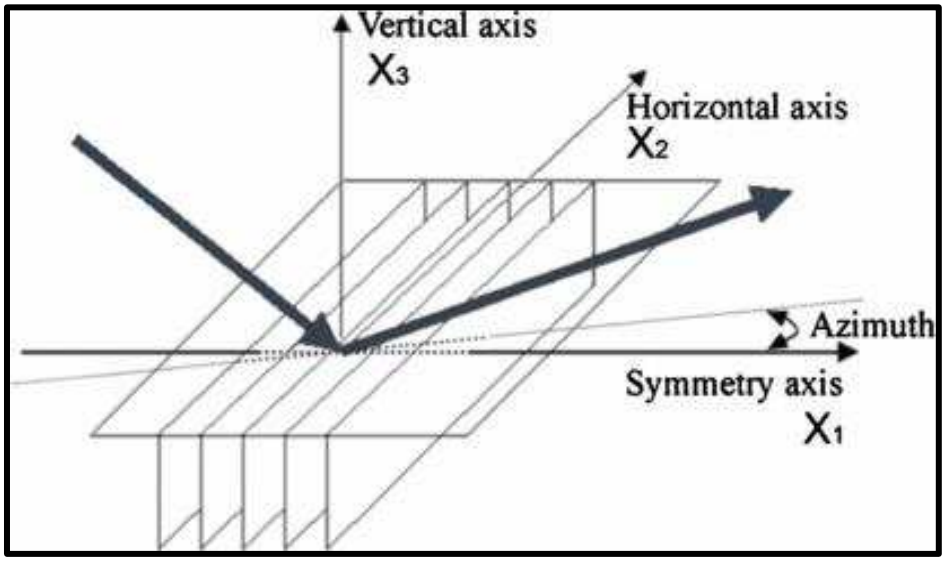

Figure 6.9. Sketch of a fractured HTI model. The symmetry axis is intersected by the horizontal axis. Shear waves polarized parallel and normal to the horizontal axis have different velocities. In nature this phenomenon may be caused in HTI media by upturned layered rocks or vertical fractures.

Teng (1998) showed the mathematical equivalence of the suite of linear-slip fracture models, an equivalence that holds true in both the cases of interacting and non-interacting cracks. Therefore, those theories which assume an effective medium comprising a homogenous medium of fracture-reduced stiffnesses should be inappropriate for modeling fractures using any approach assuming fracture-driven excess compliance. When analyzing fracture-driven anisotropy, the sign of the anisotropy parameters will be negative in the presence of fractures and

positive when excess compliance is greatest in the bedding normal direction. Hudson's crack model, when applied to the chalk data from the lab, fits the calculated anisotropy parameters well. This means that modeling other characteristics such as inclusions and fluid content should be possible for the reservoir chalks as well. To model dry cracks the assumption $\gamma^v=\varepsilon^v$ seems to be valid since the predicted values of ε^v fail to account for the variability of the Lame parameters.

Conclusion

This chapter detailed the application of a linear-slip fracture detection inversion in the Aristocrat well. Since previous studies indicate the equivalence of linear-slip crack methods it was determined that it is physically possible to determine the macro-features of existing cracks, which in the case of this study is the fracture density. This conclusion also rests on the assumption that interconnected and non-interconnected fracture-induced compliances are indistinguishable.

Due to fluid effects, it is determined that the normal fracture weakness, δ_N, lacks the precision required to locate subsurface fractures using the method employed by Sil (2013). δ_T, which isn't sensitive to fluid content, is more appropriate. Moreover since the P-wave anisotropy, ε^v, goes to zero in the presence of fluids large errors may result without correction factors where fluid-filled fractures exist.

Crack models that assume parallel cracks in a homogenous, isotropic medium are appropriate for modeling fracture density in mature reservoir intervals in the Smoky Hill member. Since fracture detection methods are basically a measurement of velocity deviation from a specified background value the presence of soft materials in bedding layers and fractures changes the sign of the anisotropy parameters. These methods can be employed alongside borehole imagery and compared with laboratory data to check accuracy. Fracture-detection

methodology is compatible with borehole VSP data and can be used to tie well log measurements in seismic surveys to inform well spacing and other development decisions.

CHAPTER 7

CONCLUSIONS AND FUTURE WORK

7.1 Conclusions

The mechanical properties were measured for the D chalk and D marl facies in the Smoky Hill member of the Niobrara Formation. The D chalk is found to be isotropic and the D marl is found to be weakly anisotropic. However, due to the lower maturity of the laboratory samples we expect velocity anisotropy to be lower at reservoir depths and in locales where a higher vitrinite reflectance is observed (Vonorio et al., 2010).

The laboratory Thomsen parameters were applied to well log data to estimate formation anisotropy in a mature region (R_o=1.2) of Wattenberg Field, Colorado. Velocity anisotropy was found negligible at reservoir depths. The near-zero values of δ enabled application of the ANNIE approximation (Schoenberg and Sayers, 1996) to find the unknown stiffness tensors C_{13}, C_{12}, and C_{11}. Due to the pervasive practice of erroneously setting δ to zero during application of ANNIE (Higgins, 2008; Havens, 2012) we modeled the errors in the uniaxial strain approximation resultant from underestimating δ. Modifying the δ equation in the presence of strong stress anisotropy dramatically underestimates minimum horizontal stress.

We measured the static and dynamic elastic parameters in the laboratory to describe the elastic anisotropy and the *dyn:stat* ratio. The static Young's modulus was lower than the dynamic Young's modulus due to the soft components undergoing greater elastic deformation during large-strain static loading (Sone and Zoback, 2013). This makes the materials appear more compliant. The D chalk, containing lower clay fraction than the D marl, is the stiffer facies and has lower directional *dyn:stat* values. The laboratory data shows the D chalk is elastically isotropic.The static and dynamic values were used to calculate minimum horizontal stress using

isotropic and anisotropic assumptions. Using static isotropic assumptions the implied error when calculating minimum horizontal stress is high, ranging between -8 to -10%, and the implied error when calculating minimum horizontal stress under dynamic anisotropic assumptions is low, ranging between 3-4 %. When using dynamic assumptions the difference between the isotropic and anisotropic case for the Smoky Hill member is negligible, ranging between 1-3 %. Using saturated samples in the presence of pore and confining pressure we found that error increases as confining pressure increases and pore pressure decreases.

A fracture detection method was applied to data for the Aristocrat well. Since previous studies indicate the equivalence of linear-slip crack methods it was determined that it is physically possible to determine the macro-features of existing cracks, which in the case of this study is the fracture density. This conclusion also rests on the assumption that interconnected and non-interconnected fracture-induced compliances are indistinguishable. Due to the effects of fluid content on anisotropy δ_T, the tangential fracture weakness, is more suitable for finding fracture density.

Crack models that assume parallel cracks in a homogenous, isotropic medium can be used to locate zones of high fracture density. Since fracture detection methods are basically a measurement of velocity deviation from a specified background value the sign of the anisotropy parameters change with respect to bedding-normal and fracture-normal compliance. When modeling dry cracks assuming $\gamma^v=\varepsilon^v$ can account for the variability of g, which isn't accounted for by Hudson's crack model (1980). Future work aiming to detect fractures in wells should employ borehole imagery to ascertain that the measured fracture density corresponds to real cracks.

REFERENCES CITED

Aguilera, R., 1998, Geologic aspects of naturally fractured reservoirs: The Leading Edge, 17, 1667–1670.

Alqahtani, A. A. (2013). Effect of mineralogy and petrophysical characteristics on acoustic and mechanical properties of organic rich shale. Unconventional Resources Technology Conference (URTEC).

Bakulin, A., Grechka, V., and Tsvankin, I. "Estimation of fracture parameters from reflection seismic data-Part I: HTI model due to a single fracture set." *Geophysics* 65.6 (2000): 1788-1802.

Dellinger, J., & Vernik, L. (1994). Do traveltimes in pulse-transmission experiments yield anisotropic group or phase velocities? *Geophysics*,*59*(11), 1774-1779.

ElGhonimy, R.S., 2015. Petrophysics, Geochemistry, Mineralogy, and Storage Capacity of the Niobrara Formation in the Aristocrat PC H11-07 Core, Wattenberg Field, Denver Basin, Colorado. M.S. thesis, Colorado School of Mines.

Eisinger, C., ed. 2011. "Colorado's New Oil Boom-The Niobrara" *Rock Talk.* Vol. 13, No. 1.

Havens, J. (2011). "Mechanical Properties of the Bakken Formation." M.S. thesis, Colorado School of Mines.

Havens, J. & Batzle, M. (2014). Thomsen parameter relationships and estimation from laboratory ultrasonic data. SEG Abstract.

Higgins, S., Goodwin, S., Donald, A., Bratton, T., & Tracy, G. 2008. Anisotropic stress models improve completion design in the Baxter Shale. In: SPE Annual Technical Conference and Exhibition.

Higley, D.K., and Cox, D.O., 2007, Oil and gas exploration and development along the front range in the Denver Basin of Colorado, Nebraska, and Wyoming, in Higley, D.K., Petroleum systems and assessment of undiscovered oil and gas in the Denver Basin Province, Colorado, Kansas, Nebraska, South Dakota, and Wyoming— USGS Province 39: U.S. Geological Survey Digital Data Series DDS–69–P, ch.2, 41p.

Hornby, B. E., Schwartz, L. M., & Hudson, J. A. (1994). Anisotropic effective-medium modeling of the elastic properties of shales. *Geophysics*,*59*(10), 1570-1583.

Hornby, B., Wang, X., & Dodds, K. (2003). Do we measure phase or group velocity with dipole sonic tools?. In *65th EAGE Conference & Exhibition*.

Hudson, J. A., 1980, Overall properties of a cracked solid: Math. Proc. Camb. Phil. Soc., 88, 371–384.

Hudson, J.A., 1981,Wave speeds and attenuation of elastic waves in material containing cracks: Geophys. J. Roy. Astr. Soc., 64, 133–150.

Jaeger, J., Cook, N. and Zimmerman, R. 2007. *Fundamentals of Rock Mechanics.* Malden: Blackwell Publishing.

Karig, D. E., & Hou, G. (1992). High-stress consolidation experiments and their geologic implications. *Journal of Geophysical Research: Solid Earth (1978–2012)*, *97*(B1), 289-300.

Katahara, K. (2009, January). Lateral earth stress and strain. In *2009 SEG Annual Meeting*. Society of Exploration Geophysicists.

Kauffman, E.G. "Geological and biological overview: Western Interior Cretaceous basin." *The Mountain Geologist* (1977).

King, M. S. 1964. Wave Velocities and Dynamic Elastic Moduli of Sedimentary Rocks. Ph.D. thesis, University of California, Berkeley.

Liu, E., X.-Y. Li, and J. H. Queen, 2000, Discrimination of pore fluids from P and converted shear-wave AVO analysis, in L. Ikelle, and A. Gangi, eds., Anisotropy 2000: Fractures, converted waves and case studies: Proceedings of the Ninth International Workshop on Seismic Anisotropy, SEG, 203–221.

Lorenz, J. C., & Finley, S. J. (1991). Regional Fractures II: Fracturing of Mesaverde Reservoirs in the Piceance Basin, Colorado (1). *AAPG Bulletin,75*(11), 1738-1757.

Maldonado, A. 2011. Elastic and mechanical properties of the Niobrara Formation with application to hydraulic fracture design. M.S. thesis, Colorado School of Mines.

Mavko, G., Mukerji, T., & Dvorkin, J. 1998. The rock physics handbook. Cambridge University Press, Cambridge.

Passey, Q. R., Bohacs, K., Esch, W. L., Klimentidis, R., & Sinha, S. (2010, January). From oil-prone source rock to gas-producing shale reservoir-geologic and petrophysical characterization of unconventional shale gas reservoirs. In *International oil and gas conference and exhibition in China*. Society of Petroleum Engineers.

Pollastro, R. and Scholle P. 1986. “Exploration and development of hydrocarbons from low permeability chalks-an Example from The Upper Cretaceous Niobrara Formation, Rocky Mountain Region” in *Geology of tight gas reservoirs: AAPG Studies in Geology*, edited by Spencer, C. and Mast, R. No. 24: 129-141.

Pollastro, R. 1992. “Natural fractures, composition, cyclicity, and diagenesis of the Upper Cretaceous Niobrara Formation, Berthoud Field, Colorado” in *Geological Studies*

Relevant to Horizontal Drilling: Examples from Western North America: Rocky Mountain Association of Geologists edited by Schmoker, J., Coalson, E., and Brown, C. 243-255.

Revil, A., 1999, Pervasive Pressure-Solution Transfer: a Poro-Visco-Plastic Model. Geophysical Research Letters, Vol. 26, No. 2, pp. 255-258, 15 January 1999.

Rice, D.D., and Shurr, G.W. "Patterns of sedimentation and paleogeography across the Western Interior Seaway during time of deposition of Upper Cretaceous Eagle Sandstone and equivalent rocks, Northern Great Plains." Rocky Mountain Section (SEPM), 1983.

Romm, E. S., 1985, Structural models of rocks pore space: Nedra (in Russian).

Ruger, Andreas. 1996. Reflection coefficients and azimuthal AVO analysis in anisotropic media. Ph.D. thesis, Colorado School of Mines.

Rüger, A., & Tsvankin, I. (1997). Using AVO for fracture detection: Analytic basis and practical solutions. *The Leading Edge*, *16*(10), 1429-1434.

Rüger, A. (1998). Variation of P-wave reflectivity with offset and azimuth in anisotropic media. *Geophysics*, *63*(3), 935-947.

Rüger, A. (2001). *Reflection coefficients and azimuthal AVO analysis in anisotropic media*. Society of Exploration Geophysicists.

Sayers, C. M., & Kachanov, M. (1995). Microcrack-induced elastic wave anisotropy of brittle rocks. *Journal of Geophysical Research-All Series-100*, 4149-4149.

Sayers, C. M., & Rickett, J. E. (1997). Azimuthal variation in AVO response for fractured gas sands. *Geophysical Prospecting*, *45*(1), 165-182.

Sayers, C. M. (2005, June). Seismic Anisotropy of Shales-What Determines the Sign of Thomsen's Delta Parameter?. In *67th EAGE Conference & Exhibition*.

Schoenberg, M. (1980). Elastic wave behavior across linear slip interfaces.*The Journal of the Acoustical Society of America*, *68*(5), 1516-1521.

Schoenberg, M. (1983). Reflection of elastic waves from periodically stratified media with interfacial slip. *Geophysical Prospecting*, *31*(2), 265-292.

Schoenberg, M., & Douma, J. (1988). Elastic wave propagation in media with parallel fractures and aligned cracks. *Geophysical Prospecting*, *36*(6), 571-590.

Schoenberg, M., & Sayers, C. M. (1995). Seismic anisotropy of fractured rock. *Geophysics*, *60*(1), 204-211.

Schoenberg, M., F., Muir, & Sayers, C. 1996. Introducing Annie: A Simple Three Parameter Anisotropic Velocity Model for Shales. Journal of Seismic Exploration, 5, 35-49.

Shaw, R. K., & Sen, M. K. (2006). Use of AVOA data to estimate fluid indicator in a vertically fractured medium. *Geophysics*, *71*(3), C15-C24.

Sil, S. "Fracture parameter estimation from well-log data." *Geophysics* 78.3 (2013): D129-D134.

Sone, H., and Zoback, M. "Mechanical properties of shale-gas reservoir rocks—Part 1: Static and dynamic elastic properties and anisotropy." *Geophysics* 78.5 (2013): D381-D392.

Sonnenberg, S. 2011. *The Niobrara Petroleum System: A New Resource Play in the Rocky Mountain Region.* Niobrara Consortium: Colorado School of Mines.

Surlyk, F., Dons, T., Clausen, C., and Higham, J. 2003. "Upper Cretaceous". In *The Millenium Atlas: petroleum geology of the central and northern North Sea*, edited by Evans, D., Graham, C., Armour, A., and Bathurst, P., 213-233. London: The Geological Society of London. Weimer, R. 1996. *Guide to the Petroleum Geology and Laramide Orogeny, Denver Basin and Front Range,Colorado*. Denver: Colorado Geological Survey.

Thomsen, L. 1986. Weak elastic anisotropy. Geophysics, 51, 1954-1966.

Thomsen, L. (1995). Elastic anisotropy due to aligned cracks in porous rock.*Geophysical Prospecting*, *43*(6), 805-829.

Tsvankin, I. (1996). P-wave signatures and notation for transversely isotropic media: An overview. *Geophysics*, *61*(2), 467-483.

Tsvankin, I. (1997). Reflection moveout and parameter estimation for horizontal transverse isotropy. *Geophysics*, *62*(2), 614-629.

Tsvankin, I., Helbig, K., & Treitel, S. (2001). Seismic signatures and analysis of reflection data in anisotropic media.

Vanorio, T., Mukerji, T., & Mavko, G. (2008, January). Elastic Anisotropy, Maturity, And Maceral Microstructure In Organic-Rich Shales. In *2008 SEG Annual Meeting*. Society of Exploration Geophysicists.

Vernik, L., & Nur, A. 1992. Ultrasonic velocity and anisotropy of hydrocarbon source rocks. *Geophysics*, 52, 727-735.

Vernik, L., & Liu, X. (1997). Velocity anisotropy in shales: A petrophysical study. *Geophysics*, *62*(2), 521-532.

Vernik, L., & Milovac, J. (2011). Rock physics of organic shales. *The Leading Edge*, *30*(3), 318-323.

Vestrum, R. 1994. Group and phase velocity inversions for the general anisotropic stiffness tensor. M.Phil. thesis, The University of Calgary.

Weimer, Robert J. "Influence of Transcontinental arch on Cretaceous marine sedimentation: a preliminary report." (1978).

APPENDIX A

Table A1 D Chalk Velocity Measurements

		Chalk 0 degrees			Chalk 45 degrees			Chalk 90 degrees		
Pressure (psi)	Density (g/cc)	VP (m/s)	VS1 (m/s)	VS2 (m/s)	VP (m/s)	VS1 (m/s)	VS2 (m/s)	VP (m/s)	VS1 (m/s)	VS2 (m/s)
600	2.68	3883.97	2352.87	2389.11	3827.75	2326.93	2280.40	3820.86	2342.87	2296.20
1000	2.68	3899.31	2345.83	2392.97	3833.25	2332.36	2285.71	3820.86	2335.83	2303.00
1500	2.68	3905.74	2352.87	2396.84	3842.46	2337.81	2291.06	3823.25	2342.87	2303.85
2000	2.68	3883.97	2355.52	2398.79	3859.14	2341.24	2294.41	3835.27	2345.52	2309.83
2500	2.68	3901.88	2357.29	2399.27	3877.85	2342.61	2295.75	3844.94	2347.29	2313.27
3000	2.68	3901.88	2360.83	2403.65	3885.38	2348.11	2301.14	3852.23	2350.83	2319.30
3500	2.68	3913.47	2363.50	2404.14	3892.94	2350.18	2303.17	3859.54	2353.50	2322.76
4000	2.68	3925.14	2366.17	2404.63	3900.54	2357.80	2310.64	3861.98	2356.17	2324.50
4500	2.68	3930.35	2366.17	2405.11	3915.81	2365.46	2318.15	3866.88	2356.17	2326.23
5000	2.68	3922.54	2367.95	2405.60	3929.27	2371.07	2323.65	3874.25	2357.95	2327.97
5500	2.68	3935.57	2367.06	2406.58	3942.83	2371.78	2324.34	3876.71	2357.06	2330.59
6000	2.68	3940.80	2364.39	2410.50	3968.25	2374.59	2327.10	3881.64	2354.39	2336.71
6500	2.68	3944.74	2366.17	2411.48	3998.00	2380.24	2332.64	3886.59	2356.17	2340.23

Table A2 D Marl Velocity Measurements

		Marl 0 degrees			Marl 45 degrees			Marl 90 degrees		
Pressure (psi)	Density (g/cc)	VP (m/s)	VS1 (m/s)	VS2 (m/s)	VP (m/s)	VS1 (m/s)	VS2 (m/s)	VP (m/s)	VS1 (m/s)	VS2 (m/s)
600	2.68	3887.56	2139.57	2060.88	4649.64	2347.42	2341.14	4639.46	2481.32	2285.24
1000	2.68	3894.55	2140.97	2056.31	4649.64	2349.78	2340.35	4642.06	2484.29	2288.39
1500	2.68	3901.56	2141.68	2056.96	4652.69	2347.42	2338.79	4652.47	2484.29	2291.55
2000	2.68	3913.31	2147.34	2058.92	4664.91	2351.36	2341.92	4662.92	2483.54	2294.72
2500	2.68	3925.12	2154.46	2060.88	4674.13	2352.94	2342.70	4665.54	2491.00	2297.90
3000	2.68	3941.78	2154.46	2060.88	4667.98	2353.73	2345.06	4678.69	2489.50	2301.08
3500	2.68	3953.77	2136.75	2062.18	4692.66	2354.52	2348.99	4681.33	2488.01	2304.28
4000	2.68	3970.68	2157.32	2064.15	4689.56	2356.90	2350.57	4689.27	2490.25	2307.48
4500	2.68	3987.73	2164.50	2063.49	4677.21	2351.36	2348.99	4697.23	2495.49	2310.69
5000	2.68	3985.29	2168.11	2067.43	4695.77	2360.88	2349.78	4699.89	2500.75	2313.91
5500	2.68	3997.54	2163.06	2071.38	4711.35	2361.67	2348.99	4715.91	2504.53	2317.14
6000	2.68	4004.93	2165.22	2071.38	4720.74	2358.49	2349.78	4729.34	2512.11	2320.38
6500	2.68	4027.26	2168.11	2076.35	4722.31	2358.49	2356.11	4737.44	2515.91	2323.63

Table A3 D Chalk and Marl Microstrain Measurements

	Chalk_vert	Chalk_45	chalk_90	Marl 0	Marl 45	Marl 90
Pressure (psi)	microstrain	microstrain	microstrain	microstrain	microstrain	microstrain
8	0.000329218	0.000329218	0.000322056	0.000533	0.000402128	0.000467836
13	0.000515873	0.000511811	0.000496503	0.000813	0.000661907	0.000751445
22	0.000808824	0.000836502	0.00079925	0.001294	0.001105851	0.001235955
28	0.001068702	0.001045556	0.001017227	0.0016	0.001410448	0.001505376
35	0.001296296	0.001322252	0.001256214	0.001913	0.001751854	0.001851852
39	0.001449814	0.001433824	0.001393067	0.002074	0.001939737	0.00203125
42	0.001544118	0.001532847	0.001493065	0.002222	0.00204878	0.002148338
-8	6.91358E-05	6.91358E-05	7.08524E-05	5.33E-05	6.03191E-05	5.1462E-05
-13	0.000113492	0.000112598	0.000114196	9.26E-05	0.000101934	8.56647E-05
-22	0.000177941	0.000192395	0.000203809	0.000154	0.000173619	0.000154494
-28	0.000245802	0.000240478	0.000264479	0.000192	0.000225672	0.000195699
-35	0.000311111	0.00031734	0.000325359	0.000241	0.000289056	0.000257407
-39	0.000362454	0.000358456	0.000359411	0.00029	0.000329755	0.000314844
-42	0.00039375	0.000375547	0.000382225	0.000329	0.000348293	0.000335141

APPENDIX B

Workflow for developing anisotropic static stress profile

In a vertical wellbore with flat bedding planes C_{33}, C_{44}, and C_{66} can be determined using a log suite containing density, P-wave, dipole S-wave, and Stoneley wave data. The following steps can be performed to determine the minimum horizontal stress under static anisotropic assumptions.

Step 1. Perform laboratory dynamic and static testing on cores bedding-normal, 45 degrees to bedding, and bedding-parallel to obtain the stiffnesses required to describe a VTI medium.

Step 2. Use the dynamic measurements to find the Thomsen parameters ε, γ, and δ. Perform regression analysis to find the relationship between ε and γ and ε and δ. This allows estimation of C_{11} and C_{13}.

Step 3. Use the laboratory dynamic and static measurements to find the Young's modulus and Poisson's ratio for both measurement cases. This enables determination of the static case for the stress coupling coefficient, K_o.

Step 4. To apply the laboratory relationships to the well log, first find γ by using the Stoneley wave to find C_{66}. The Stoneley wave is related to the V_{SH}-wave with the following equation from Bratton (2014):

$$\left(\sqrt{\frac{\rho_{mud}}{\rho_b}}\Delta t_{shear}\right)^2 + \Delta t_{mud}^2 = \Delta t_{Stoneley}^2$$

Step 5: Use the laboratory relationships between the Thomsen parameters to estimate ε and δ, C_{11} and C_{13}.

Step 6: With all the stiffnesses required to describe a VTI medium, find the vertical and horizontal Young's modulus and Poisson ratio. Use the correction factors obtained from the laboratory static measurements to convert these elastic parameters to the static case. Find the stress coupling coefficient, K_o.

Step 7: Use the anisotropic static stress coupling coefficient to estimate minimum horizontal stress.